



Methods to Improve the Maintenance
of the Earth Catalog of Satellites
During Severe Solar Storms

By

Paul Gerard Wilkin

B.S. May 1988, Clarkson University
B.S. May 1986, St. John Fisher College

A Thesis submitted to

The Faculty of

The School of Engineering and Applied Science
of the George Washington University in partial satisfaction
of the requirements for the degree of Master of Science

September 1997

Thesis directed by

Robert H. Tolson
Professor of Engineering and Applied Science

This research was conducted at NASA Langley Research Center.

Abstract

The primary objective of this thesis is to investigate methods to improve the ability to maintain the inventory of orbital elements of Earth satellites during periods of extreme atmospheric disturbance brought on by severe solar activity. Existing tracking techniques do not account for such atmospheric dynamics. This can result in tracking errors of several seconds in predicted crossing time during periods of high geomagnetic activity for certain satellites. The reduction of these tracking errors is the principal goal of this thesis. Two techniques are examined for this purpose. In the first approach, density predicted from various atmospheric models is fit to the orbital decay rate for a number of satellites using a least-squares method. An orbital decay model is then developed that potentially could be used to reduce tracking errors by accounting for atmospheric changes. The second approach utilizes a Kalman filter to estimate the orbital decay rate of a satellite after every observation. The new information is then used to predict the next observation.

Results from the first approach demonstrated the feasibility of building an orbital decay model based on predicted atmospheric density, which then could potentially be used to reduce tracking errors. Correlation of atmospheric density to orbital decay was as high as 0.88. However, it is clear that contemporary atmospheric models need further improvement in modeling density perturbations brought on by solar activity in the polar region. The second approach of Kalman filtering satellite orbital decay resulted in a dramatic reduction in tracking errors for certain satellites during severe solar storms. For example, in the limited cases studied, the reduction in tracking errors ranged from 79 to 25 percent.

Acknowledgements

The author would like to express his gratitude towards Dr. Robert Tolson and Gerry Keating for their support and patience throughout the development of this thesis, to Dr. Paul Schumacher and Steve Knowles for their assistance in understanding radar fence operations, to Julian Vahlberg for his help with Kalman filtering, to Robert Grandle for recovery of fence data from 9-track tape, to Mike Hickey for aid in understanding the MET model, and lastly, to Jim Bass and Doug Reynolds for supplying the J77 model.

Table of Contents

Abstract	ii
Acknowledgements	ii
Table of Contents	iv
Nomenclature	vi
List of Abbreviations	ix
List of Figures	x
List of Tables	xii
1. Introduction	1
2. Theoretical Background	5
Measurement of Drag on Satellite Orbits	5
Discrete Kalman Filter	8
3. Atmospheric Models	13
Input Requirements	13
Model Descriptions	18
4. Data Description	22
Radar Fence	23
Observations	25
Orbital Decay Parameter (ODP)	25
5. Empirical Fit of Atmospheric Models to ODP	27
Satellite Selection Criteria	28
Sources of Density Variation	31
Correlation of Models to ODP	36

Ballistic Coefficient Estimation.....	62
6. One-State Kalman Filtering Approach.....	66
State Model	67
State Noise Model	67
Measurement Noise Model.....	70
Process Flow.....	71
Objects Selected.....	74
Satellite Residual Errors Prior to Filtering	74
Filtering Results	78
7. Conclusions and Recommendations.....	83
Atmospheric Modeling.....	83
Kalman Filtering.....	84
Future Work	86
Appendix A: Atmospheric Modeling	88
Appendix B: Model of Orbital Motion.....	92
Brouwer/Lyddane Model	92
Propagation Algorithm.....	98
Fence-Crossing Time Prediction.....	101
References	106

Nomenclature

A	Reference area of a satellite, [m ²]
a	Semi-major axis, [km]
C_D	Coefficient of drag
$C_{n,m}$	Geopotential coefficients
e	Eccentricity
e_k	Estimation error [revs/day ²]
$E[]$	Expectation operator
g	Acceleration due to gravity, [m/s ²]
H	Density scale height, [km]
H_k	Measurement matrix, [days ³ /rev]
I	Identity matrix
i	Inclination, [degrees]
J_n	Geopotential zonal terms
K_k	Kalman gain at time t_k , [revs/day ³]
k	Average time between element sets [days]
ℓ	Mean anomaly, [degrees]
ℓ_0	Mean anomaly at epoch, [degrees]
M_0	Molecular weight boundary condition, [g/mole]
\bar{M}	Mean molecular weight, [g/mole]
M_i	Molecular weight of i th species, [g/mole]
m	Mass, [g]

m	Mean, mean motion [revs/day]
n	Mean motion, [revs/day]
n_0	Mean motion at epoch, [revs/day]
\dot{n}	Time rate of change in mean motion, [revs/day ²]
n_i	Number density of i th species, [particles/m ³]
P	Pressure, [N/m ²]
P_n^m	Associated Legendre polynomials
P_k	Error covariance at time t_k , [revs/day ²] ²
Q_k	State covariance matrix at time t_k , [revs/day ²] ²
r	Position vector magnitude, [km]
R_k	Measurement noise covariance matrix at time t_k , [day ²]
R	Universal gas constant, [J mol ⁻¹ K ⁻¹]
R_\oplus	Equatorial radius of the Earth, [km]
$S_{n,m}$	Geopotential coefficients
T	Temperature, [°K]
T_0	Temperature boundary condition, [°K]
t	Time, [seconds]
U	Gravitational potential, [km ² /s ²]
v_k	White measurement noise with covariance R_k , [day]
w_k	White measurement noise with covariance Q_k , [revs/day ²]
x_k	State vector at time t_k , [revs/day ²]
\hat{x}_k	Estimate of state vector at time t_k , [revs/day ²]

\mathbf{x}_k^T	Transpose of state vector at time t_k
Z	ae/H
z	Geodetic altitude, [km]
\mathbf{z}_k	Measurement at time t_k , [day]

Greek

α_i	Thermal diffusion coefficient of i th species
α	Constant used in adaptive state noise
β	Geodetic latitude, [degrees]
β	Ballistic coefficient [g/cm^2]
γ	Constant used in non-adaptive state noise
$\delta_{k,j}$	Kronecker delta function
λ	Longitude, [degrees]
μ	Gravitational constant [km^3/s^2]
Ω	Right ascension of node [degrees]
ω	Argument of perigee [degrees]
ρ	Atmospheric density, [g/cm^3]
ρ_p	Atmospheric density at perigee, [g/cm^3]
ρ_0	Atmospheric density boundary condition, [g/cm^3]
$\Phi_{k,k+1}$	State transition matrix from t_k to t_{k+1}

Superscripts

$\dot{}$ (dot)	Derivative with respect to time
---------------------------	---------------------------------

List of Abbreviations

CW	Continuous Wave
DC	Differential Correction
EUV	Extreme Ultraviolet
J71	Jacchia 1971 Atmospheric Model
J77	Jacchia 1977 Atmospheric Model
LEO	Low Earth Orbit
LS	Least Square
LST	Local Solar Time
MET	Marshall Engineering Thermosphere Model
MSIS	Mass Spectrometer and Incoherent Scatter Model
NOAA	National Oceanic and Atmospheric Administration
NSC	Naval Space Command
OD	Orbit Determination
ODP	Orbital Decay Parameter $\begin{pmatrix} \dot{n} \\ n \end{pmatrix}$
PPT2	Orbit Propagation Software
RCS	Radar Cross-Section
RMS	Root-Mean-Square
SAV	Semi-Annual Variation
SLV	Seasonal-Latitudinal Variation
STM	State Transition Matrix
UCT	Uncorrelated Target

List of Figures

Figure 1: Geocentric and geodetic latitude.....	16
Figure 2: NSC radar fence receiver locations.....	23
Figure 3: ODP of Cosmos 1220 during 1989.....	30
Figure 4: Daily solar flux and geomagnetic activity during the year 1989.....	32
Figure 5: MET density, ODP of Cosmos 1220, A_p , and $F_{10.7}$	33
Figure 6: LST and latitude of perigee for Cosmos 1220.....	34
Figure 7: Perigee altitude and density scale height for Cosmos 1220.....	35
Figure 8: LS fit of MET density to the ODP of Cosmos 1220.....	37
Figure 9: MET density fit showing a phase lag with ODP of Cosmos 1220.....	38
Figure 10: Correlation of MET to Cosmos 1220 using phase shifts of 0 and 1 <i>k</i> -day.....	40
Figure 11: Correlation of MET to Cosmos 1220 using phase shifts of 2 <i>k</i> and 3 <i>k</i> -days.....	41
Figure 12: MET correlation vs. density lag.....	42
Figure 13: Correlation of MSIS to Cosmos 1220 using phase shifts of 0 and 1 <i>k</i> -day.....	44
Figure 14: Correlation of MSIS to Cosmos 1220 using phase shifts of 2 <i>k</i> and 3 <i>k</i> -days.....	45
Figure 15: Correlation of J71 to Cosmos 1220 using phase shifts of 0 and 1 <i>k</i> -day.....	46
Figure 16: Correlation of J71 to Cosmos 1220 using phase shifts of 2 <i>k</i> and 3 <i>k</i> -days.....	47
Figure 17: Correlation of J77 to Cosmos 1220 using phase shifts of 0 and 1 <i>k</i> -day.....	48
Figure 18: Correlation of J77 to Cosmos 1220 using phase shifts of 2 <i>k</i> and 3 <i>k</i> -days.....	49
Figure 19: Correlation of MET to Explorer 8 using phase shifts of 3 <i>k</i> -days.....	55
Figure 20: Correlation of MET to Explorer 8 using phase shifts of 8 <i>k</i> -days.....	56
Figure 21: Effect of lag on Explorer 8 correlation.....	57
Figure 22: Correlation of J71 to Atlas F using phase shifts of 3 <i>k</i> -days.....	58

Figure 23: Ballistic coefficient plot.....	63
Figure 24: Kalman filter process flow diagram.....	72
Figure 25: Residual crossing errors and ODP for Cosmos 1601 without filtering.	75
Figure 26: Residual crossing errors and ODP for Cosmos 1776 without filtering.	76
Figure 27: Residual crossing errors and ODP for Meteor 1 without filtering.	77
Figure 28: Effect of a one-state Kalman filter on Cosmos 1601 fence-crossing errors.	79
Figure 29: Fence-crossing geometry.....	102
Figure 30: Satellite crossing radar fence-plane.....	103

List of Tables

Table 1: Required atmospheric model inputs	14
Table 2: Satellite characteristics	53
Table 3: Model correlation coefficients.....	54
Table 4: Change in correlation after fitting $\rho H^{\frac{1}{2}}$ to ODP.....	61
Table 5: Characteristics for additional satellites	74
Table 6: Filter results for an adaptive state noise.....	80
Table 7: Filter results for a non-adaptive state noise.	81

1. Introduction

The tracking of artificial earth satellites began with the launch of Sputnik in 1957. During the Cold War it was imperative to distinguish existing satellite orbits from new launches to determine whether or not those new satellites posed a threat. Today, the environment is considerably different but the need still exists to be able to identify satellites. In addition, the U.S. has treaty agreements to predict satellite re-entry and notify the appropriate country where landfall is expected to occur.¹ Currently there are over 8,000 satellites in orbit, which is considerably more than even a few years ago. Consequently, congestion and collision avoidance are growing concerns and hence one of the continuing needs for space surveillance. An inventory of orbital information on every satellite is continuously maintained and hereinafter referred to as the Earth satellite catalog.

Satellite tracking is achieved through the use of various radar installations such as the fence that is operated by the Naval Space Command (NSC) from Dahlgren, VA.² As a satellite passes through the fence, receivers detect a reflected signal and a crossing time is associated with the peak amplitude of the reflected signal. A predicted crossing time for the satellite being tracked is calculated using orbital theory. This predicted time is compared to the actual crossing time and if the difference is within a specified tolerance the satellite is considered identified. Otherwise, the satellite becomes an uncorrelated target (UCT). UCT's can occur for a number of reasons including the launching of new objects, collisions between existing ones, explosions, propulsive maneuvers, approximations made in the geopotential of the Earth, or from disturbances in the

atmosphere resulting in a change in density and therefore a change in atmospheric drag. Increased drag decreases the orbital energy of a satellite and consequently the semi-major axis of the orbit. Since the square of the period of a satellite is proportional to the cube of the semi-major axis, a decrease in the semi-major axis will result in a decrease in the period of a satellite. Therefore, an increase in drag will cause a satellite to arrive earlier at the fence than predicted.

Drag effects are incorporated in the orbit model by carrying, in addition to the six orbital elements, a seventh term, the rate of change in mean motion, or \dot{n} . This term, also known as the orbital decay parameter (ODP), is used to absorb non-central forces such as drag, solar radiation pressure, forces due to higher order harmonics, thrusting, etc., that are not incorporated into the orbital model.

A catalog entry for a new satellite is created shortly after launch when elements are initially calculated using orbit determination (OD) methods. Periodic updates to the orbital elements are required to maintain the catalog. This is accomplished by using a differential correction (DC) process of the orbital elements. This process requires many observations, spanning days, whereby residuals are created by differencing the actual observation from those predicted by the orbit model. In addition, DC of elements requires the solution of a set of j simultaneous linear equations in seven unknowns, where j is the number of observations. Since the number of observations is typically larger than the number of unknowns, there are more equations than unknowns and therefore no unique solution. To find the best solution, a batch least-squares (LS) process is employed,

providing the corrections to the elements that minimizes the square root of the arithmetic mean of the squared residuals, or root mean square (RMS).³

For low Earth orbiting (LEO) satellites, ODP is primarily an indication of atmospheric drag a satellite experiences. Because ODP is part of the LS solution to the DC process that can involve several days worth of observations, ODP will be an average indication of the drag acting on a satellite during the period of observation. Because atmospheric disturbances can have time spans on the order of hours, using the smoothed ODP to make fence crossing predictions has led to fence crossing errors greater than 10 seconds. Such a large error is well outside the crossing tolerance of 2 seconds and therefore not conducive to maintaining the satellite catalog.

The present research centers around reducing UCT's that are caused by the atmospheric perturbations mentioned above. This is accomplished by studying several atmospheric models and, in the first approach, developing a simple drag or ODP model that could be applied to the current orbital equations and potentially reduce the number of UCT's occurring. As a second approach, a Kalman filter is used to continuously update ODP after each observation. This updated ODP is then used in place of the batch ODP to reduce UCT's.

This thesis begins with a review of the governing equations, followed by descriptions of the atmospheric models studied. Next, a description of the radar fence and the data it generates is given. Thereafter the ODP model is presented, followed by the Kalman filter approach and concluding remarks.

Additional background information is provided in the appendices, including the model of orbital motion as well as an introduction to the fundamental theory of atmospheric modeling.

2. Theoretical Background

This chapter presents the basic equations relating the orbital decay rate of satellites to atmospheric density followed by an introduction to the Kalman filter equations.

Measurement of Drag on Satellite Orbits

The development of atmospheric models has relied historically on the measurement of drag as indicated by the change in period, or the orbital decay parameter (ODP) of satellites, and more recently on space-borne instruments such as mass spectrometers and gas analyzers.⁴ To develop such models though, analytical relationships were required that related the orbital decay of a satellite to drag and density. These expressions form the basis for the first research approach of this thesis in developing a method to estimate \dot{n} or ODP of LEO satellites by comparing ODP to density predicted by atmospheric models.

The equations that estimate \dot{n} are broken down into various categories based on satellite orbit type. For simplicity, the atmosphere has been assumed to be spherical and exponential, with constant density scale height H , and rotating at the angular rate of the Earth.⁵

For satellites with $e < 0.2$ and $ae/H > 3$, \dot{n} is estimated by⁶

$$\dot{n} = 3\pi\delta a n^2 \rho_p \exp\left(-\frac{ae}{H}\right) \left[I_0 + 2eI_1 + \frac{3}{4}e^2(I_0 + I_2) + O(e^3) \right] \quad (1)$$

where ρ_p is the density at perigee, I_0 , I_1 , and I_2 are Bessel functions of the first kind of order n and argument Z , written $I_n(Z)$, where $Z = ae/H$. Further, δ is given by

$$\delta = \frac{FAC_d}{m} \quad (2)$$

where C_D is the coefficient of drag, A is the reference area of the satellite, m is the mass of the satellite, and F is the atmospheric rotation factor represented by

$$F = \left(1 - \frac{r_p w}{v_p} \cos i\right)^2 \quad \text{for } i \leq \frac{\pi}{2}$$

$$F = \{2 - F(\pi - i)\} \quad \text{for } i > \frac{\pi}{2} \quad (3)$$

where r_p and v_p are the position and velocity of the satellite at perigee relative to the center of the Earth, and w is the angular rate of rotation of the atmosphere. For satellites with $e < 0.2$ and $Z < 3$, \dot{n} is approximated by

$$\dot{n} = 3\pi\delta a n^2 \rho_p \exp(-Z) [I_0 + 2eI_1 + O(e^2)] \quad (4)$$

However, for satellites in orbits with eccentricities larger than 0.2, \dot{n} is given by⁷

$$\dot{n} = 3\delta\rho_p n^2 \left(\frac{\pi Ha}{2e}\right)^{\frac{1}{2}} \frac{(1+e)^{\frac{3}{2}}}{(1-e)^{\frac{1}{2}}} \left\{1 - \frac{8e-3e^2-1}{8Z(1-e^2)} + O(5 \times 10^{-5})\right\} \quad (5)$$

These analytical approximations to satellite \dot{n} can be used to improve atmospheric models if the ballistic coefficient of the satellite is well known, where the ballistic coefficient, β , is defined to be $\frac{m}{C_d A}$.⁸ Calculating the ballistic coefficient requires knowing how a satellite is oriented throughout its orbit, which enables the cross-sectional area perpendicular to the direction of motion to be calculated. For this reason, spherical satellites are often used when atmospheric models are being developed.⁹

When estimating ODP values given an atmospheric model, calculating the ballistic coefficient for satellites in the satellite catalog would be a difficult task, due to the many complex satellite geometries existing, and the fact that the orientation of the majority of satellites is unknown, and perhaps changing. However, given actual ODP values from observations and predicted density and perigee, the mean ballistic coefficient of a satellite could be estimated by using the appropriate ODP equations.

Despite the obstacles in evaluating ODP, the feasibility of estimating satellite ODP by fitting predicted model densities to actual ODP in a least squares (LS) sense will be evaluated in Chapter 5. The degree to which the estimated ODP values agree with actual data will depend on the accuracy of the atmospheric model, assuming the particular satellite in question is not thrusting or subject to other perturbations other than drag and the geopotential. There are several factors that greatly affect density and it is the modeling of these factors that will determine how well an atmospheric model will fit the ODP of a given satellite. The handling of these factors varies from model to model and for this reason, a number of atmospheric models will be applied towards the estimation of ODP. But prior to beginning this, a brief discussion of the major factors that affect density is introduced in Chapter 3, followed by short descriptions of four atmospheric models.

Discrete Kalman Filter

The second research approach, a single state Kalman filter¹⁰, will be applied to update the state or ODP after each fence observation. Kalman filtering is a linear, LS process that uses state-space methods and recursive algorithms to estimate a state variable, or signal, from measurement data containing an element of random noise. One of the main features of Kalman filtering is using the results from the previous step to estimate the current state, as opposed to a batch process that generally uses all the data to estimate the state. In addition, a batch process can not readily handle state noise, particularly if it is time dependent. In the case of estimating ODP of a LEO satellite, it will be shown that ODP is highly dependent on the time varying interaction of solar energy with the upper atmosphere as indicated by the geomagnetic index, A_p , and solar radio flux, $F_{10.7}$, which will be introduced in Chapter 3. It is the time varying state noise-level of ODP that suggests Kalman filtering will produce a better state estimate during periods when the state noise-level of ODP is rapidly changing, as is the case during the waxing and waning of solar and geomagnetic storms.

To take advantage of the Kalman filter recursive solution, a few assumptions must be made. First, the process to be estimated can be modeled in the following form:

$$\mathbf{x}_{k+1} = \Phi_{k,k+1} \mathbf{x}_k + \mathbf{w}_k \quad (6)$$

where the state vector at time t_k , denoted by \mathbf{x}_k , $\Phi_{k,k+1}$, represents the state transition matrix (STM), and \mathbf{w}_k , a white noise sequence with covariance \mathbf{Q}_k . The STM describes how the state evolves from one time to another. White noise is defined as a sequence of

random variables uncorrelated in time with a mean of zero. Therefore the covariance matrix can be expressed as:

$$E[\mathbf{w}_k \mathbf{w}_j^T] = \mathbf{Q}_k \delta_{k,j} \quad (7)$$

where $\delta_{k,j}$ is the Kronecker delta function. This means that there is no statistical relationship between the value of \mathbf{w}_k and \mathbf{w}_{k+1} , *i.e.*, for any time other than when t_k equals t_j . However, this does not mean that the individual elements of \mathbf{w}_k are uncorrelated. There could be a significant correlation at any time as described by the off-diagonal terms in \mathbf{Q}_k . The second assumption necessary to utilize discrete Kalman filtering requires the observation or measurement of the process to occur at discrete points in time according to the linear relationship:

$$\mathbf{z}_k = \mathbf{H}_k \mathbf{x}_k + \mathbf{v}_k \quad (8)$$

Here, \mathbf{z}_k denotes the vector of measurements at time t_k , \mathbf{H}_k is a matrix defining the ideal (noiseless) mapping from state space into measurement space at time t_k , and lastly \mathbf{v}_k symbolizes the associated measurement error and similarly to \mathbf{w}_k , assumed to be a white sequence with known covariance structure

$$E[\mathbf{v}_k \mathbf{v}_j^T] = \mathbf{R}_k \delta_{k,j} \quad (9)$$

and having zero cross-correlation with \mathbf{w}_k that is

$$E[\mathbf{w}_k \mathbf{v}_j^T] = 0 \quad (10)$$

for all k and j . A third requirement is that there is information available regarding the initial estimate of the state at time t_k , and that this information is based on knowledge prior to t_k . This prior or *a priori* estimate is represented by $\hat{\mathbf{x}}_k^-$, where the symbol $\hat{}$ or “hat”

above the state vector denotes that this is an estimate, and the minus means that this is a best estimate prior to processing the information in measurement \mathbf{z}_k at time t_k . A further assumption is that the associated error covariance of $\hat{\mathbf{x}}_k^-$ is known. Estimation error is defined as the difference between the true and estimated state, i.e.,

$$\mathbf{e}_k^- = \mathbf{x}_k - \hat{\mathbf{x}}_k^- \quad (11)$$

The error covariance matrix is then:

$$\mathbf{P}_k^- = E[\mathbf{e}_k^- \mathbf{e}_k^{-T}] \quad (12)$$

where it has been assumed the estimation error has a mean of zero, i.e., the estimate is unbiased.

With the above assumptions, it is now possible to utilize the measurement \mathbf{z}_k to improve the prior estimate. This is accomplished by¹¹

$$\hat{\mathbf{x}}_k^+ = \hat{\mathbf{x}}_k^- + \mathbf{K}_k (\mathbf{z}_k - \mathbf{H}_k \hat{\mathbf{x}}_k^-) \quad (13)$$

where \mathbf{K}_k is a linear weighting factor applied to the difference between the measurement \mathbf{z}_k and the resultant linear mapping of the prior estimate $\hat{\mathbf{x}}_k^-$ from state space into measurement space. The gain \mathbf{K}_k is determined by picking an optimization criteria. The Kalman gain is determined by picking the gain that minimizes the terms along the diagonal in the error covariance matrix \mathbf{P}_k . This is chosen because the diagonal terms represent the estimation error variances for the state vector elements. The Kalman gain \mathbf{K}_k is then given by:

$$\mathbf{K}_k = \mathbf{P}_k^- \mathbf{H}_k^T (\mathbf{H}_k \mathbf{P}_k^- \mathbf{H}_k^T + \mathbf{R}_k)^{-1} \quad (14)$$

The covariance matrix associated with the optimal estimate shown in (13) is then given by

$$\mathbf{P}_k^+ = (\mathbf{I} - \mathbf{K}_k \mathbf{H}_k) \mathbf{P}_k^- \quad (15)$$

where \mathbf{I} is the identity matrix. All the elements are now present to update the estimate and the associated error covariance matrix, but to be able to continue the process in anticipation of the next observation at t_{k+1} , both $\hat{\mathbf{x}}_k^+$ and \mathbf{P}_k^+ need to be projected ahead in time to function as the next *a priori* associated with measurement \mathbf{z}_{k+1} . This is accomplished via the STM.

$$\hat{\mathbf{x}}_{k+1}^- = \Phi_{k,k+1} \hat{\mathbf{x}}_k^+ \quad (16)$$

$$\mathbf{P}_{k+1}^- = \Phi_{k,k+1} \mathbf{P}_k^+ \Phi_{k,k+1}^T + \mathbf{Q}_k \quad (17)$$

This process is then repeated as future measurements become available. Figure 2 illustrates the Kalman filter process.¹²

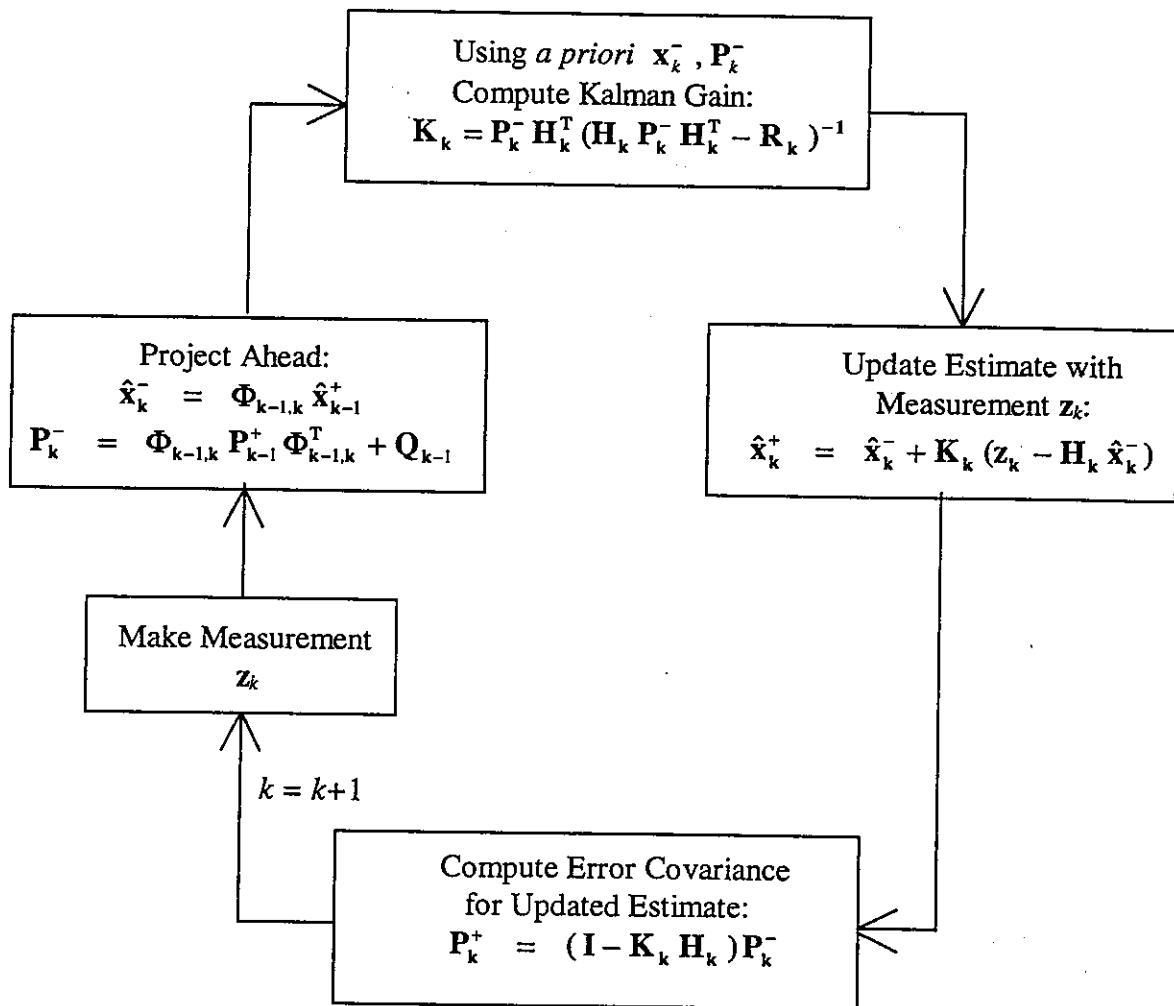


Figure 2: Kalman filter process

3. Atmospheric Models

Empirical atmospheric models have been developed for a number of reasons, some of which include improving orbit prediction capabilities, understanding atmospheric processes and, more recently, aerobraking maneuvers.¹³ There are three basic types of empirical atmospheric models that have been developed: those developed from studying the rate of change in the period of satellites due to drag, those formulated from space-borne instruments such as mass spectrometers, and those models which are hybrids or comprised of both drag-derived and instrument based measurements.

To provide background prior to the development of a density based ODP model, the input requirements of atmospheric models will be discussed, followed by descriptions of the four models of the upper atmosphere that were chosen for this study. An introduction to atmospheric modeling can be found in Appendix A.

Input Requirements

Table 1 shows the inputs required by the atmospheric models before density can be estimated.

Table 1: Required atmospheric model inputs

Argument	Units/Form
Geodetic Altitude	km
Geodetic Latitude	Degrees
Longitude	Degrees
Day of Month	DD
Month	MM
Year	YY
Hour of LST	HH
Minute of LST	mm
Previous Day Solar Radio Flux, $F_{10.7}$	$\times 10^{-22}$ Watts/m ² /Hz
81-Day Smoothed Solar Flux, $\bar{F}_{10.7}$	$\times 10^{-22}$ Watts/m ² /Hz
Current Day Geomagnetic Index, A_p	0 – 400

Geodetic Altitude

The density of the atmosphere is primarily a function of the altitude above the surface of the Earth, which is oblate. As a result, the atmosphere is also oblate, meaning the atmosphere has an equatorial bulge as well.¹⁴ Therefore, to model the atmosphere correctly, a reference must be chosen to represent the surface of the Earth from which altitude will be measured. Various models of the surface of the Earth exist, but the most

common in use is a reference spheroid, which is an ellipse rotated about the minor axis to represent the oblateness of the Earth. Specifically, the ellipse is defined by the equatorial radius, $R_{\oplus} \approx 6378.140$ km, and the ellipticity or flattening,

$$f \equiv \frac{R_{\oplus} - R_p}{R_{\oplus}} \approx \frac{1}{298.257} \quad (18)$$

where R_p is the polar radius. A much more complex model is the equipotential surface of the gravitational field, which is known as the geoid or mean sea level, and contains many local irregularities due to the non-uniform mass distribution of the Earth.¹⁵ True geodetic altitude is the altitude measured from the geoid upward, but the basic reference spheroid model is used to approximate geodetic altitude and is adequate for use in most atmospheric models.

Geopotential Altitude

Gravitational potential is defined as

$$\Phi = \int_0^z g dZ \quad (19)$$

where Φ is the gravitational potential, g the acceleration due to gravity, and z the geometric height above a reference spheroid. Geopotential height or altitude is expressed as

$$h = \frac{\Phi}{g_0} = \frac{1}{g_0} \int_0^z g dZ \quad (20)$$

where h is the geopotential altitude and g_0 is the fixed reference value of gravity, equal to 9.80665 m/s^2 .¹⁶

Geodetic Latitude

Although the oblateness of the Earth does not affect the definition of longitude, it does complicate the definition of latitude. Figure 1 illustrates two common definitions of latitude.

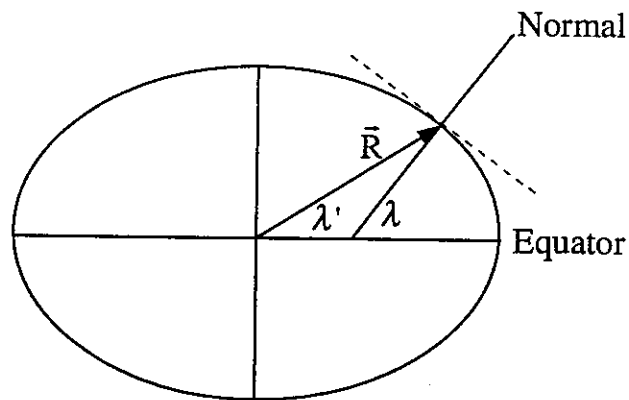


Figure 1: Geocentric and geodetic latitude

The angle labeled λ' is called geocentric latitude and is defined as the angle between the equatorial plane and the position vector \vec{R} from the geocenter. Geodetic latitude is represented by the angle λ and is defined as the angle between the equatorial plane and the normal to the surface of the reference spheroid. Geodetic latitude is the foundation for most maps and, in this case, geodetic latitude would be synonymous with geographic latitude.¹⁷

Solar Radio Flux

Ultraviolet (UV) solar radiation heats the upper atmosphere through adsorption and consists of two components, one associated with the 27-day solar rotation and sunspots, and the other related to the 11-year solar cycle. Due to energy adsorption, UV solar radiation is difficult to measure directly at the surface. However, the extreme ultraviolet (EUV) radiation received from the sun has been highly correlated to the surrogate index, $F_{10.7}$, which is a ground-based measurement representing the solar radio flux at a wavelength of 10.7 centimeters.¹⁸ The solar radio flux also consists of the short-term solar rotation component and the long-term 11-year solar cycle. Both of these components affect the upper atmosphere differently and must be treated separately. Although separate values of these two components of the solar radio flux are not easily available, a relationship is used relating the 11-year solar cycle to the flux averaged or smoothed solar radio flux, $\bar{F}_{10.7}$.¹⁹ This allows the smoothed solar radio flux to be used to represent long-term solar cycle effects on the atmosphere.

Geomagnetic Index

Geomagnetic activity is the result of the interaction of the solar wind with the Earth's magnetic field. Solar wind kinetic energy is partially adsorbed by the magnetosphere, transformed, and eventually dissipated in the magnetic polar regions of the atmosphere in the form of heat and ionization. Geomagnetic activity is monitored by means of planetary indices such as A_p , which like the solar radio flux $F_{10.7}$, is an indirect measure of source strength that has a reasonable correlation to observed energy dissipation effects. Specifically, A_p is a ground-based measurement taken using magnetometers placed at various stations.²⁰

Model Descriptions

Four models were studied and their ability to correlate with satellite drag was compared. The models examined were the Marshall Engineering Thermosphere (MET)²¹, the L.G. Jacchia 1971 (J71)²² model, the J77²³ model, and lastly, the Mass Spectrometer Incoherent Scatter (MSIS)²⁴ 1986 model. A description of each of these models follows.

Jacchia 71 Model

The J71 model is a revised version of the drag-derived J70 model.²⁵ Minor modifications have been made to numerical coefficients, as well as to the height of the homopause. The homopause is the transition region where the model switches from hydrostatic equilibrium, governed by the barometric equation, to diffusive equilibrium as

represented in the diffusion equation. Changes were based on mass spectrometer and EUV absorption data at 150 km, suggesting that the concentrations of N_2 and O_2 needed to be decreased by 16 and 36 percent respectively, whereas atomic oxygen needed to be increased by 37 percent. In addition, the correction made in J70 to the exospheric temperature, T_{∞} , due to the semiannual variation (SAV) was replaced in J71 with a more sophisticated correction made directly to density. The J71 model dissociates SAV from temperature entirely, clearing up many puzzling results in the helium-hydrogen region and eliminating the need for adding *ad hoc* variations for these constituents.²²

Given the above required model inputs, the process of determining density begins by calculating T_{∞} . J71 accomplishes this by using empirical relations that correct for variations due to solar activity, diurnal or day/night effects, latitudinal/seasonal variations, and geomagnetic activity. Once T_{∞} is calculated, the result is then applied to Jacchia's empirical temperature profiles, and, together with an expression for the atmospheric mean molecular weight, numerical integration is performed on the barometric equation starting with a boundary condition at 90 km and integrating up to an altitude of 100 km. Above this point, the diffusion equation is integrated separately for each atmospheric constituent and the partial densities are combined to provide the total density. Once the integration up to altitude Z has occurred, corrections are added to the total density for the seasonal latitudinal variation (SLV), SAV, and the winter helium "bulge".²⁶

Marshall Engineering Thermospheric Model

The Marshall engineering thermospheric (MET) model is a drag-derived model that is based on J70 but with the SLV and helium bulge corrections taken from the J71

model²¹. Other differences between MET and J71 include modifications made to coefficients in the temperature profile and the sixth order polynomial used to estimate mean molecular weight between 90 and 100 km. In addition, the height of the homopause in MET is set to 105 km, whereas in J71 it is lowered to 100 km.

MSIS-86 Model

The mass spectrometer incoherent scatter (MSIS) model was developed by A. E. Hedin using spacecraft borne mass spectrometers as well as ground-based incoherent scatter radar data. This model uses a Bates temperature profile²⁷ for the upper thermosphere and an inverse polynomial for the lower thermosphere, which are both functions of geopotential height rather than geodetic height. Substituting geopotential height for geodetic height allows exact integration of the barometric equation, assuming a constant mean molecular weight and using a boundary condition at 120 km. Exospheric temperature as well as other primary quantities are expressed as functions of geographic and solar/magnetic parameters using spherical harmonics in latitude and longitude where relevant.²⁴

Jacchia 77 Model

The Jacchia 77 model is a major revision of Jacchia's earlier models. Here he incorporates instrument based mass spectrometric and extreme ultraviolet (EUV) data in an effort to improve the representation of individual atmospheric constituents, while using satellite drag data to indicate total density. One of Jacchia's major changes in J77 is in his formulation of the effect of geomagnetic activity on temperature and density. In his prior

models, corrections were made only to T_{∞} prior to integration. However, J77 incorporates both an additive term to T_{∞} and a perturbation to the temperature profile, necessitating further integration. Other terms are added as well, including a term representing the effect of the magnetic disturbance on the height of the homopause and a term modeling an equatorial wave that convects from the geomagnetic pole regions towards the equator.²³

4. Data Description

The Catalog of Earth satellites is a database containing information on every known object greater than or equal to 4 inches in diameter that is currently in orbit.²⁸ Objects include active and inactive satellites, rocket bodies (RB's), and general space debris. Currently, the catalog contains over 8,000 satellites, with each catalog record containing: a satellite identification number, orbital elements, an epoch or time associated with the elements, and an orbital decay parameter (ODP).²⁹

One purpose of the catalog is to enable the detection of launches of new satellites, and to determine the country of origin, for security reasons. In addition, the US holds a treaty agreement with other nations, requiring the US to predict the time and location for reentry of space debris, and to notify the appropriate country where landfall is expected.³⁰ Further, with an increasing number of satellites and debris comes the increased need for collision avoidance. By tracking satellites and updating the catalog, the catalog may be used to accomplish all of these tasks. However, it is during periods of the extreme solar and geomagnetic storms mentioned previously in Chapter 3, that maintaining the satellite catalog becomes more difficult, and therefore the subject of this study.

In both the ODP predictor model and the Kalman filter approaches to improve the maintenance of the satellite catalog, the primary data source will be ODP values listed in the catalog for a dozen LEO satellites. But before attempting to implement these approaches, an understanding of the data and its source is required. To accomplish this, a

description of the radar fence and fence observations is provided, followed by a discussion on the calculation of ODP.

Radar Fence

The Naval Space Command (NSC) operates a radar fence across the southern United States for purposes of helping to maintain the catalog of Earth orbiting objects.³¹ The fence is comprised of 3 transmitters and 6 receiver stations located on an approximate great circle with an inclination of 33.6° relative to the equator. Figure 2 shows a map of the U.S. where the symbols indicate the location of the six receiver stations.

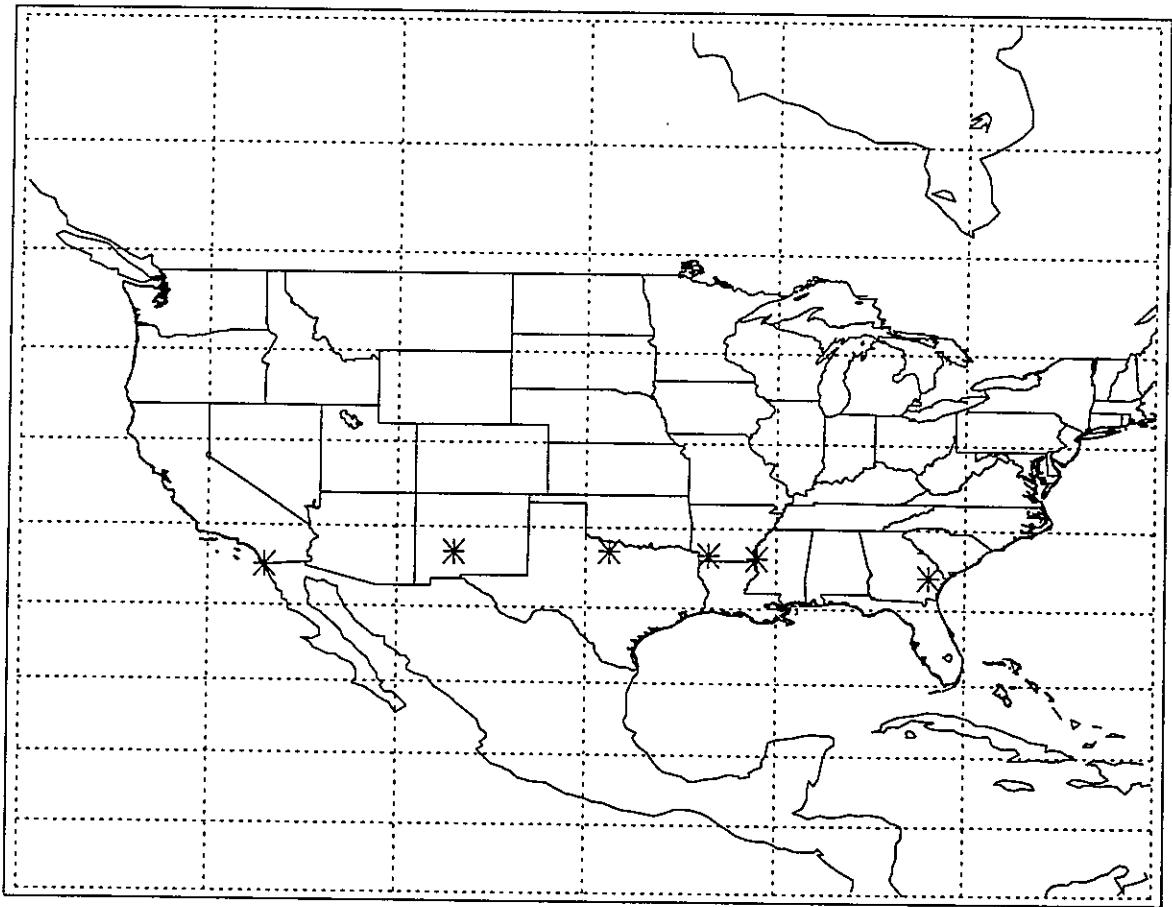


Figure 2: NSC radar fence receiver locations.

Transmitters

The three transmitters are located at Gila River, NM, Lake Kickapoo, TX, and Jordan Lake, AL. Continuous wave (CW) illumination is used to provide the maximum average power. Under high power conditions, radar coverage is a thin vertical fan of width 0.02° . The resolution of the fence is an important factor when considering the growing size of the satellite catalog. To distinguish the reflected signal of one satellite from another, there must be an adequate amount of time between signals. However given the above fence characteristics, the radar fence would be approximately 350 meters wide at an altitude of 1000 km, providing a temporal resolution of 50 ms.³² With a catalog of 8,000 satellites, the number of fence crossings is approximately 20,000 per day, or the equivalent of a fence-crossing every 4 seconds. Thus, resolving fence-crossing signals using a radar fence with a temporal resolution of 50 ms is quite feasible, assuming drag effects are insignificant. However, during periods of severe solar storms, changes in drag can alter the crossing time of a satellite by more than 10 seconds. It is during these perturbed periods that the resolution of fence-crossing signals and subsequent identification of satellites can become a problem, and hence the need and interest in finding methods to improve the maintenance of the satellite catalog.

Receivers

Up to six stations can receive the reflected signal from a satellite passing through the fence, when the elevation angle of the satellite is above the local horizon. Fundamental measurements are elevation angle or zenith angle, azimuth angle, and time of crossing. Radio interferometry is used to measure the angle an incoming signal has with

the local vertical and the "time of crossing" is determined by the peak strength of the reflected signal. Typical crossing time can be resolved with errors of no more than several milliseconds. Position can be determined using two receiver stations and triangulation, with an accuracy of 400 meters.³³

Observations

Station observations are recorded in two forms, depending on the source of the data. NSC records elevation and azimuth angles, whereas the US Space Command (USPACOM) records x, y, z position. Typical observations are recorded in the following format: satellite crossing time in the form of year, month, day, hour, minute, and second, the source of the data, i.e. NSC fence, or USPACOM, the receiver station number, the satellite 5-digit ID, and for NSC observations, elevation or zenith angle and azimuth angle. Elevation angle is the angle between the local horizontal and the satellite vector, whereas zenith angle is the complimentary angle. Azimuth is the angle formed in the horizontal plane between the local East vector and the horizontal component of the satellite vector. If the source of the observation is USPACOM, the aforementioned angles are replaced with x, y, and z position.³⁴

Orbital Decay Parameter (ODP)

The orbital decay parameter (ODP) is produced using several days of fence observations in a differential correction (DC) process that determines the updates to the seven-element model. Because the number of observations is typically greater than the number of elements, no unique solution exists. Therefore the best solution in a least-

squares (LS) sense is sought, or equivalently, a solution that causes the sum of the squares of the fence crossing residuals to be a minimum.³⁵ The orbit type of each satellite determines actual data spans. For example, a satellite that is experiencing rapid orbital decay will require a short fit span of about a day of observations, whereas for a satellite in a slowly decaying orbit, fit spans of 3-7 days or longer are used. After recording the required amount of data, the DC process yields mean elements with the epoch occurring on the last observation time.³⁶ This process has several consequences. First, the longer the fit span, the smoother the resulting ODP will be because this is an average solution that is the best fit over the entire span of data. Second, because the time-tag of the elements occurs at the time of the last observation, a phase lag will be introduced into the ODP of the satellite of about $\frac{1}{2}$ the fit-span. This means that variation in ODP resulting from changes in the atmospheric density will appear in element set data with lower resolution and occurring from 1.5 to 3.5 days after the actual atmospheric disturbance occurred.

5. Empirical Fit of Atmospheric Models to ODP

Ignoring new satellites, collisions between existing ones, and propulsive maneuvers, the major cause of uncorrelated targets (UCT's) is due to changes in the density of the atmosphere that are not accounted for in the seven element orbit propagation model used to maintain the satellite catalog as described in Appendix B. Variations in solar and geomagnetic activity are the primary sources for these disturbances in density. The resulting changes in drag can affect the along-track orbital position of a LEO satellite anywhere from several meters to hundreds of kilometers per day, depending on the mass-to-area ratio of the satellite and orbit.³⁷ Along-track deviations change the orbital period of a satellite and can be expressed as changes in mean motion or ODP. In addition, the ODP derived from DC of elements is a smoothed or averaged estimate of satellite drag which will not contain the resolution necessary to be an accurate indication of satellite drag during periods of severe atmospheric disturbance. Therefore, applying an averaged ODP that also contains a phase lag can lead to large fence crossing errors and UCT's during times of high solar and geomagnetic activity. However, including atmospheric modeling as part of the orbit propagation model by developing and applying a model of ODP, these atmospheric disturbances and corresponding perturbations in density and drag can be accounted for, and potentially lower the number of UCT's.

The evaluation of ODP is a complex problem, due to the many factors influencing the orbital decay of a LEO satellite. This is revealed in Chapter 2 by the orbital decay equations (1), (4), and (5), which relate the ODP of a satellite to density at perigee, the ballistic coefficient, density scale-height, eccentricity, mean motion, and semi-major axis.

The ballistic coefficient, β , represented by the quantity $\frac{m}{C_D A}$, is often unknown or varying for many satellites in the Earth catalog. For satellites other than spheres, the calculation of the cross-sectional area A may not be straightforward, as in the case of a tumbling satellite. In addition, the coefficient of drag is a function of satellite shape, altitude, surface characteristics, atmospheric composition, speed ratio of incoming particles, and solar activity.³⁸

Despite these complexities, an ODP model is developed to estimate ballistic coefficients and times of strong atmospheric perturbations, which potentially could be used to reduce UCT's. This will be accomplished by applying different atmospheric models to estimate density at perigee for a number of satellites over a period of time. The density values will then be correlated to satellite ODP and a least squares (LS) process will be used to develop a linear relation between density at perigee and ODP. This approach was chosen rather than including density as part of the orbit propagation algorithm because adding perturbations due to density and drag would require replacing the propagation process with an integration technique such as Cowell's method.³⁹

Prior to beginning the correlation of model densities to satellite ODP values, the criteria used in selecting satellites for this study is outlined, followed by a discussion on the sources of density variation.

Satellite Selection Criteria

To test the approach of correlating model densities to satellite ODP, satellites were selected that were in non-circular orbits, having a perigee altitude below 1000 km, and

daily updates to the element sets. Further, a time period of interest was selected that involved significant atmospheric disturbances as indicated by both the solar radio flux $F_{10.7}$ and the geomagnetic activity index A_p .

The period of interest that was chosen to examine the capability of the various atmospheric models was the year 1989. During this period, there were three severe geomagnetic storms, the first of which was the 3rd largest in the last sixty years.⁴⁰

Upon implementing the above selection criteria, Cosmos 1220 was chosen. Cosmos 1220 was launched by the USSR on November 4, 1980 and placed into an orbit with an eccentricity of 0.02, inclination of 65° , and perigee height of 575 km.

Cosmos 1220 is believed to be a cylinder of unknown size and originally capable of maneuvering.⁴¹ However, since the period of study of this investigation is over 8 years after launch, it is probable that Cosmos 1220 was no longer capable of thrusting. Figure 3 shows how ODP of Cosmos 1220 varied throughout 1989. The plot reveals many distinct spikes

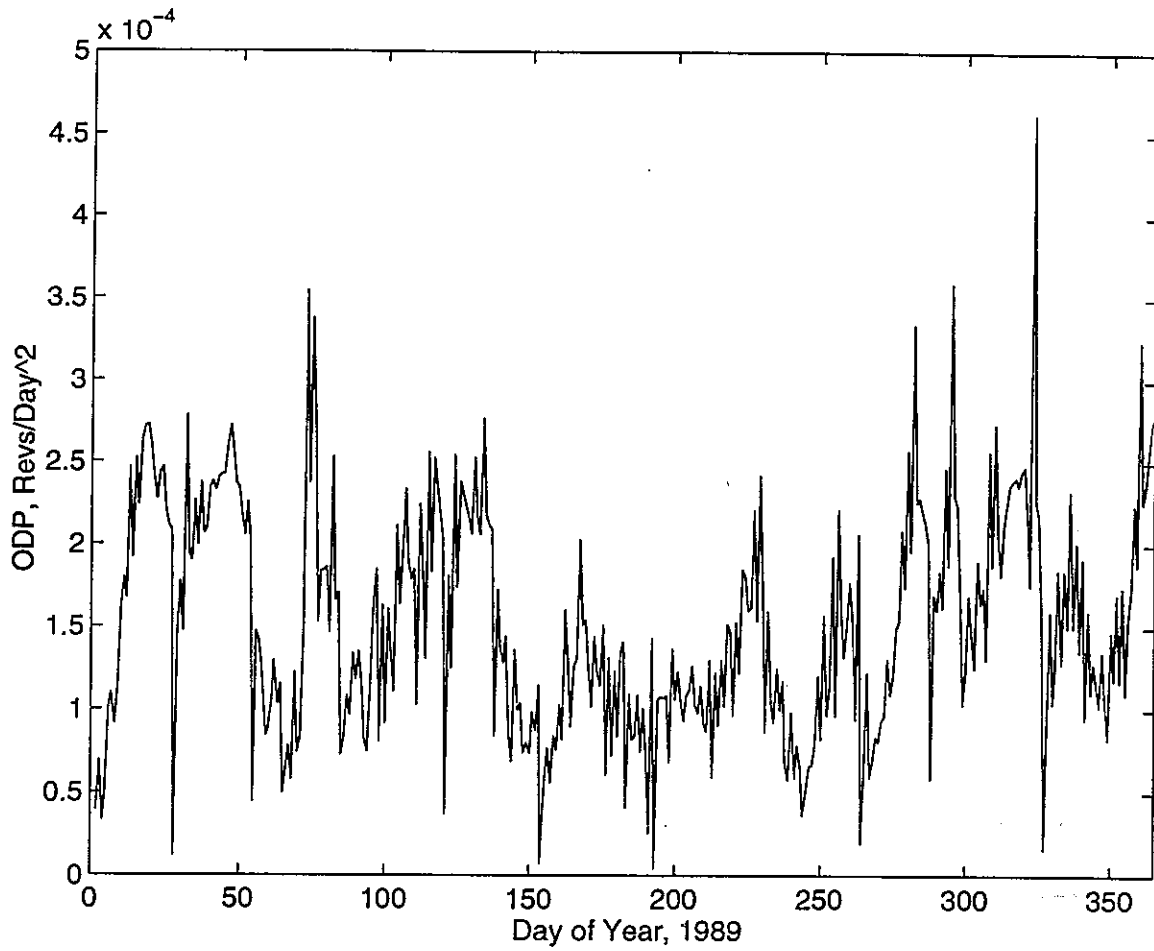


Figure 3: ODP of Cosmos 1220 during 1989.

in ODP most likely due to changes in atmospheric density. To verify whether ODP variation is driven by changes in density, the factors that influence density and hence drag must be examined.

Sources of Density Variation

Prior to correlating the ODP of a satellite to predicted density at perigee, it will be useful to understand the major sources of density variation. Atmospheric density has many sources of variability that greatly effect the drag of a LEO satellite as it passes through perigee or the point of closest approach to the Earth. Some of these fluctuations are due to variations in altitude, solar activity, solar rotation, geomagnetic activity, diurnal or day/night variations, the seasonal-latitudinal variation (SLV) and the semi-annual variation. How well a model predicts each of these variations in density is measured by the amount of correlation between the density predicted by the model and the ODP of a satellite, and therefore will be used to rank the quality of each atmospheric model.

Solar and Geomagnetic Activity

A major source of variation in upper atmospheric density is caused by fluctuations of the solar EUV flux and solar wind. To help understand how these factors affect satellite drag, the daily solar 10.7 cm radio flux $F_{10.7}$, and the daily geomagnetic index A_p , were plotted for the year 1989 in Figure 4.

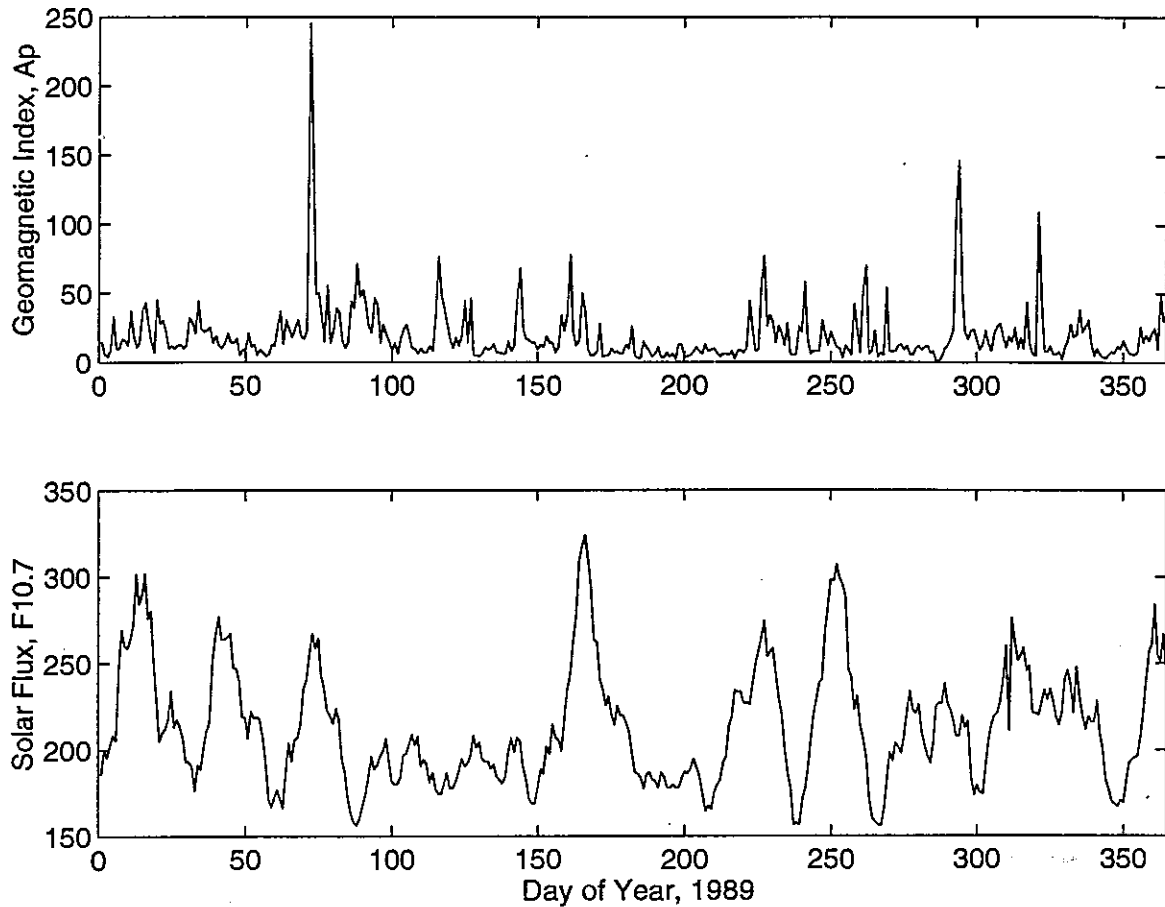


Figure 4: Daily solar flux and geomagnetic activity during the year 1989.

The upper plot displays geomagnetic activity revealing several distinct spikes in A_p on a background of lower amplitude activity. The spikes illustrate the three significant geomagnetic storms that occurred during 1989. The lower plot of the solar radio flux shows “quasi-periodic” variations that correspond to the sun’s 27-day solar rotation.

These trends in the solar and geomagnetic activity should be clearly visible in the ODP data and also the density data output from an atmospheric model if that model contains an adequate representation for such phenomenon.

To test this assumption, Figure 5 was constructed as a combination plot of atmospheric density indicated by the MET²¹ model, ODP of Cosmos 1220, geomagnetic index A_p , and solar radio flux $F_{10.7}$ during 1989.

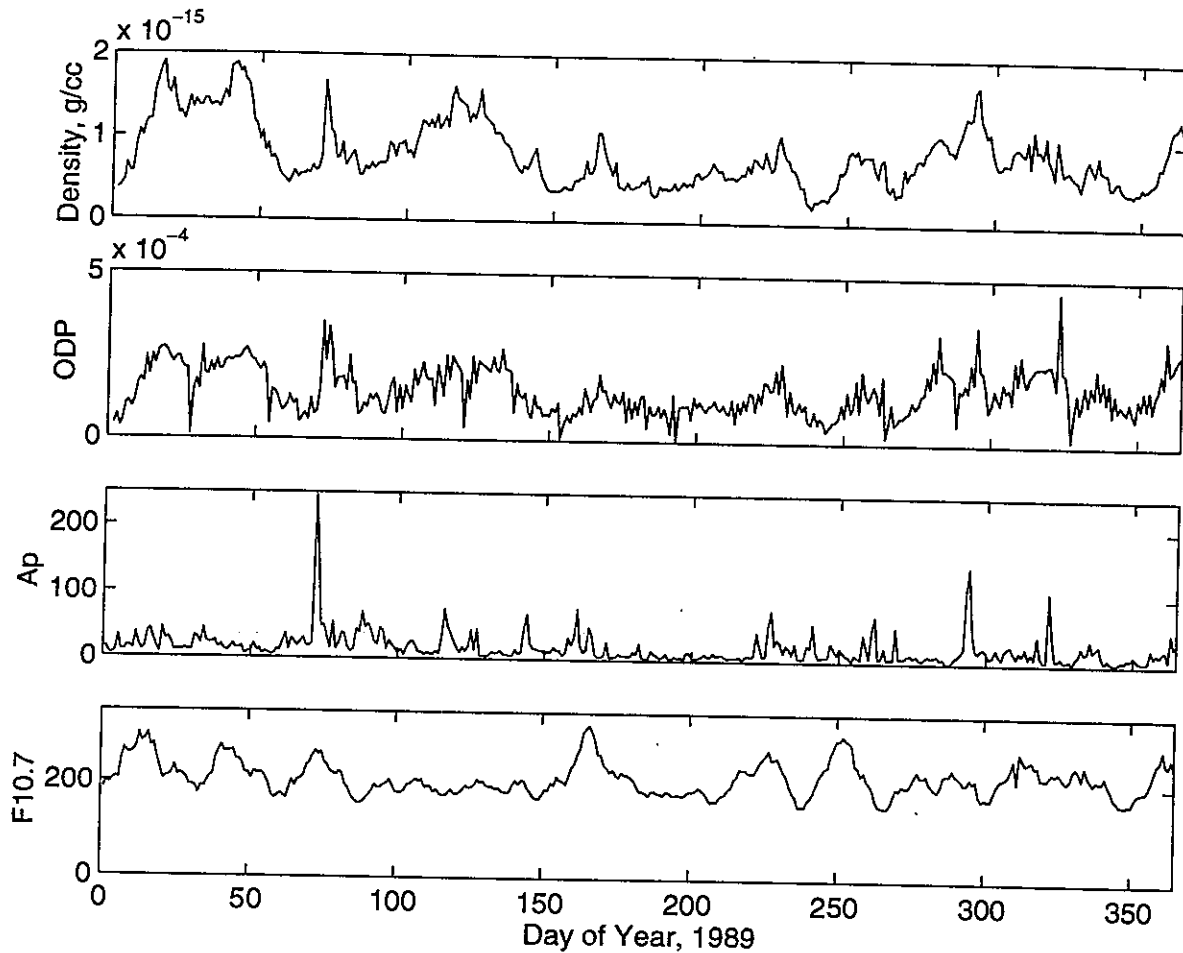


Figure 5: MET density, ODP of Cosmos 1220, A_p , and $F_{10.7}$.

The various trends of both the geomagnetic effect and solar activity can be clearly seen in both the ODP of Cosmos 1220 and the density predicted by MET. For instance, in the early part of 1989 there were a series of three broad peaks in the solar radio flux, reaching well over $250 \times 10^{-22} \text{ W m}^{-2} \text{ Hz}^{-1}$. The third peak was accompanied by the third largest

storm in the past sixty years, occurring on the 72nd day of the year.⁴⁰ The plot of Cosmos 1220 ODP and predicted density show three corresponding peaks during this period. Specific spikes and trends in the ODP curve can be attributed to the appropriate factor by directly comparing plots of those factors with the plot of ODP.

Diurnal, Seasonal-Latitudinal, and Altitude Effects

To help illustrate diurnal or day/night variational effects in satellite ODP plots, local solar time (LST) and latitude of perigee were calculated. Figure 6 shows plots of LST and latitude of perigee for Cosmos 1220.

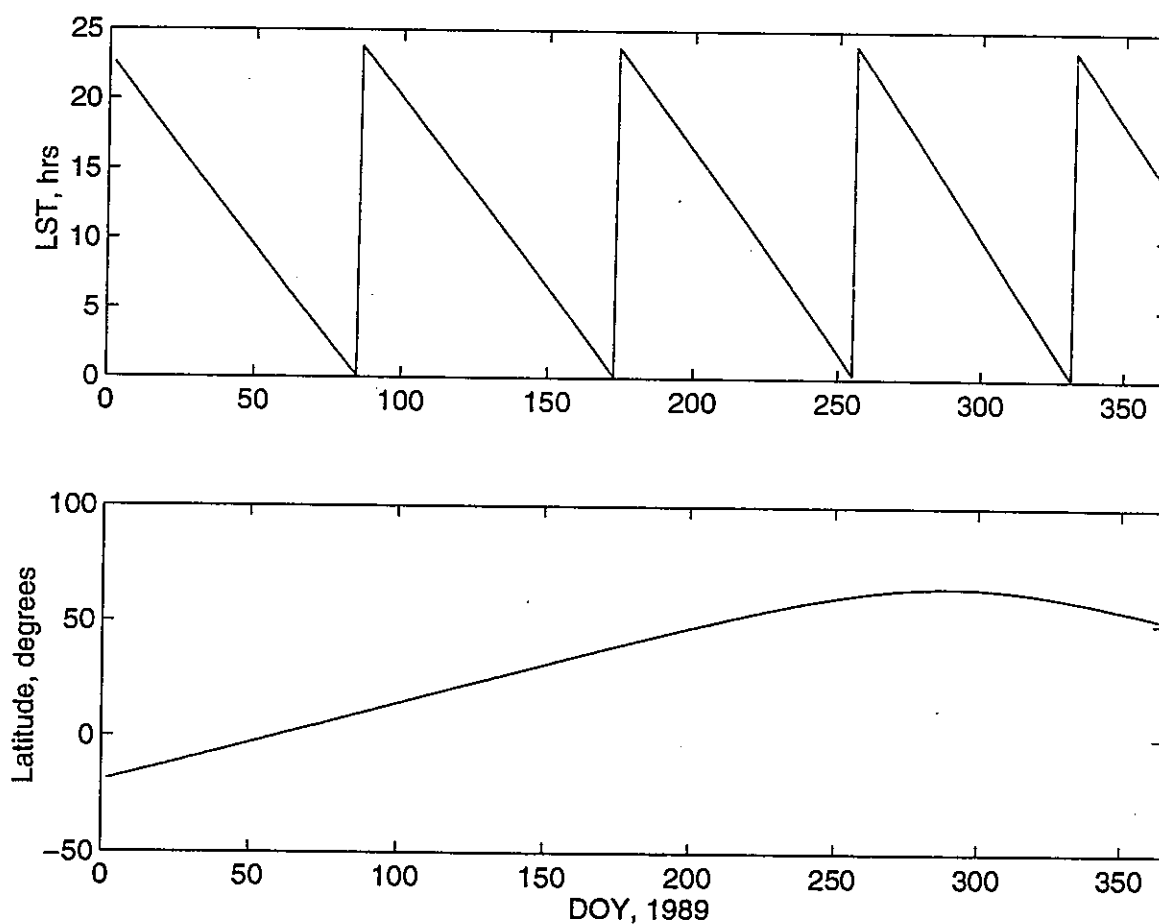


Figure 6: LST and latitude of perigee for Cosmos 1220.

The top plot reveals that the LST[†] of perigee for Cosmos 1220 goes through several diurnal cycles throughout the year. This is mainly due to the precession of the orbital plane caused by the oblateness of the Earth. The latitude of perigee plot reveals that perigee for Cosmos 1220 is changing slowly. This is because the inclination of Cosmos 1220 is near the critical inclination of 63.4° where $\dot{\omega}$ approaches zero. With a small $\dot{\omega}$, the resultant latitude of perigee will vary slowly.⁴²

To assist in interpreting the effect that altitude variation had on density and ODP for Cosmos 1220, the height of perigee and the density scale height, H, were calculated,

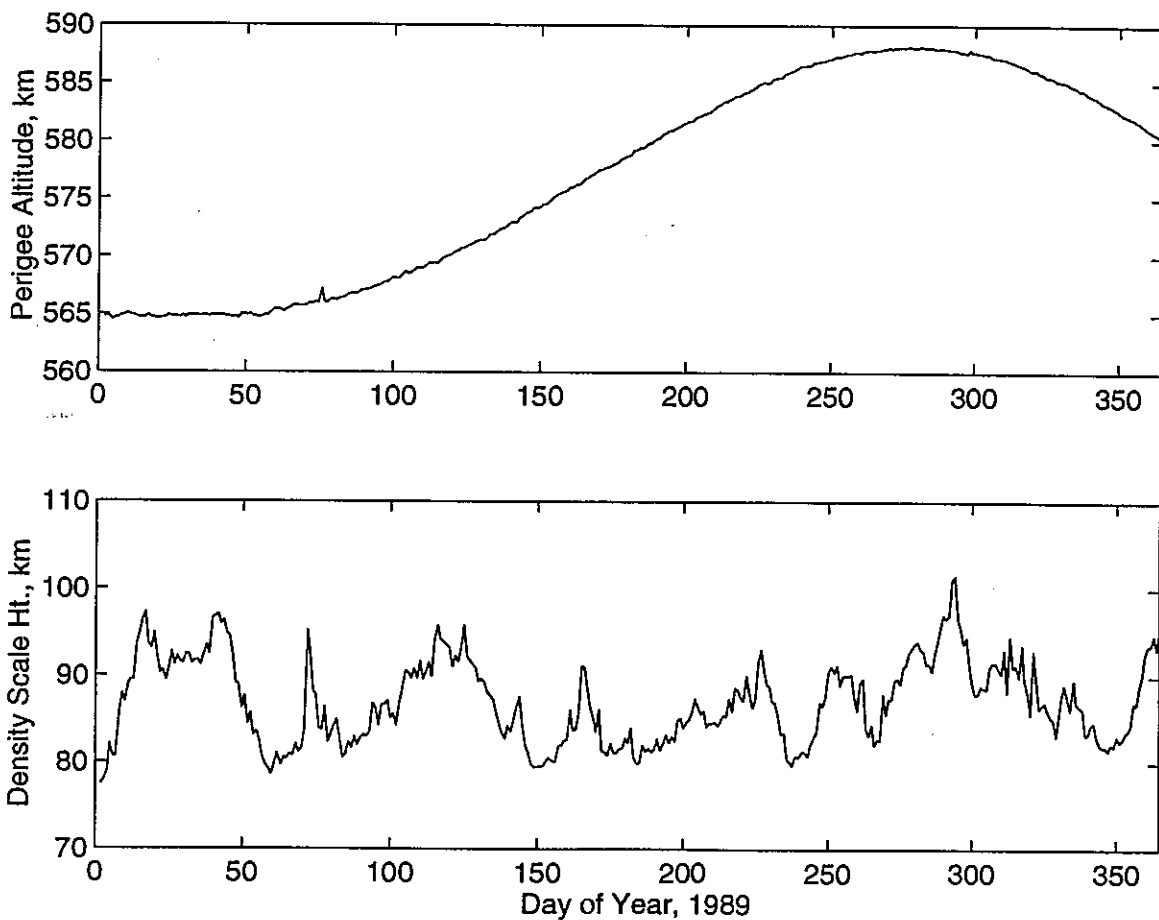


Figure 7: Perigee altitude and density scale height for Cosmos 1220.

[†] LST equals zero at midnight.

with results shown in Figure 7. The top plot shows that the perigee altitude of Cosmos 1220 increases gradually, with a variation of 20 km throughout the year. Variation in perigee altitude occurs primarily due to the oblateness of the Earth. The bottom plot displays the values for the density scale height, and reveals that H is fairly constant, with an average of approximately 85 km. Because the change in perigee altitude for Cosmos 1220 is only about 25% of the density scale height, altitude changes will represent approximately 22% of the total changes in ODP for Cosmos 1220, meaning that the majority of the changes in density and ODP will be the result of variations in other factors such as solar flux and geomagnetic activity.

Correlation of Models to ODP

To begin the comparison of atmospheric models to Cosmos 1220 ODP, model inputs were calculated over a period of a year from daily satellite orbital elements. The National Oceanic and Atmospheric Administration (NOAA) supplied solar and geomagnetic inputs. Atmospheric density was then calculated at perigee over the entire year for each of the models described in Chapter 3. Once this was completed, a LS fit was performed fitting daily, predicted density to the daily change in mean motion using the following linear form:

$$\text{ODP}_i = A\rho_i \quad (21)$$

This form was chosen for its simplicity, and due to ODP, *i.e.*, \dot{n} , being linearly related to ρ as shown in the orbital decay equations (1), (4), and (5). In addition, ODP should approach zero when density approaches zero.

MET Model

Figure 8 shows a scatter plot of Cosmos 1220 ODP relative to the linear estimate calculated using MET densities in (21). The plot reveals that the relationship between ODP and density is mostly linear, however, there is considerable noise present.

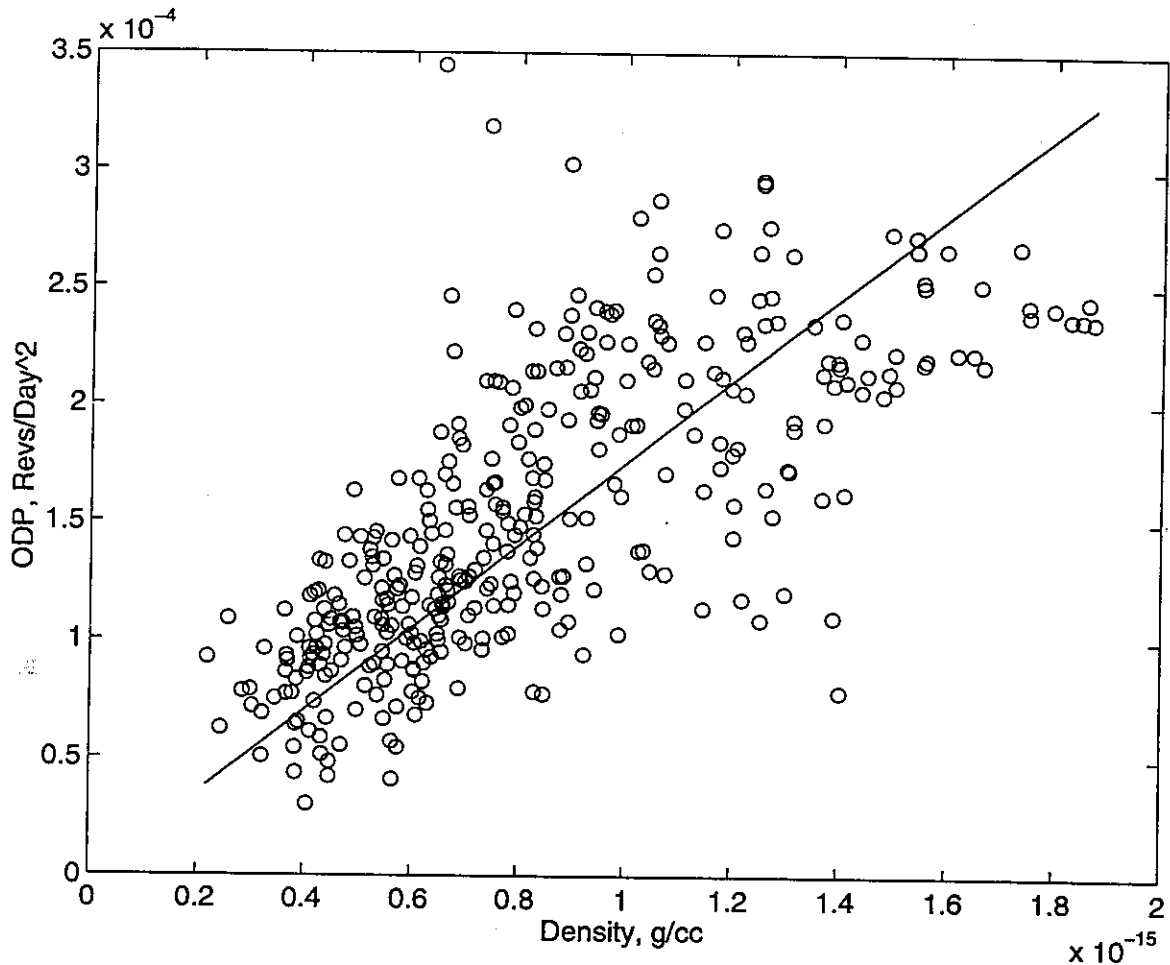


Figure 8: LS fit of MET density to the ODP of Cosmos 1220.

The upper part of Figure 9 shows a plot of density as calculated by the MET model using Cosmos 1220 element sets. The lower plot shows Cosmos 1220 ODP from element sets, (solid line), compared to the linear approximation to ODP using (21) with MET density at

perigee (dash-dot). Clearly there is good correlation, but a phase-lag exists between the actual ODP and that predicted by MET as indicated by the ODP spikes of Cosmos 1220

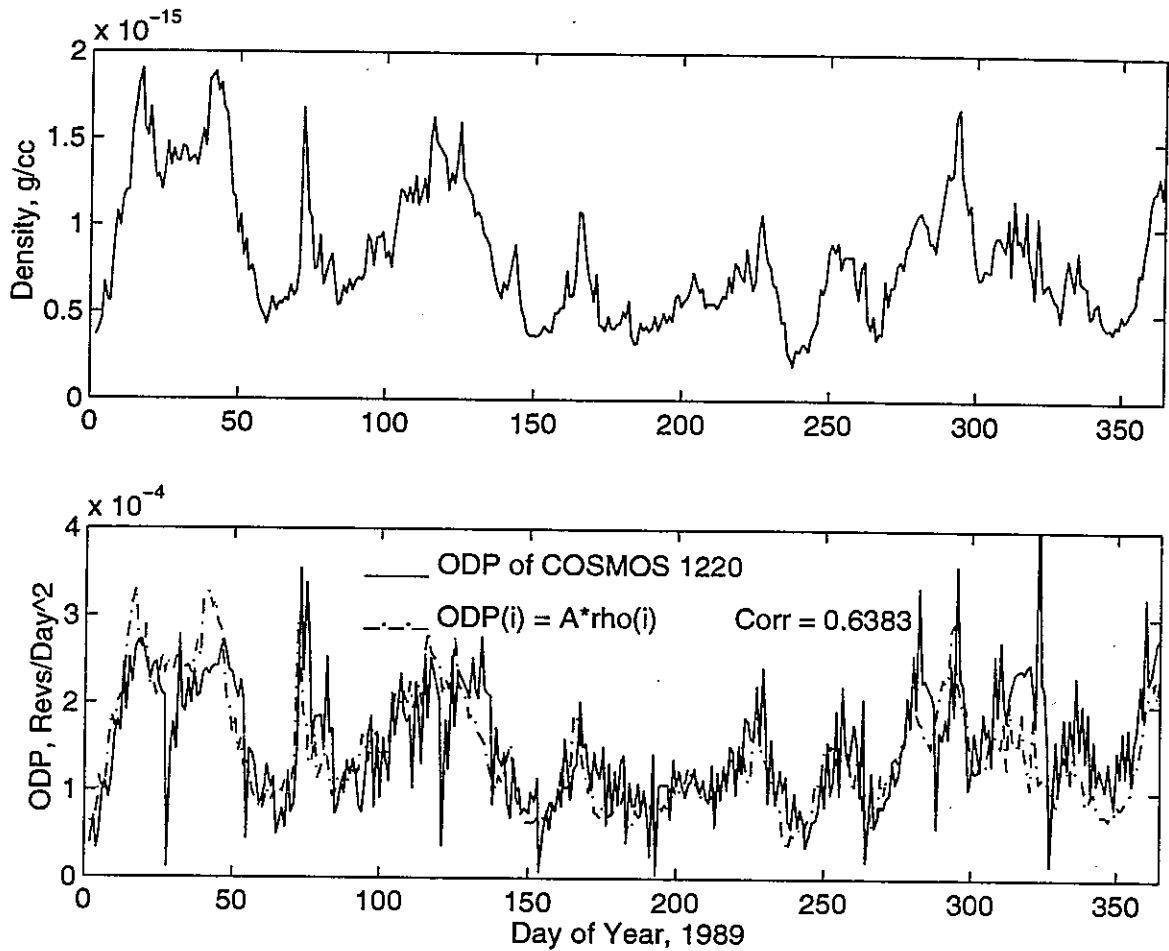


Figure 9: MET density fit showing a phase lag with ODP of Cosmos 1220.

appearing to the right of those estimated by MET. The plot of ODP also indicates a process bias exists and/or an element of noise is present, as suggested by the spikes in the negative direction that typically follow large corrections to ODP made by the DC process. This may be due to over-correction of ODP. In addition, the increases in density associated with the two geomagnetic storms that occurred on DOY 72 and 293 are fairly well predicted, yet the density effects from the storm that occurred on DOY 322 are

extremely under-predicted. This reveals the geomagnetic effect of the MET model most likely needs additional development. But despite the lag, noise, and under-estimation, MET generated densities have a 0.64 correlation with ODP from the element sets. Recalling the method that was used to generate the ODP contained in the element sets discussed in Chapter 4, the existence of a lag between the atmospheric disturbances in density and ODP should be expected.

To remove this lag and reduce the process bias contained in the ODP values, running averages were calculated for ODP and density using consecutive data points and a phase-shift was introduced into the LS expression in the following form

$$\text{ODP}_i = C\rho_{(i-k)} \quad (22)$$

where $\rho_{(i-k)}$ represents the previous density value at perigee, approximately k -days earlier than ρ_i . The actual amount of phase shift was dependent upon the frequency of the DC updates to the elements. For Cosmos 1220, updates to the elements occurred an average of 1.01 days apart. Thus a fixed phase shift in time of an integer number of days was not possible, and hence the need to express this temporal shift as a k -day phase shift, where the value k of a satellite is approximated by the average time between updates to the elements. Therefore, for the case of Cosmos 1220, k would be approximately 1.01 days. Introducing the phase shift in density will counter the apparent temporal lag in ODP and should result in a higher correlation. Ideally, density should have been averaged over the entire data fit-span to match the smoothed ODP from the differential correction (DC) process, but because the fit-spans were unknown, averaging density over the data span was not possible.

Figure 10 shows the results for Cosmos1220 after performing a LS fit using a running mean of both density and ODP along with a zero and a 1k-day phase-shift in density as calculated by the MET model. The top plot of Figure 10 shows the effect on the correlation using running means of consecutive ODP and density values. The bottom plot shows the additional increase in correlation due to the introduction of a 1k-day phase shift in density.

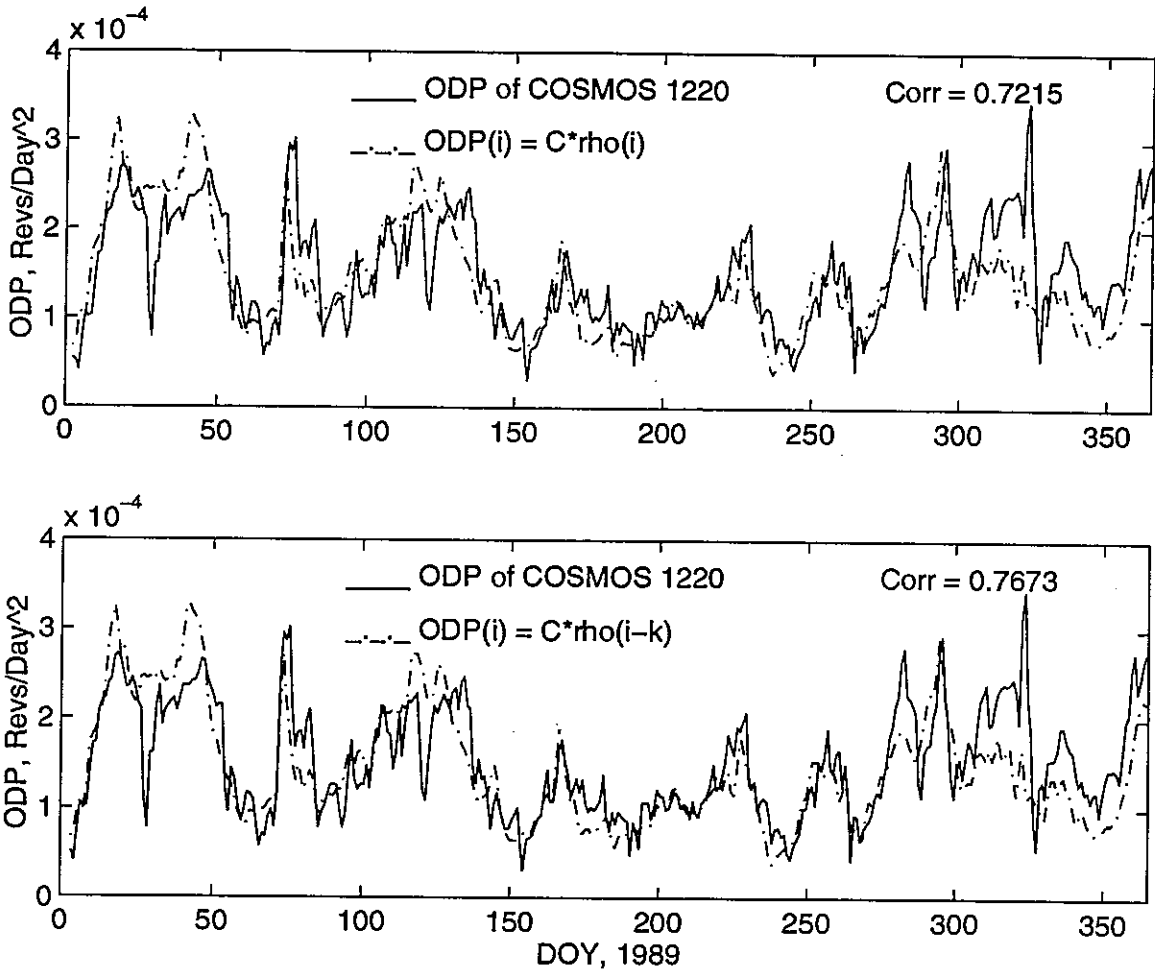


Figure 10: Correlation of MET to Cosmos 1220 using phase shifts of 0 and 1k-day.

There is still a lag visible between the density and ODP. Therefore, the lag in density was increased to 2k and 3k-days with the results shown in Figure 11. The top plot shows the

results corresponding to a phase-lag of $2k$ -days whereas the bottom reveals the effect of a phase lag of $3k$ -days.

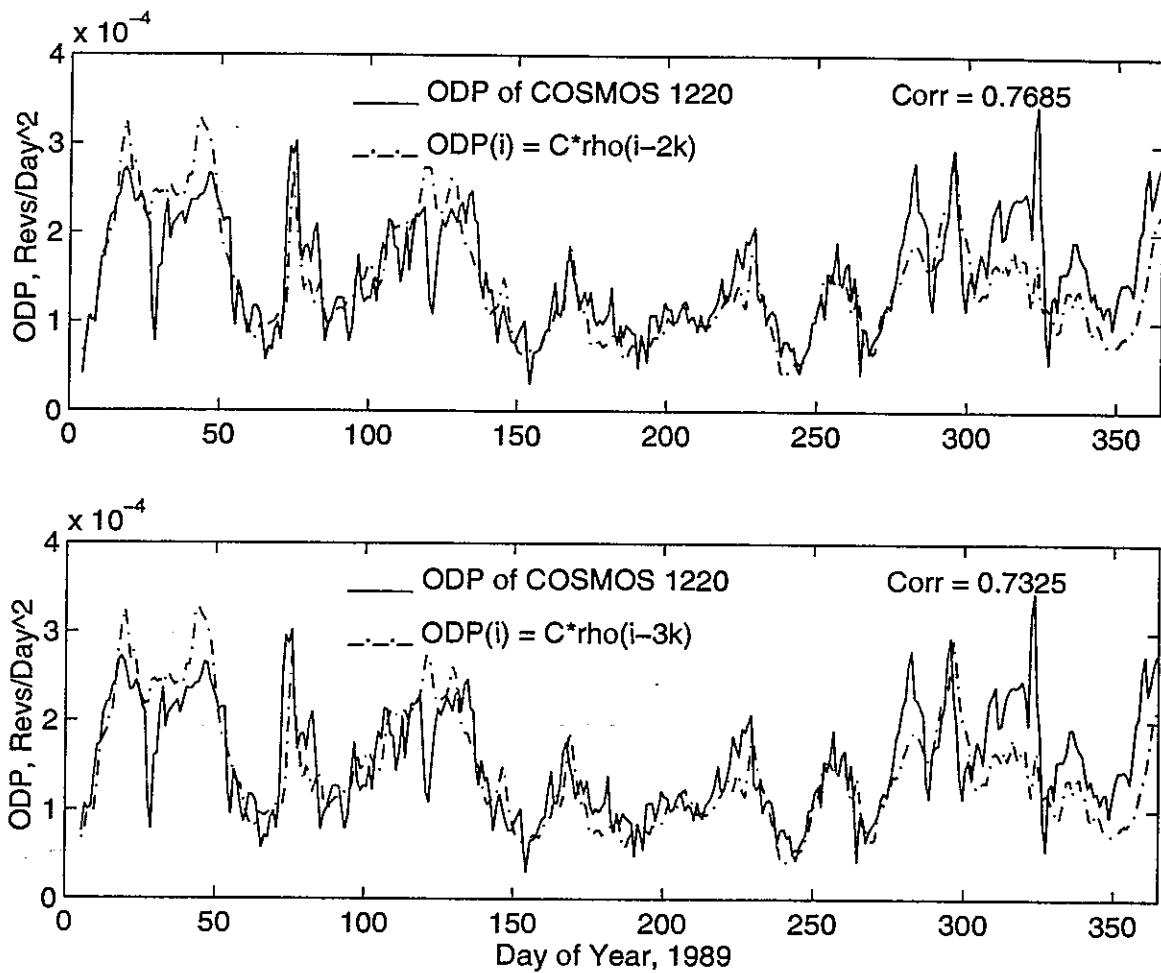


Figure 11: Correlation of MET to Cosmos 1220 using phase shifts of $2k$ and $3k$ -days.

Since the correlation decreased for a phase shift of $3k$ -days, the above plots suggest that the optimum phase shift in density for Cosmos 1220 lies between $1k$ and $2k$ -days. This can be illustrated by plotting the variation in correlation versus the amount of lag applied to the density model as shown in Figure 12.

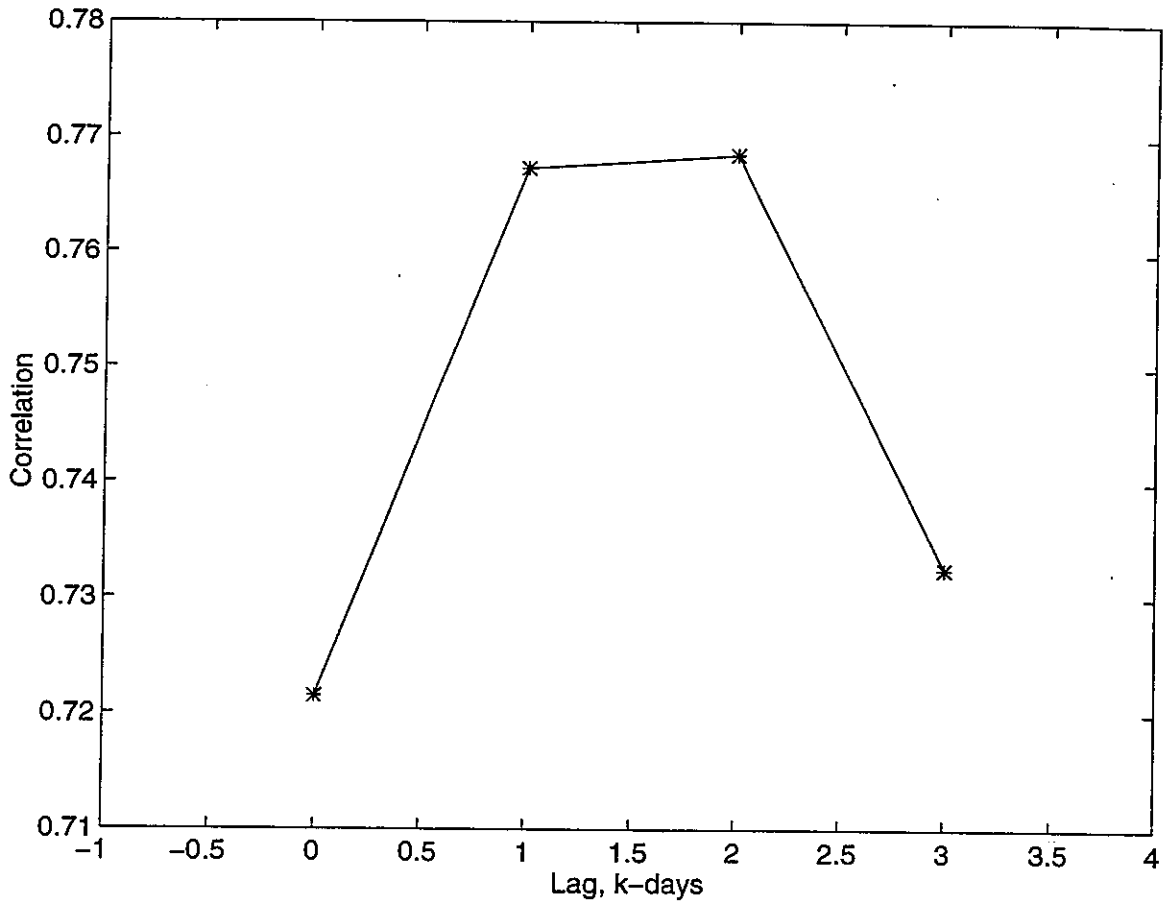


Figure 12: MET correlation vs. density lag.

The existence of a lag in ODP will have a serious impact on fence crossing predictions most notably during a period of severe atmospheric disturbance. This disturbance in density and drag will not be directly input into the orbit prediction model because the orbit model does not contain an atmospheric model. The only way this change in density and drag can manifest itself into the orbit predictor model is through DC of ODP. However, recall the discussion in Chapter 4 regarding the processing of lengthy data-spans of radar fence observations. The updates to ODP from the DC process will be an averaged solution, that is the “best fit” over the entire span of observations and lagging

up to several days, depending on the fit-span length of the data. Therefore, the DC process can not provide the sharp corrections necessary to ODP during periods of severe atmospheric disturbance. The end result will be large fence crossing errors during extreme solar storms, and thus UCT's.

However, applying the ODP model just developed without using a phase lag would eliminate the lag between the orbit model and the atmospheric perturbations. The phase lag is a process bias formed as a result of applying the DC method to ODP over a length of data, and was introduced into the ODP model to match this process bias and get a more representative correlation between model densities and observed ODP values. By applying the ODP model using atmospheric density predicted at the time of perigee, a lag will not exist between density and the estimate for ODP, which then could be used in conjunction with the existing orbit model to potentially reduce the number of UCT's occurring during severe solar storms.

MSIS-86 Model

Similar results were found for the MSIS-86 atmospheric model, but differences in model structure are apparent. Results are shown in Figure 13 and Figure 14 where the phase shifting techniques were applied. As previously, the solid line is Cosmos 1220 ODP, whereas the dash-dot line represents the estimated ODP calculated using a LS fit of the density at perigee predicted by MSIS-86 to actual Cosmos 1220 ODP.

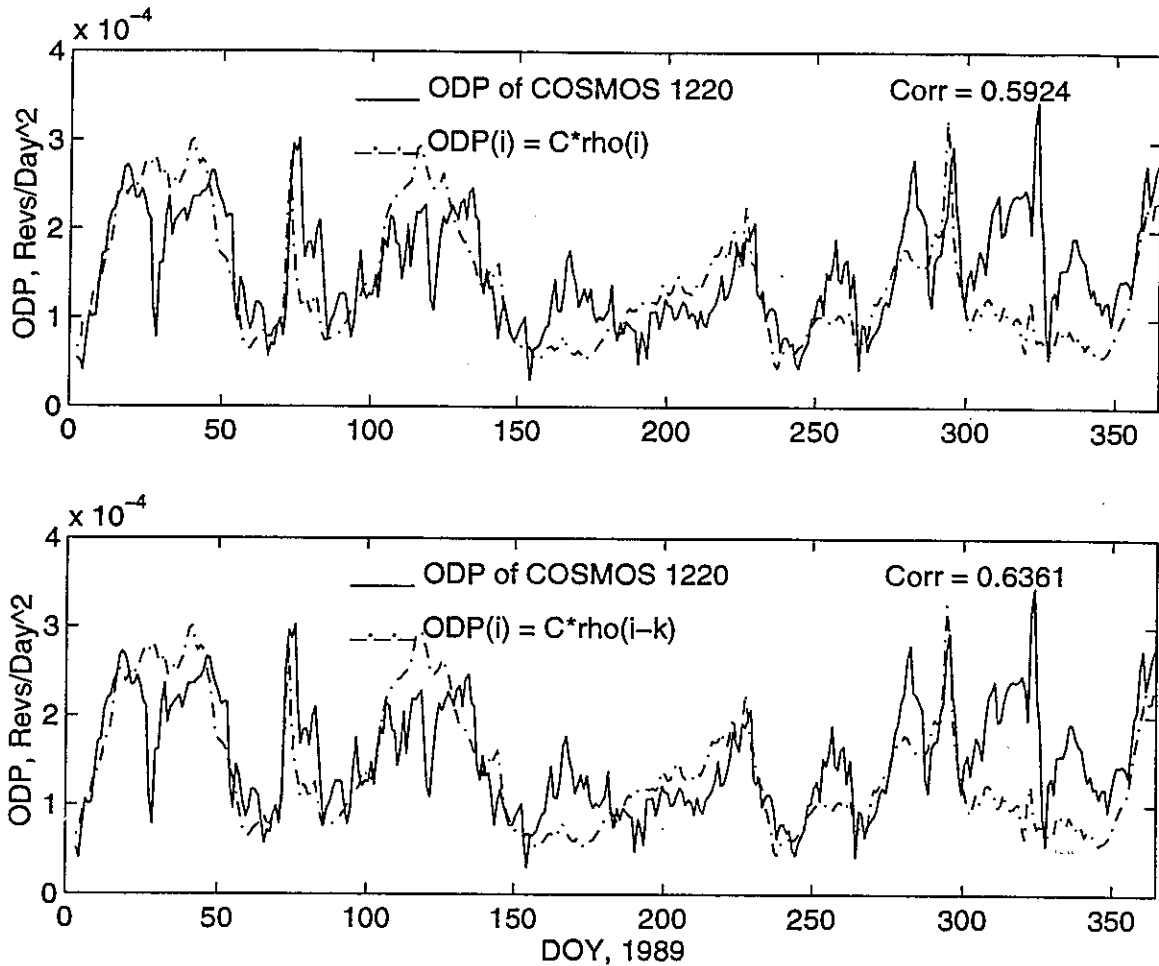


Figure 13: Correlation of MSIS-86 to Cosmos 1220 using phase shifts of 0 and 1k-day.

The results are similar as with the MET model, but there are several time periods where the MSIS-86 model estimates for ODP are lower than MET estimates, as occurs on DOY 170 and 260. On the contrary, MSIS-86 predicts higher density than MET for the geomagnetic storm on DOY 293, suggesting that the MSIS-86 model is representing the geomagnetic effect on density more accurately than MET. However, despite the periods of greater density prediction, it is apparent that density under prediction is more prevalent, given the lower correlation of MSIS-86 to Cosmos 1220.

Under or over-estimation of ODP is undesirable. An appropriate atmospheric model must be able to properly estimate the major contributors to density variation as outlined earlier in this chapter. A model that has diurnal and seasonal latitudinal variations represented, but does not estimate the solar flux or geomagnetic impacts to density accurately, will not be a very useful atmospheric model for the purposes of eliminating UCT's caused by solar storms.

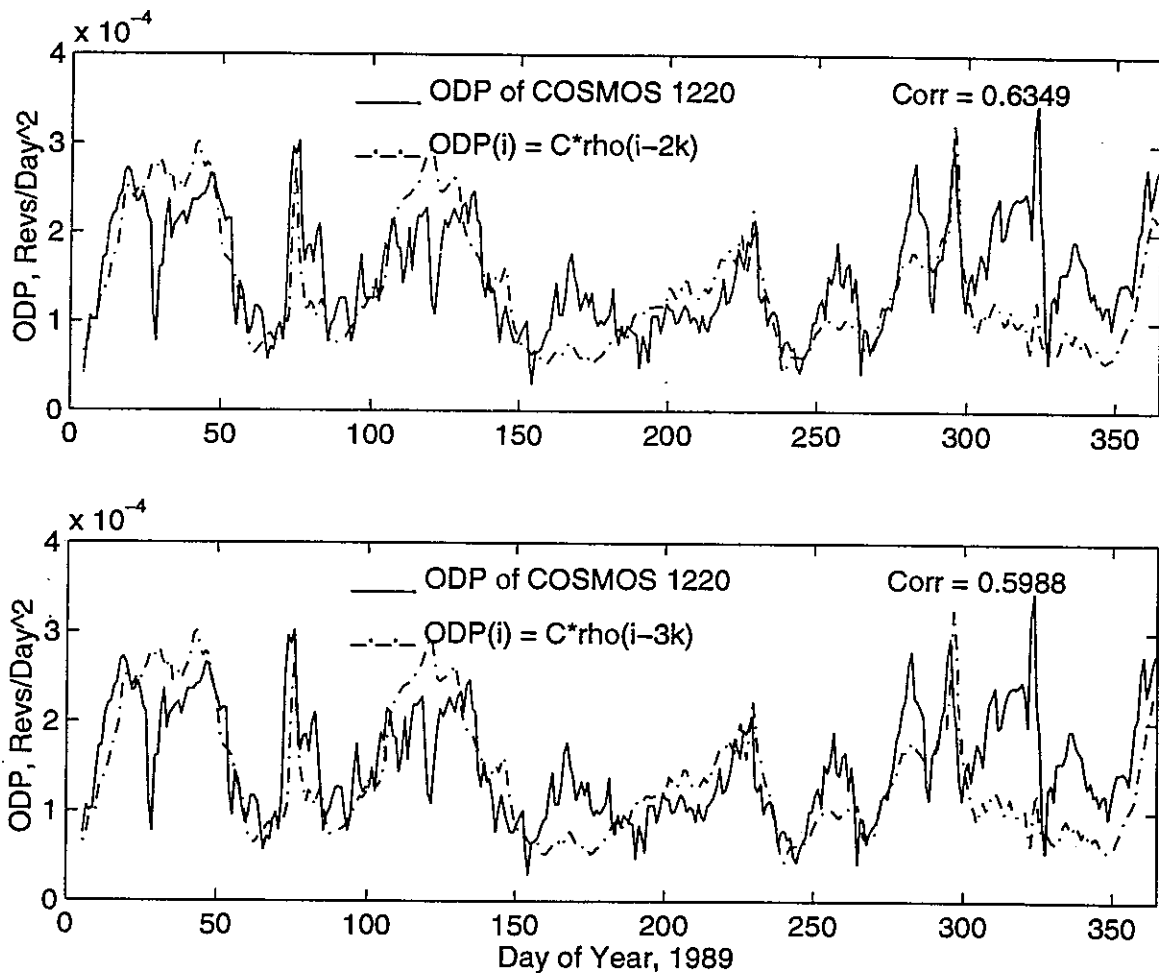


Figure 14: Correlation of MSIS-86 to Cosmos 1220 using phase shifts of 2k and 3k-days.

Referring back to Figure 4 which shows the solar flux and geomagnetic activity during 1989, the time periods of under-estimated MSIS-86 density coincide with periods of high solar activity, suggesting that the coefficients governing the solar flux perturbations to MSIS-86 density need adjusting.

J71 Model

Figure 15 and Figure 16 show the results of the LS fit of the J71²² model to Cosmos 1220 ODP for various phase shifts in density.

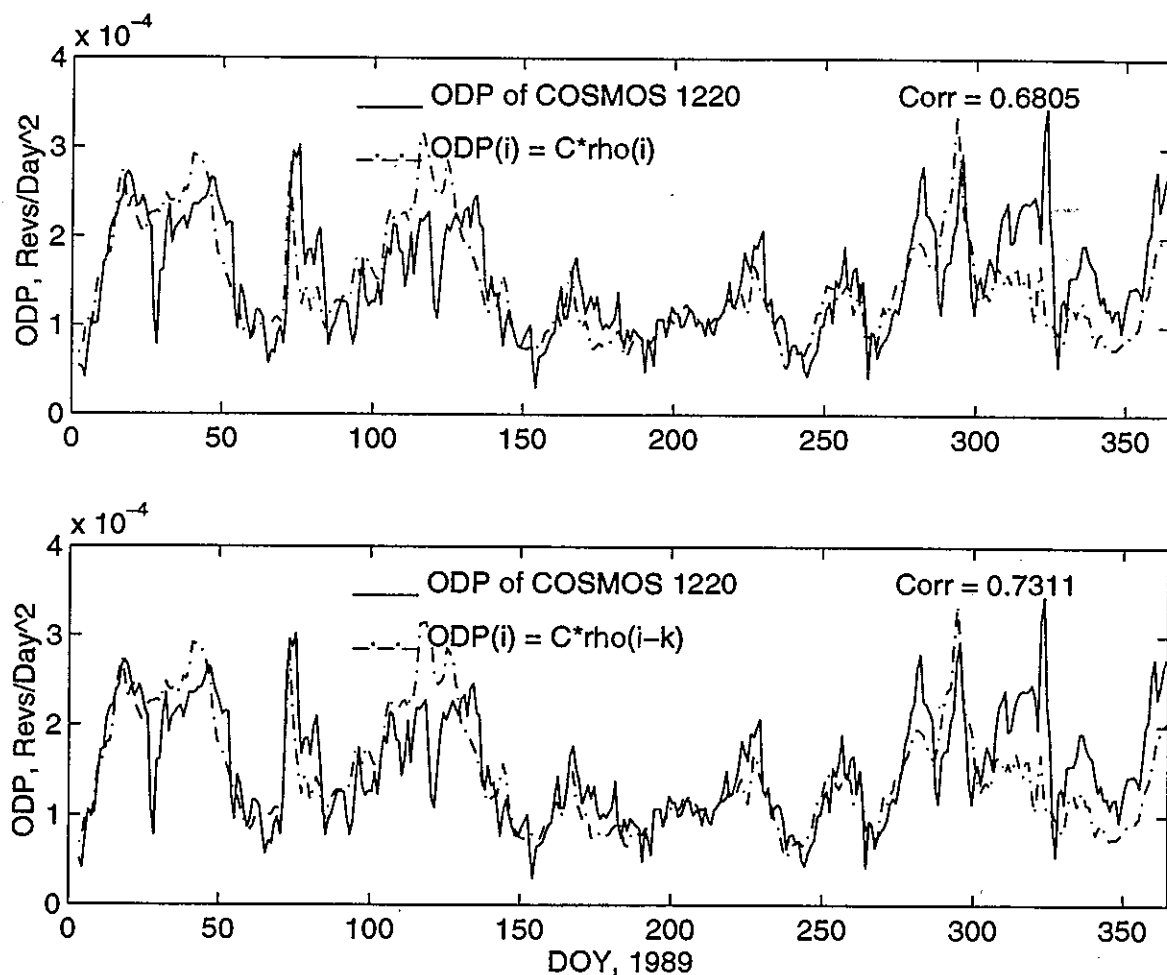


Figure 15: Correlation of J71 to Cosmos 1220 using phase shifts of 0 and 1k-day.

Very similar results to the MET model can be seen. However, notice that the J71 estimate for ODP associated with the A_p storm on DOY 293 is, as in the MSIS-86 case, greater than the corresponding MET estimate for ODP, implying that the disturbances in density

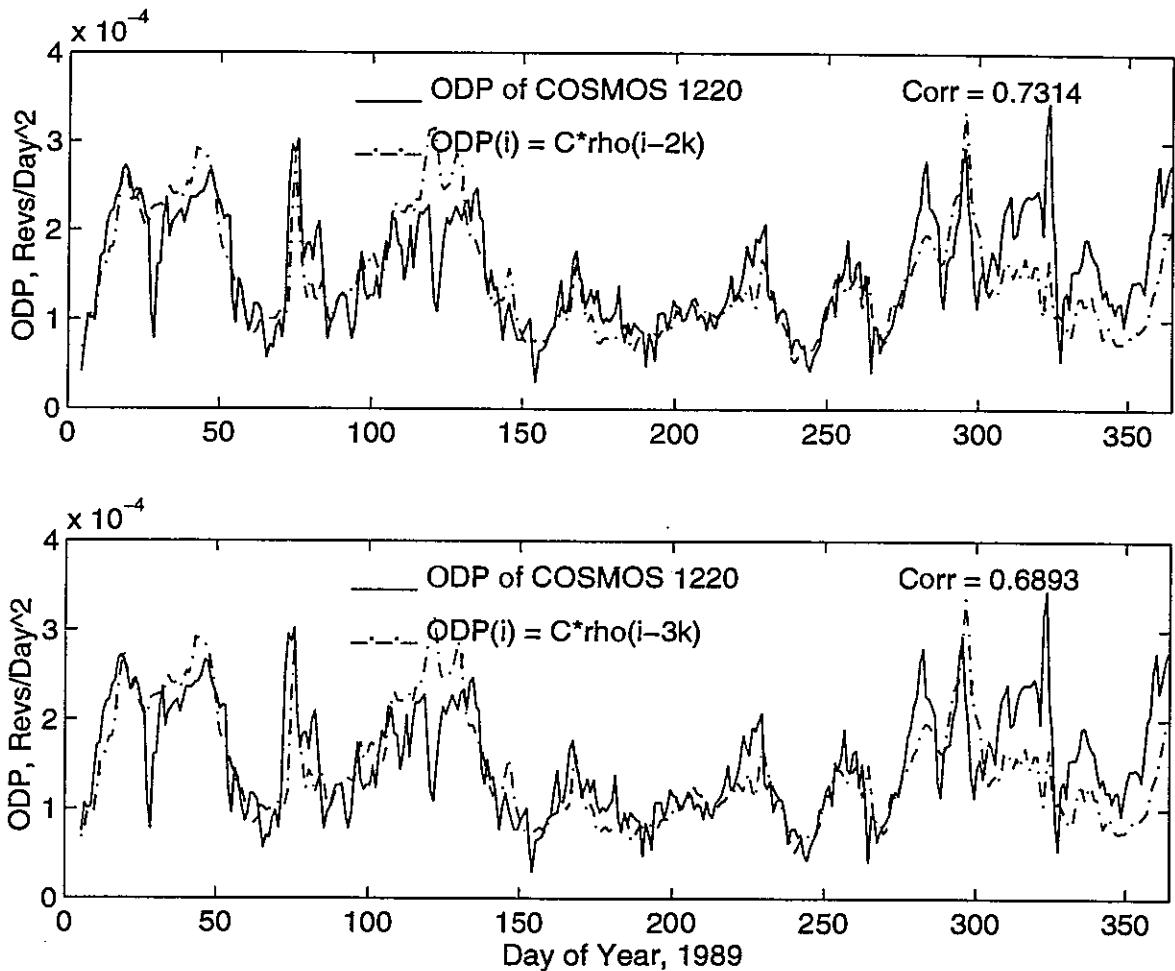


Figure 16: Correlation of J71 to Cosmos 1220 using phase shifts of $2k$ and $3k$ -days.

that occurred on this day due to the geomagnetic effect may be more accurately represented by the J71 and MSIS-86 models.

J77 Model

The Jacchia 77 model was evaluated using the same procedure as for the other models, with results shown in Figure 17 and Figure 18.

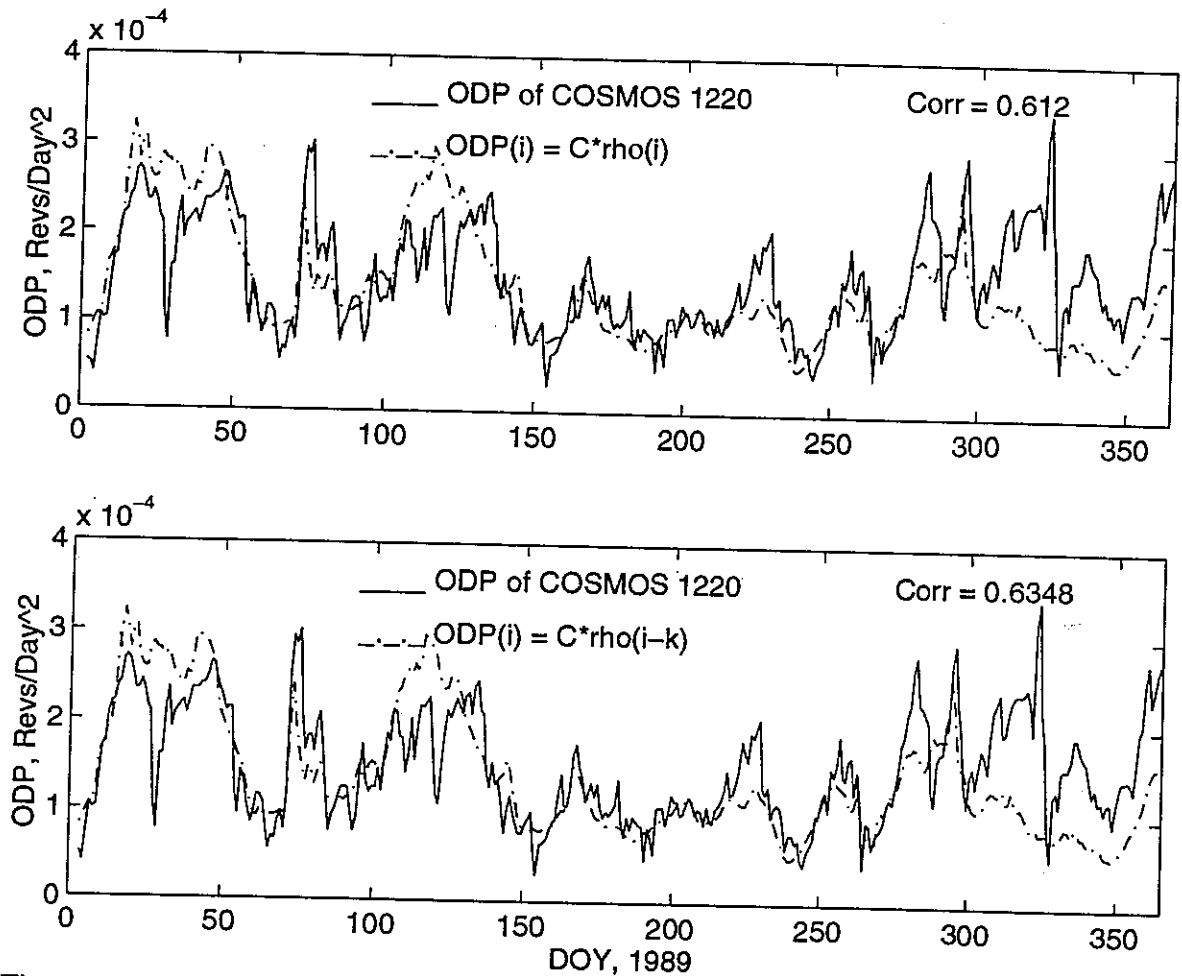


Figure 17: Correlation of J77 to Cosmos 1220 using phase shifts of 0 and 1k-day.

A general inspection of the J77 estimate for Cosmos 1220 ODP suggests that J77 does not predict total density as well as the other models. The spikes in ODP due to the three severe geomagnetic storms that occurred on DOY 72, 293, and 322 are all under-

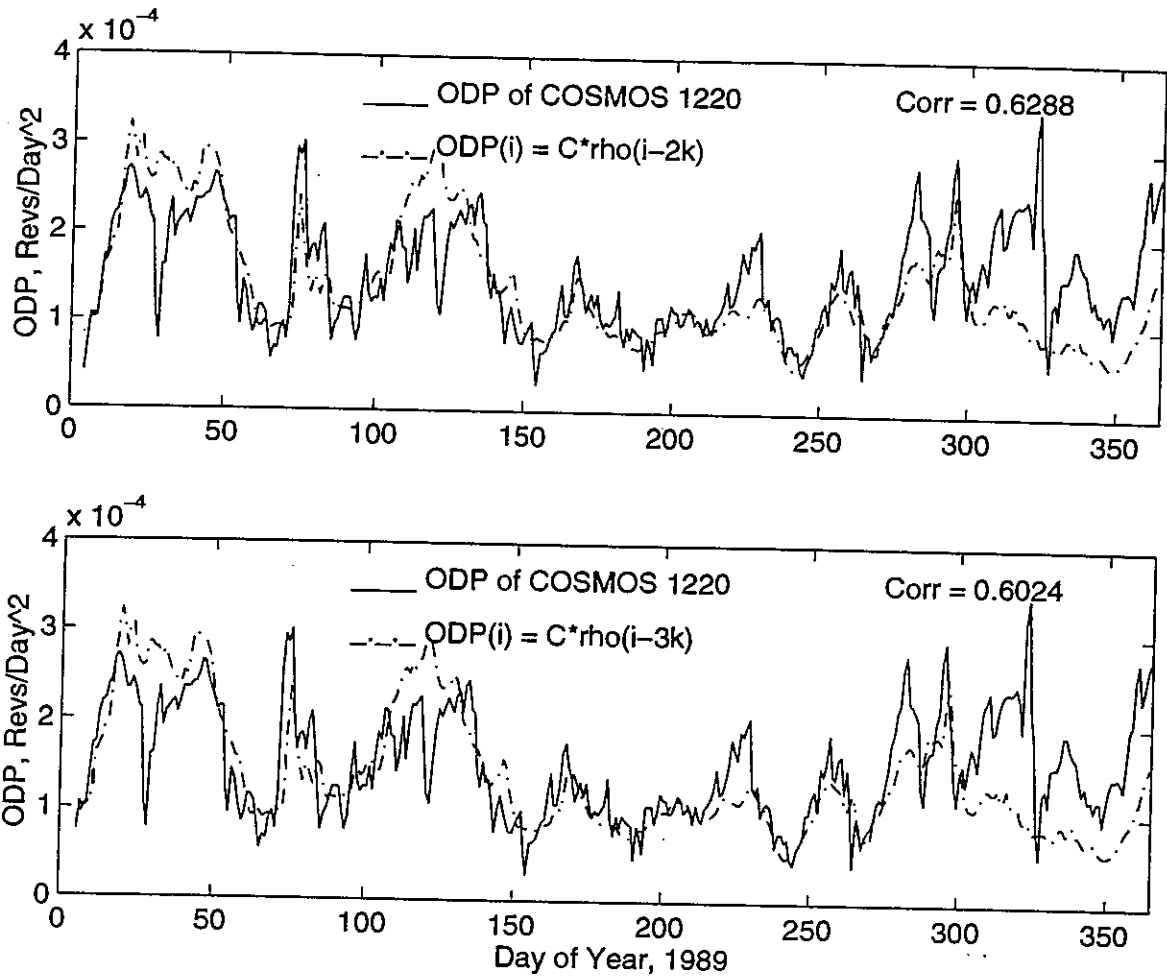


Figure 18: Correlation of J77 to Cosmos 1220 using phase shifts of 2k and 3k-days.

estimated, considerably more than any of the other models.

Analysis of Model Performance

In comparing the responses of all four models, differences arise in how well they match fluctuations in ODP. The majority of these disturbances in ODP are most likely caused by variations in the solar flux and geomagnetic activity, as suggested earlier in the sub-section entitled "Geomagnetic and Solar Activity". Comparing Figure 11 and Figure

14 showing the correlation of the MET and MSIS-86 models to ODP respectively, reveals that the MET model responds stronger and with better resolution to variations in solar flux than does the MSIS-86 model in this particular case. Another interesting region lies in between days 170 and 225 of the year. Both the beginning and the end of this period are characterized by strong increases in the daily solar flux. The result forms a semi-circular shape in the ODP curve. The MET model responds strongly to the $F_{10.7}$ variation both at the 160-day mark and the 225-day mark. On the other hand, the MSIS-86 model shows very little response at the 170-day mark, but estimates the 225-day peak fairly well.

The response of J71 to geomagnetic activity is most similar to MSIS-86 predictions. However, J71 estimates for density are slightly higher as can be seen by comparing Figure 14 and Figure 16 on DOY 72 and 293. For changes in density due to solar flux changes, J71 and MET are most alike. Nonetheless, in comparing Figure 11 and Figure 16, it can be seen that J71 predicts lower density than MET on days 15, 40, and 170. But on day 225, the difference is only slight, and on days 125 & 290, J71 is considerably larger than MET. There is an apparent difference between the two models that seems to appear semi-annually. This phenomenon behaves similarly to the semi-annual variation (SAV) which generally peaks twice a year, once in the spring and once in the fall. SAV implementation differs between these two models and could be the reason for the observed contrast. In MET, the change in density due to SAV is represented by a correction to exospheric temperature, T_{∞} , that is a function of time of year and solar radio flux. In contrast, J71 represents SAV by a direct correction to density that is a function of altitude and time of year, but eliminates any functional dependency on solar flux.⁴³

The models were fair when it came to reacting to geomagnetic events. Recall Figure 4 showing the geomagnetic and solar activity throughout 1989. There were three main geomagnetic events, occurring on days 72, 293, and 322. All models responded fairly well to the first two geomagnetic storms by correctly estimating a sharp rise in ODP. However, the last storm was extremely under predicted by all of the models. Key variables for determining atmospheric density were identified for the three storms in an effort to isolate a possible cause or deficiency in the models. The severity of the three storms happened to decrease for days later in the year, meaning the order of the storms in decreasing strength was day 72, 293, and 322. Upon inspection of the ODP plot, the order appeared to be contradictory, since the largest spike in ODP occurred during the weakest storm. In contrast, it would be expected that the largest geomagnetic disturbance would create the greater increase in density, all else being equal. However, after examining other variables it was determined that perigee for Cosmos 1220 occurred at low latitude during the largest geomagnetic event and was located at 65° and 60° for the other storms, respectively. This would help explain why ODP was smaller for the first storm when Ap was 249, compared to the third storm with an Ap of 138, since Cosmos 1220 perigee occurred close to the north geomagnetic pole of the Earth for the third storm[‡]. It is in the magnetic polar regions of the thermosphere where thermal and density effects from geomagnetic activity would be greatest.⁴⁴ Nonetheless, this does not explain why ODP for the second largest storm on day 293 was smaller than the ODP that took place during the weaker storm on day 322, since perigee was even closer to the north

[‡] The north geomagnetic pole occurs at a geodetic latitude of 78.6° and a longitude of 289.3° .

geomagnetic pole during the stronger storm on day 293. If LST of perigee is considered, the resultant behavior of ODP is explained. During the weaker storm on day 322, LST was approximately 3 AM, whereas during the stronger storm on day 293, the LST was approximately 12 Noon. Geomagnetic activity affects atmospheric density the most during the night when solar energy input is at a minimum and therefore temperature and density reach their minimums as well. Thus any addition of energy during the night is going to have a larger impact on temperature and density and therefore ODP, than an equivalent storm occurring during the day.

Having reasonably explained the pattern of ODP for the geomagnetic storms, that still leaves understanding why all the models failed to estimate ODP correctly during the third magnetic storm. One possibility is the fact that none of the Jacchia models evaluated include LST or longitude in the functions that represent the changes in density due to the geomagnetic effect. LST and longitude appear to be important variables, given the difference between the effects of the geomagnetic storms on ODP during days 293 and 322 and the LST when they occurred. The J77 model contains the most complex geomagnetic modeling of all the Jacchia models, yet failed to outperform the other models. However, Hedin does use LST when factoring in geomagnetic effects in MSIS-86, but it is possible that some coefficients need adjusting.

Extended Satellite Study

To further test the approach of modeling satellite ODP using atmospheric density and continue the evaluation of the 4 atmospheric models, the study was expanded to include eleven additional satellites in various types of orbits during the year 1991.

Elevated geomagnetic activity during this period was generally more frequent than that during 1989, although the magnitudes of the storms were less severe. Table 2 summarizes the properties of the satellites, if known, including the 5-digit satellite identification number, international reference number, name, height of apogee and perigee, inclination, radar cross-section (RCS), shape, size, and mass.

Table 2: Satellite characteristics

Sat. No.	Int. No.	Name	H _a x H _p (km)	i (deg.)	RCS (m ²)	Shape	Size (m)	Mass (kg)
60	1960-014A	Explorer 8	1498 x 399	50	0.47	2x Cone	0.76 L x 0.76 Dia.	41
614	1963-025B	Hitch-Hiker 1	2759 x 330	82	0.47	Oct.	0.30 L x 0.90 Dia.	79.8
1616	1965-078A	Atlas D RB	2731 x 408	144	1.62	Cyl.	2.05 L x 0.72 Dia.	70 ?
2389	1966-70A	OV3-3	3342 x 354	81	1.01	Oct.	0.74 L x 0.74 Dia.	75
2404	1966-70B	OV3-3 RB	1286 x 318	81	0.34	Cyl.	1.5 L x 0.46 Dia.	24
3342	1968-066D	Explorer 39 Debris	1761 x 619	81	0.01	?	?	?
4222	1969-097B	Scout B RB	1621 x 364	103	1.60	Cyl.	1.5 L x 0.46 Dia.	24
8368	1975-100C	DELTA 1 RB(2)	6901 x 251	23	2.85	Sphere -Cone	1.32 Dia. to 0.94 Dia.	66
11791	1980-032B	Atlas F RB	12215 x 264	63	2.27	Cone-Cyl.	1.85 L? 0.63-1.65 Dia. ?	163 ?
12069	1980-087B	Atlas Centaur RB	9336 x 268	26	19.5	Cyl.	8.6 L x 3.0 Dia	1815
15679	1985-035C	Ariane 3 RB(3)	30156 x 264	6	15.9	Cyl.	9.9 L x 2.6 Dia.	2150 (e)

Results of the extended satellite study are shown in Table 3, which lists the satellite number, name, average time k between element set updates, the amount density was shifted in k -days, and the resulting correlations of the atmospheric models to the ODP data of the above eleven satellites.

Table 3: Model correlation coefficients

Sat. No.	Name	k (days)	Lag (k -days)	MET	MSIS	J71	J77
60	Explorer 8	0.75	3	0.55	0.62	0.58	0.50
614	HitchHiker 1	0.84	3	0.82	0.86	0.88	0.81
1616	Atlas D RB	0.79	3	0.72	0.74	0.80	0.74
2389	OV3-3	0.85	3	0.75	0.74	0.83	0.78
2404*	OV3-3 RB	0.74	3	0.74	0.77	0.77	0.74
3342	Explorer 39 Debris	2.21	1	0.73	0.68	0.71	0.79
4222	Scout B RB	0.69	3	0.84	0.86	0.87	0.83
8368	DELTA 1 RB(2)	0.66	3	0.62	0.63	0.75	0.64
11791	Atlas F RB	1.87	2	0.92	0.88	0.93	0.85
12069	Atlas Centaur RB	1.58	2	0.71	0.67	0.82	0.72
15679*	Ariane 3 RB(3)	2.11	2	0.74	0.79	0.72	0.57

* Correlation timespan was limited to DOY = 1-250, due to orbital decay.

* Correlation timespan was limited to DOY = 1-200, due to orbital decay.

The results reveal that the J71 model performed the best out of the 4 models as indicated by the correlation of J71 being the highest for 7 of the 11 satellites. This suggests that J71 is the better atmospheric model for the altitude range studied. In general, it can be seen from the correlations that all the models performed well for nearly all of the objects, having correlation coefficients from 0.7 to 0.9. The only exception is Explorer 8, where the correlations are in the range of 0.5 to 0.6. There is a myriad of reasons why the models didn't fit this satellite as well as the others. Examining a plot of the correlation of MET density to ODP of Explorer 8 in Figure 19 reveals that the lag

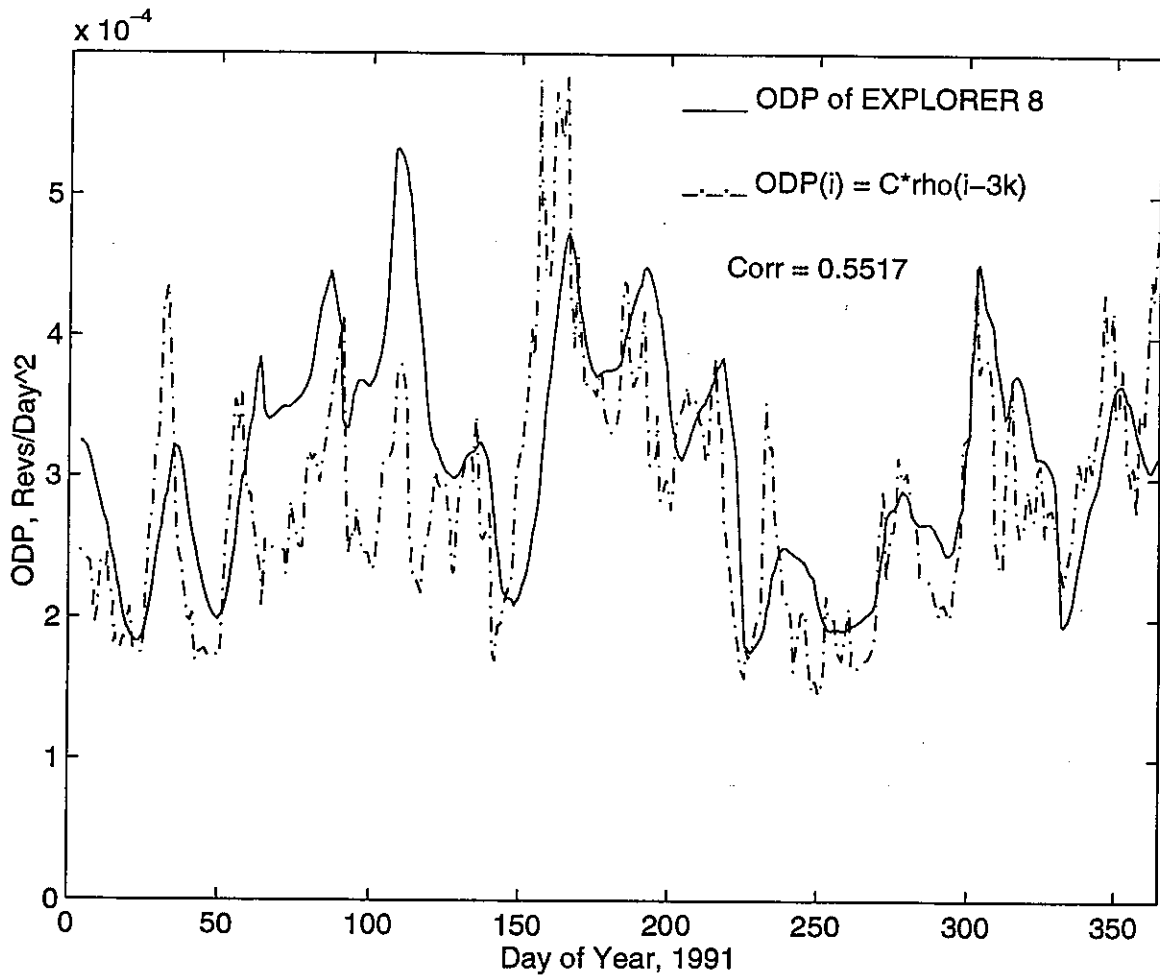


Figure 19: Correlation of MET to Explorer 8 using phase shifts of 3k-days.

between the ODP data and the density model still exists and is more than likely the reason for the low correlation. The presence of a lag even after shifting the density $3k$ -days, where k for Explorer 8 is 0.75, suggests that the data fit-span used in calculating the ODP of Explorer 8 is longer than $6k$ -days, *i.e.*, 6×0.75 , or approximately 4.5 days. Investigating further, the density was shifted out to a total of $10k$ -days. Figure 20 shows a plot of the results of shifting the density $8k$ -days.

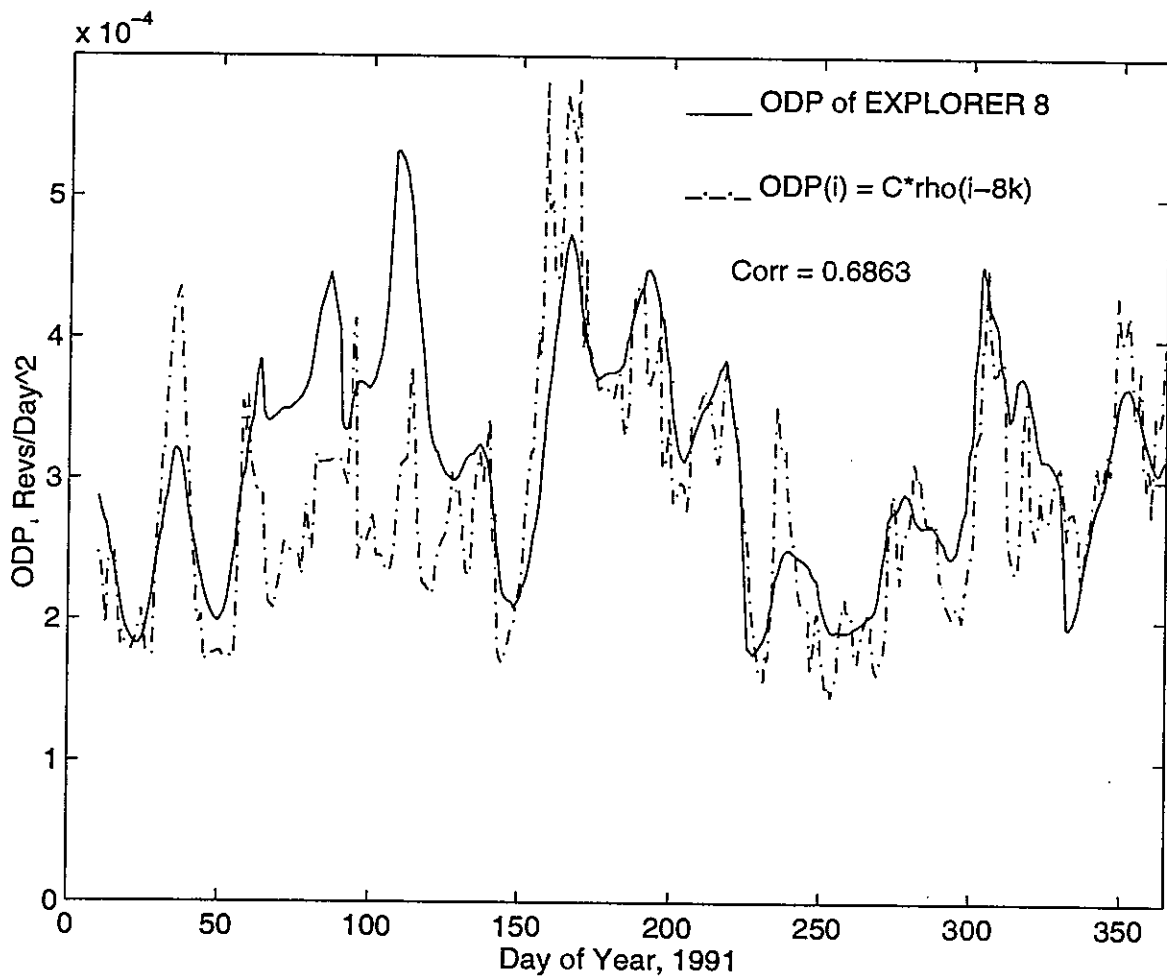


Figure 20: Correlation of MET to Explorer 8 using phase shifts of $8k$ -days.

As in previous plots, the solid line represents actual ODP, whereas the dash-dot indicates the ODP estimated by the MET model. By shifting the density, the lag between the averaged ODP solution from DC and the atmospheric model has been eliminated. The end result is an increase of 25% in the model correlation from a value of 0.55 up to 0.69. Figure 20 shows the lag versus correlation for Explorer 8.

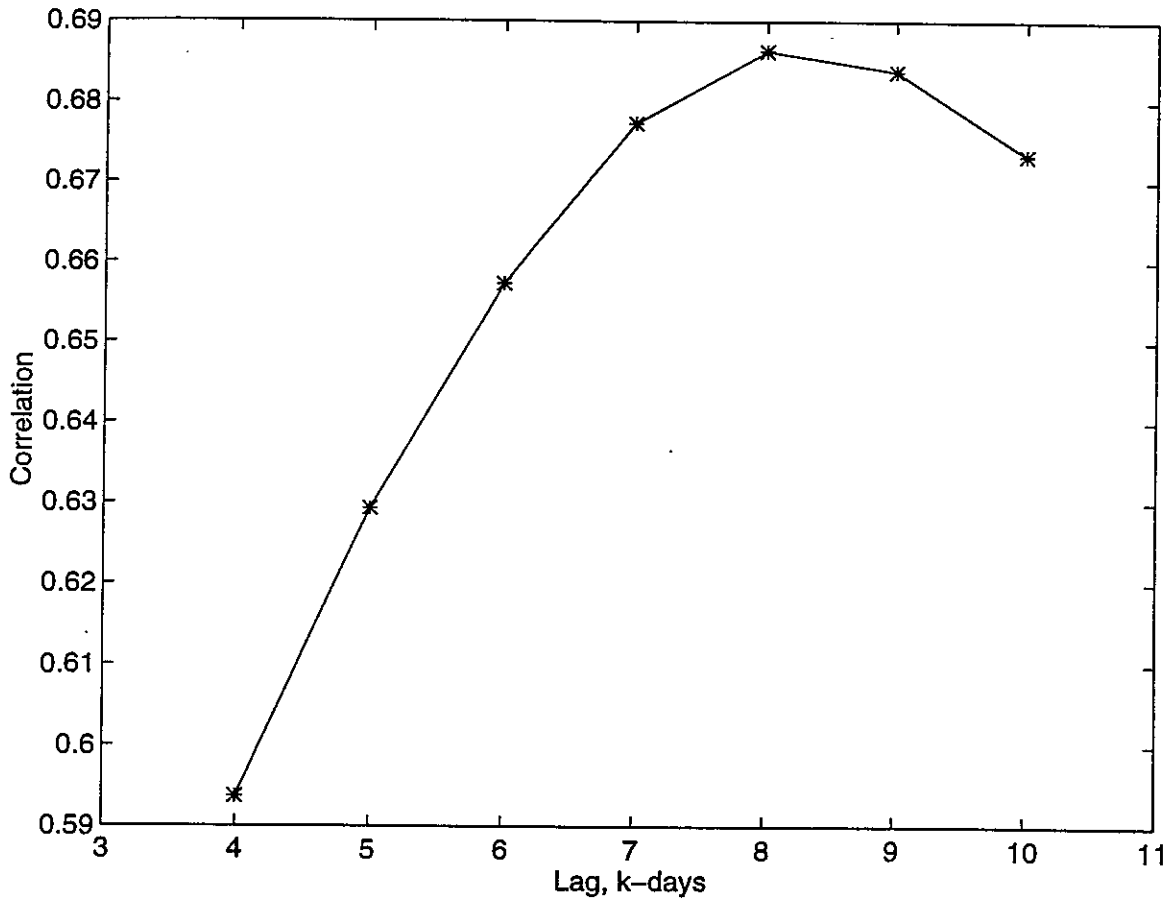


Figure 21: Effect of lag on Explorer 8 correlation

It appears that the optimum lag falls between 8 to 9k-days, which is equivalent to 8.5×0.75 , or a lag of 6.4 days. Recall that the timestamp from the DC process occurs at the time of the last observation so that the lag will be approximately $\frac{1}{2}$ of the fit-span.

Therefore, a lag of 6.4 days would suggest a fit-span of about 13 days. Explorer 8 has been orbiting for over 35 years due most likely to its relatively high height of perigee and small RCS, which translates into lower drag. Hence the orbit of Explorer 8 is decaying very slowly. A slowly decaying orbit does not require frequent DC of elements as would be required for a rapidly decaying orbit. Therefore, observations of a slowly decaying orbit such as Explorer 8, can be extended over many days for a longer fit-span, and thus, lower the computational burden associated with performing frequent DC updates.

Another satellite of interest is the Atlas F rocket body (RB). Correlations for this satellite ranged from 0.85 to 0.93. To get a better understanding as to why the

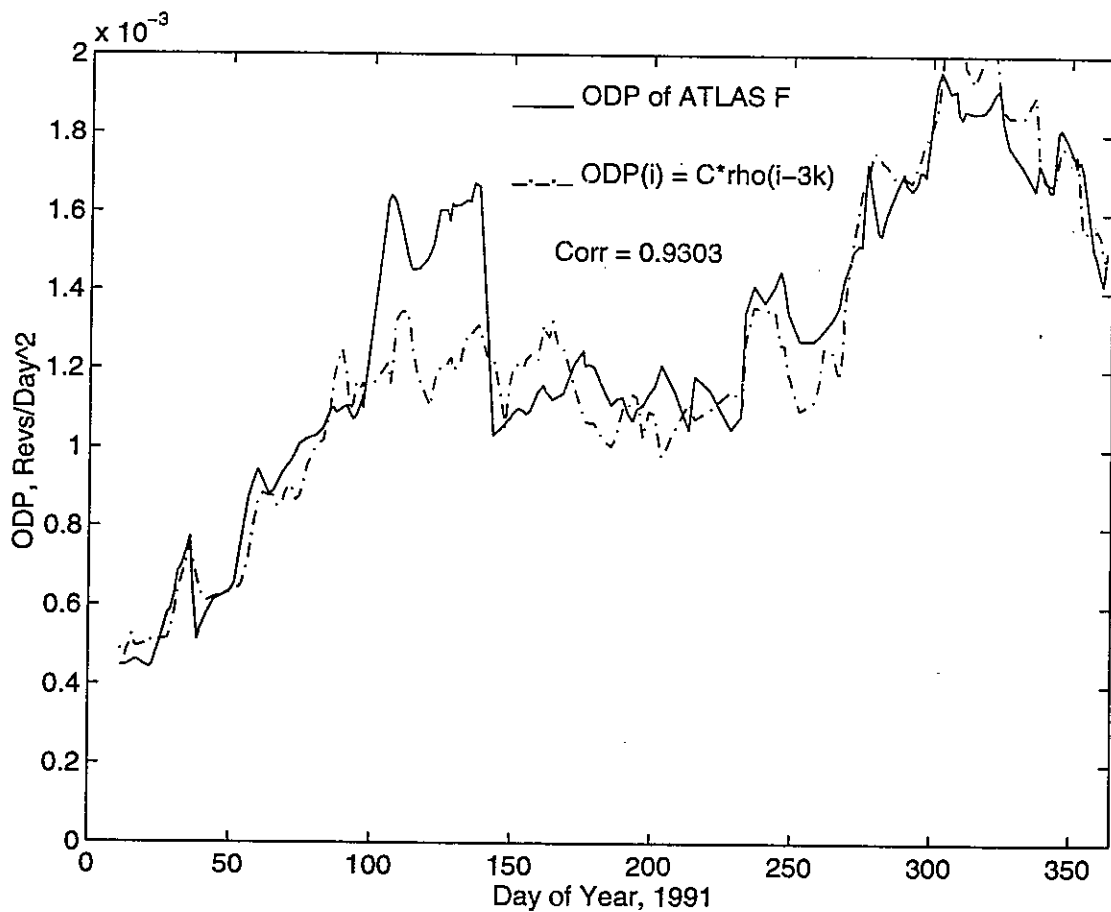


Figure 22: Correlation of J71 to Atlas F using phase shifts of 3k-days.

correlation was significantly higher than the other satellites, a plot of the LS fit of J71 to the ODP of Atlas F was examined as shown in Figure 22. The plot shows that the ODP of Atlas F has a large long-term linear trend superimposed upon finer short-term variations caused most likely by changes in atmospheric density resulting from fluctuations in solar flux and geomagnetic activity. The linear trend in ODP for Atlas F is most likely due to the 40 km decrease in the height of perigee. Large decreases in altitude equate to increases in density and ODP. When the change in altitude becomes large enough, *i.e.* approaching the value for the density scale height, H , ODP becomes a function dominated by altitude changes rather than by variations in solar and geomagnetic inputs, which appears to be the case for Atlas F. All of the models were able to match this large linear tendency in ODP, which accounts for the high correlation. However, it is more critical that the models match the finer details of the ODP curve, which would indicate that the models are following the physical short-term trends occurring in the atmosphere. For this reason, the high correlation given by the models for Atlas F should be viewed with caution. Ideally, the large linear trend should be removed before analyzing the performances of the models. This can be accomplished by passing the ODP of Atlas F through a high pass filter. A high pass filter removes low frequency content from the input signal while allowing the high frequency signal to pass through unaltered.⁴⁵

As mentioned earlier under satellite selection criteria, it is desirable to study atmospheric drag effects using satellites in fairly eccentric orbits, where the drag effect would occur primarily near perigee, as opposed to a circular or nearly circular orbit where the altitude of the satellite would be nearly the same throughout the orbit, and thus latitudinal, seasonal, and LST variation of drag and density could not be isolated. It should be expected that for the

circular orbit case, ODP would not be a strong function of H, since altitude is nearly fixed. However, for eccentric orbits, altitude varies and therefore variation in H should have a stronger effect on ODP.

Recall the relationship expressed in (5) where satellite ODP, or \dot{n} , was proportional to $\rho H^{\frac{1}{2}}$ for orbits with eccentricities of 0.2 and larger, and therefore could be used to estimate the ODP of a satellite using densities predicted by an atmospheric model. Of the eleven satellites examined, a number of them were in orbits of eccentricity greater than 0.2, and given this relationship, there should be an improvement in model correlation if the expression $\rho H^{\frac{1}{2}}$ is related to ODP instead of simply ρ . To investigate, $\rho H^{\frac{1}{2}}$ was calculated for all the satellites and correlations performed to their respective ODP values. Table 4 shows the percent change in correlation for the MET model using $\rho H^{\frac{1}{2}}$ relative to the correlations and phase lags given previously in Table 3.

Table 4: Change in correlation after fitting $\rho H^{\frac{1}{2}}$ to ODP

Sat. No.	Name	Change in Corr. (%)	Eccentricity
60	Explorer 8	-1.60	0.075
614	HitchHiker 1	-0.60	0.150
1616	Atlas D RB	+0.14	0.150
2389	OV3-3	+0.40	0.180
2404	OV3-3 RB	+4.44	0.060
3342	Explorer 39 Debris	-0.40	0.073
4222	Scout B RB	+0.24	0.085
8368	DELTA 1 RB(2)	+8.80	0.330
11791	Atlas F RB	+0.55	0.470
12069	Atlas Centaur RB	+3.94	0.400
15679	Ariane 3 RB(3)	+2.17	0.690

As was suspected, correlations increased for those satellites in orbits with eccentricities larger than 0.2. For most of the satellites with $e < 0.2$, the correlation coefficients went up only slightly or in some cases decreased. There were exceptions however, notably the OV3 3rd stage RB, where the orbit was fairly circular yet the correlation increased. This was most likely due to decay of the OV3 orbit, causing perigee altitude to decrease into a denser atmosphere where H changes more rapidly and therefore strengthening the dependency of ODP on H.

Ballistic Coefficient Estimation

Ballistic coefficients were estimated using predicted densities at perigee in conjunction with the appropriate theoretical orbital decay equation (1), (4), or (5) from Chapter 2.⁴⁶ The empirical ballistic coefficient of a given satellite was obtained by equating the theoretical ODP expression to actual ODP values, and solving for β . A theoretical β was then calculated if possible, based on available satellite physical characteristics, *i.e.*, shape, size, and mass. Because the cross-sectional area perpendicular to the velocity direction of non-spherical satellites can vary throughout an orbit, as is the case for a tumbling satellite, minimum, maximum, and mean areas were calculated, and the results used to estimate the possible ranges in satellite β 's.⁴⁷

The results of estimating ballistic coefficients for all the satellites are shown in Figure 23, where the circles represent β as estimated by MET, and the asterisks are a mean β as calculated from satellite physical characteristics published by King-Hele.²⁹ Error-bars appear depicting the possible range in β based on maximum and minimum satellite reference areas if known, for the non-spherical satellites.

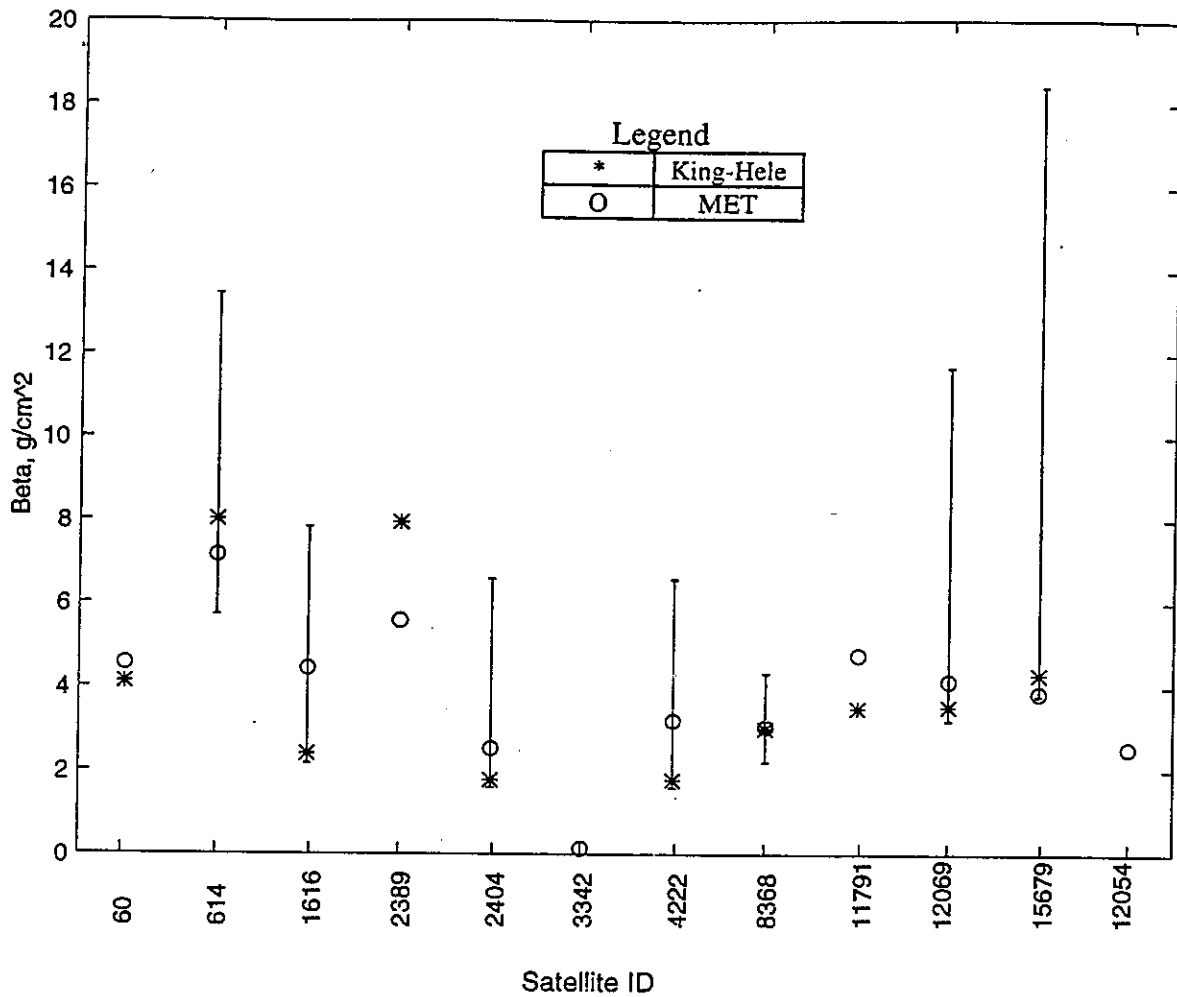


Figure 23: Ballistic coefficient plot.

The plot shows the results for the satellites from the extended satellite study and Cosmos 1220, and reveals the good agreement between the empirical and theoretical estimates for β . Notice that for satellite 3342, also known as Explorer 39 debris, β is extremely small. No physical characteristics for Explorer 39 debris are available, therefore a theoretical β could not be calculated.

In summary, the atmospheric models correlated fairly well to satellite ODP data, with the J71 model performing the best. By applying the LS fitting process between model densities and satellite ODP values, two simple linear ODP models were developed that could be used to predict satellite orbital decay rates. The first form where ODP was estimated by a LS fit to density, would be used for quasi-stable orbits with $e < 0.2$, whereas in the second form, ODP was fit to $\rho H^{\frac{1}{2}}$. This version would be reserved for orbits with $e \geq 0.2$ and for satellites that are experiencing high rates of orbital decay prior to re-entry. In the latter case, the density scale height, H , would be more likely to change significantly enough to effect satellite orbital decay rates and hence must be accounted for in the ODP model. In addition, it was determined that a phase lag exists between satellite ODP values as determined by DC, and atmospheric disturbances. The amount of lag depends on the fit-span that is used to perform the DC. How well the atmospheric models predicted ODP fluctuations brought on by solar disturbances determined the level of correlation. Although the models generally represented the atmospheric dynamics well, there were occasional instances where all the models underestimated effects of geomagnetic and solar activity, clearly indicating the need for further advancement in atmospheric modeling. By using the above ODP models and eliminating the lag, improved fence crossing predictions could be made, potentially reducing the number of UCT's. In addition, atmospheric models can be used in conjunction with orbital decay theory to determine satellite ballistic coefficients, which can aid in identifying satellite class or be used to monitor changes in β that might occur due to alterations in the orientation of the satellite to the orbit-plane, or changes in the mass-to-area ratio due to maneuvers or

collisions, *etc.* The empirical ballistic coefficients of the majority of satellites agreed well compared to their theoretical values.

6. One-State Kalman Filtering Approach

Recall from Chapter 4 that ODP from element set data is the orbital decay parameter calculated from a DC process of variable data length. This makes the ODP smooth and lag the physical processes occurring in the atmosphere. Using smoothed ODP data with a lag to make fence crossing predictions can lead to large crossing errors during severe geomagnetic storms such as the one that occurred in March of 1989, when crossing errors grew to over 10 seconds for certain satellites. To circumvent this, a process must be developed that would provide a more responsive ODP with little or no lag.

The purpose of this chapter is to determine the feasibility of using a one-state discrete Kalman filter to process observations, *i.e.*, take in measurements as they occur at the fence and make optimal corrections to ODP, *i.e.*, the state, as required to reduce the number of UCT's occurring during large solar storms. Kalman filtering had been applied previously for the same purpose, but a three-state filter had been utilized.⁴⁸

A one-state filter was chosen because the recursive filter equations listed in Chapter 2 are reduced from vectors and matrices to simpler scalar expressions. The result is a filter that is easier to implement and maintain and therefore more readily applied to a large-scale operation such as maintaining a satellite catalog, as opposed to using a multiple state filter. However, the disadvantage of modeling the physical world by a single state variable is that the model will be more likely to be deficient in representing real world dynamics. Thus the more state variables there are describing state dynamics, the more accurate the model will be, but at the price of adding more complexity to the operation.⁴⁸

State Model

The single state variable that was chosen for filtering was ODP, *i.e.*, \dot{n} , making the state “vector”:

$$\mathbf{x} = [\text{ODP}] \quad (23)$$

Normally as part of the Kalman filter process, state dynamics are handled by the STM ϕ , where dependencies among state variables are expressed using partial derivatives. As stated previously, ODP affects both ℓ and n as seen in equations (50) and (51). Since ODP is the only state variable, the state transition matrix (STM) will simply be unity. This means that changes in ℓ and n due to changes in \dot{n} can not be reflected by applying the STM to the state. To circumvent this, changes in n and ℓ due to variation in the state variable can be reflected by repropagating n and ℓ in time, once the new estimate for \dot{n} or ODP is determined.

State Noise Model

State noise is a measure of the uncertainty in the physical variable being modeled. In this application, state noise would be the residual variations in ODP as indicated by the existence of fence-crossing errors. If the current value of ODP is predicting crossing times with zero error, then there would be no uncertainty in the knowledge of the state and hence state noise would be zero. However, this is rarely the case since ODP is constantly changing primarily due to atmospheric drag for LEO satellites.

Modeling the state noise associated with a dynamic atmosphere can be a challenging task. Recall earlier the strong perturbations to atmospheric density and hence

ODP that are caused by fluctuations in both the solar flux, $F_{10.7}$, and geomagnetic index, A_p . Given the dynamic nature of the atmosphere, it can be expected that the noise levels of the atmosphere are highly dependent on the values of $F_{10.7}$ and A_p . Thus it can be expected that state noise levels will be quite different for quiet atmospheric conditions where $F_{10.7} < 100$ and $A_p < 50$, as opposed to “noisy” periods during severe solar storms where $F_{10.7} > 200$ and/or $A_p > 100$. This suggests that a representative state noise model must be able to adapt to the changing conditions of the atmosphere, in contrast to a state noise model that uses a fixed noise level based on the average value of ODP in the past.

To investigate which type of process noise model would work best, both models were evaluated using real fence data for the satellites listed in Table 5. First, the fixed noise model used was of the form

$$\mathbf{Q}_k = [\gamma dt]^2 \quad (24)$$

where dt is the time between observations in days and γ is some constant to be determined. Second, the adaptive noise model used was of the form

$$\mathbf{Q}_k = [\alpha \text{ODP}_{k-1} dt]^2 \quad (25)$$

where αODP_{k-1} is a percentage of the previous state estimate ODP_{k-1} and is used to represent the current level of state noise. In addition, \mathbf{Q}_k in both expressions is proportional to dt^2 . Thus the state noise increases with the time between fence

observations, due to the higher uncertainty in older estimates of ODP representing the current rate of the orbital decay of a satellite.

Using ODP directly in the state noise expression allows the state noise model to be adaptive to the dynamics of the atmosphere. That is, if a perturbation of some sort occurs in the atmosphere, it will manifest itself in the estimated value of ODP output from the Kalman filter. This in turn will affect the state noise level, increasing noise for perturbed periods whereas decreasing it for quiet intervals. However, there is the possibility that measurement errors exist, *e.g.*, associating a fence-crossing observation with the incorrect satellite, errors in data transmission can occur, *etc.* If the low quality of the measurement, *e.g.*, at time t_k , was not indicated by a corresponding rise in the measurement noise \mathbf{R}_k , and the error covariance \mathbf{P}_{k-1} has converged, the Kalman filter will react to the noisy measurement by adjusting the state estimate of ODP to eliminate the residual crossing error and result in an erroneous estimate of ODP. The bad estimate of ODP would then cause the state noise to be over or under-estimated depending on whether ODP was estimated high or low. In the case of an under-estimated ODP, this would lower the state noise \mathbf{Q}_k , which in turn would lower the Kalman gain. When the gain becomes small while the measurement still contains useful information, *i.e.*, the crossing time of a satellite is changing due to an actual change in ODP, the filter is no longer functioning correctly and is said to diverge. Ultimately the filter should use the information contained in the measurement to correct the state, but when filter divergence occurs, the error covariance \mathbf{P}_k becomes small, indicating low uncertainty in the state, *i.e.*, the current state is correct and the measurement erroneous. Thus, the new estimate of the state is not updated

properly to reflect the changes in ODP. In the case that ODP is over-estimated, having ODP in the state noise expression will drive Q_k up and consequently both P_k and the Kalman gain will increase. A filter with an artificially large gain is said to be reactive, with a high level of uncertainty in the state, *i.e.*, the current state estimate is erroneous and the measurement correct, and therefore the filter reacts and corrects the state without accounting for measurement noise.⁴⁹

Using a weighted averaging technique on ODP such as

$$\overline{ODP}_k = \frac{(3ODP_{k-1} + 2ODP_{k-2} + ODP_{k-3})}{6} \quad (26)$$

where \overline{ODP}_k represents the weighted average at time k , and ODP_{k-1} , ODP_{k-2} , *etc.*, the estimated values for ODP at times $k-1$, $k-2$, *etc.*, could reduce the lack of robustness or susceptibility to bad data. The use of a weighted ODP average in the state noise expression (25) would help prevent a single spurious estimate of ODP from making a large change to the state noise. On the contrary, if there were a real change in atmospheric density, ODP would tend to increase or decrease over consecutive measurements, which would shift the weighted average of ODP in a similar fashion.

Measurement Noise Model

To limit the number of variables that would need adjusting for filter “tuning” purposes, the measurement noise level was fixed, based on the typical variance of fence

observations, and the ratio of the process noise to the measurement noise, Q_k/R_k , changed. The ratio Q_k/R_k is essentially the signal to noise ratio of the state variable with respect to the measurement, and is often used to tune a Kalman filter.⁵⁰

Accountability of anomalous measurements is essential for successful Kalman filtering in a real environment, and ideally, bad data should be prevented from entering the filter in the first place. One method that could be used involves checking the “innovations” vector, $[z - H\hat{x}]$, for sudden jumps in amplitude or rate before a bad data point enters the filter.⁵¹

Process Flow

The flowchart in Figure 24 depicts the Kalman filter process flow as applied to radar fence data.

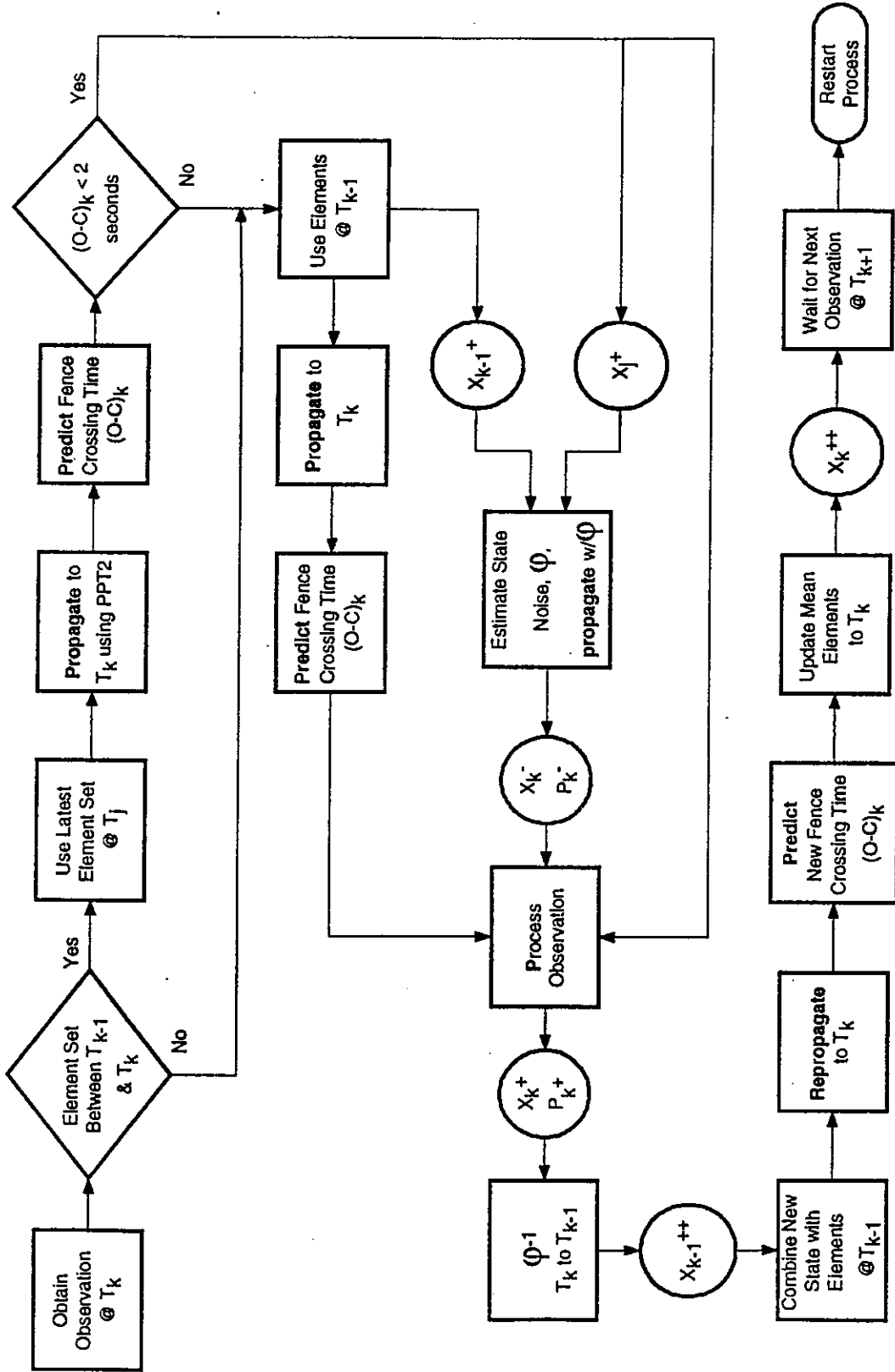


Figure 24: Kalman filter process flow diagram

The process begins in the upper left corner when an observation is obtained at some time T_k . If mean orbital elements are available at some time T_j between time T_k and the previous observation T_{k-1} , they are propagated in time to T_k , otherwise the value of the mean elements at time T_{k-1} are propagated to time T_k . A fence-crossing time prediction is then made using the software PPT2. Next, the residual crossing error is computed $(O - C)_k$. If the starting elements came from the DC process, the value of the residual is checked. If the crossing error is greater than ± 2 seconds, the elements are discarded and the value of the mean elements at T_{k-1} and $\hat{\mathbf{x}}_{k-1}$ are propagated to T_k and a new prediction is calculated. If the crossing error is less than ± 2 seconds, the DC elements and associated state, $\hat{\mathbf{x}}_j$, are kept. Subsequently, the state noise \mathbf{Q}_k is estimated using (24) or (25). The *a priori* information $\hat{\mathbf{x}}_k^-$ and \mathbf{P}_k^- is obtained by using $\Phi_{k-1,k}$ to propagate the state from $\hat{\mathbf{x}}_{k-1}^+$ to $\hat{\mathbf{x}}_k^-$ using (16) and the error covariance from \mathbf{P}_{k-1}^+ to \mathbf{P}_k^- using (17). The observation is then "processed" whereby the Kalman gain is calculated using (14) and both the state estimate $\hat{\mathbf{x}}_k^+$ and error covariance \mathbf{P}_k^+ are updated using (13) and (15) respectfully. The value $\hat{\mathbf{x}}_k^+$ output from the filter is **the value of $\dot{\mathbf{n}}$ that should have been applied during the period from T_{k-1} to T_k to reduce the fence crossing error.** The effects of $\dot{\mathbf{n}}$ on the other elements, primarily ℓ and n , must be accounted for by replacing the value of $\dot{\mathbf{n}}$ or the state at T_{k-1} with the new estimate $\hat{\mathbf{x}}_k^+$ and repropagating the elements to time T_k . Updating the mean elements to T_k concludes the recursive process until the satellite being tracked is observed again.

Objects Selected

The Kalman filter process was evaluated using the three satellites listed in Table 5, which provides orbit and physical characteristics of the satellites.

Table 5: Characteristics for additional satellites

Sat. No.	Int. No.	Name	Ha x Hp (km)	<i>i</i> (deg.)	RCS (m ²)	Shape	Size (m)	Mass (kg)
11848	1980-051A	Meteor 1 (30 th)	472 x 439	74	7.6	Cyl. + 2 vanes	5.0 L ? x 1.5 Dia. ?	2200
15326	1984-104A	Cosmos 1601	458 x 436	65.8	14.8	Cyl.	4.0 L ? x 2.0 Dia. ?	?
16928	1986-067A	Cosmos 1776	589 x 534	97.7	28.1	Oct. Ellipsoid	1.8 L ? x 1.5 Dia. ?	?

The satellites were chosen based on the availability of radar fence observations and the level of residual crossing error.

Satellite Residual Errors Prior to Filtering

To determine if Kalman filtering can reduce the number of UCT's, fence-crossing predictions were made for the three satellites during the first half of 1989

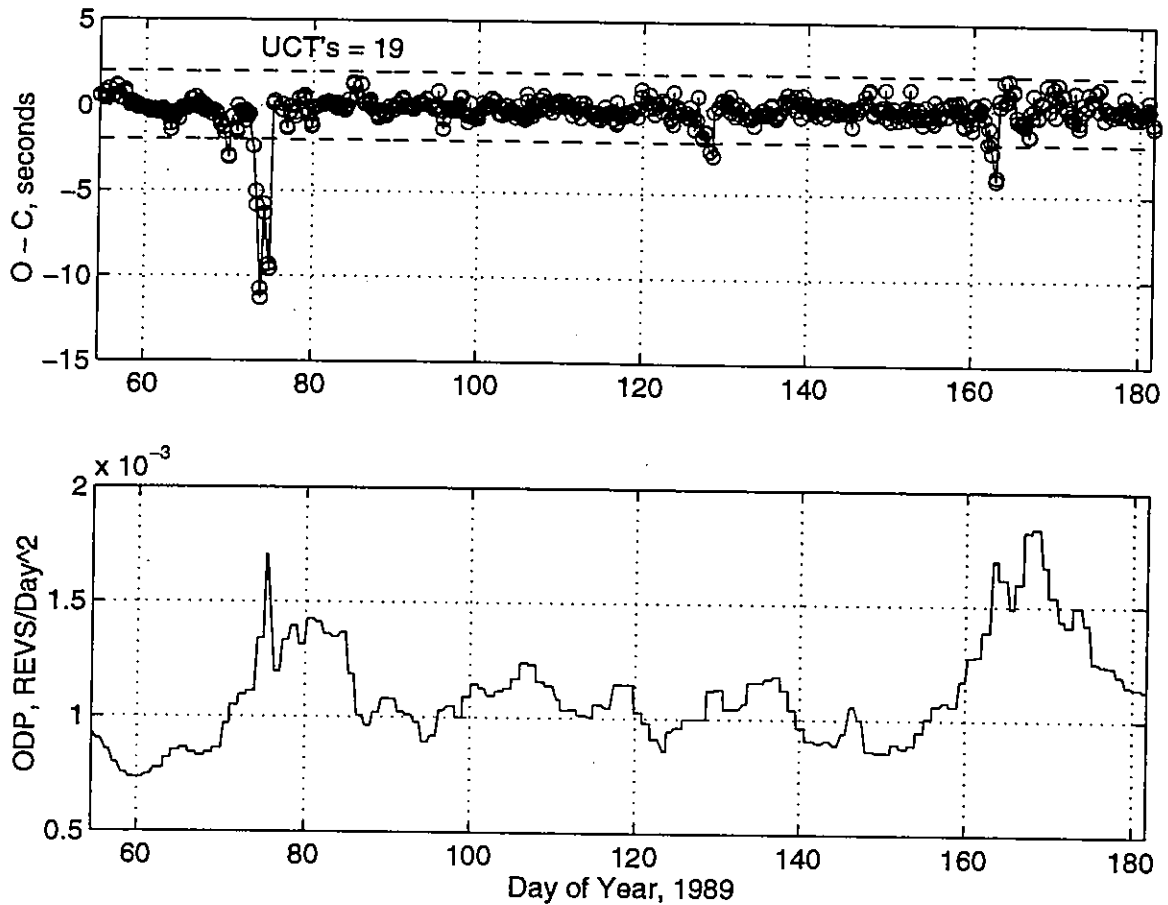


Figure 25: Residual crossing errors and ODP for Cosmos 1601 without filtering.

without filtering. The top plot Figure 25 shows the residual crossing errors over time for Cosmos 1601 whereas the bottom plot is the corresponding values of ODP as calculated from DC of elements. As can be seen by examining the (O - C) plot, there are primarily 3 periods when the crossing errors fall outside ± 2 seconds for Cosmos 1601. The first of which corresponds to the large geomagnetic storm that occurred in March of 1989 when the geomagnetic index A_p reached a value of 249, and where the crossing errors reached a maximum of nearly 12 seconds. Figure 26 shows a similar plot for Cosmos 1776.

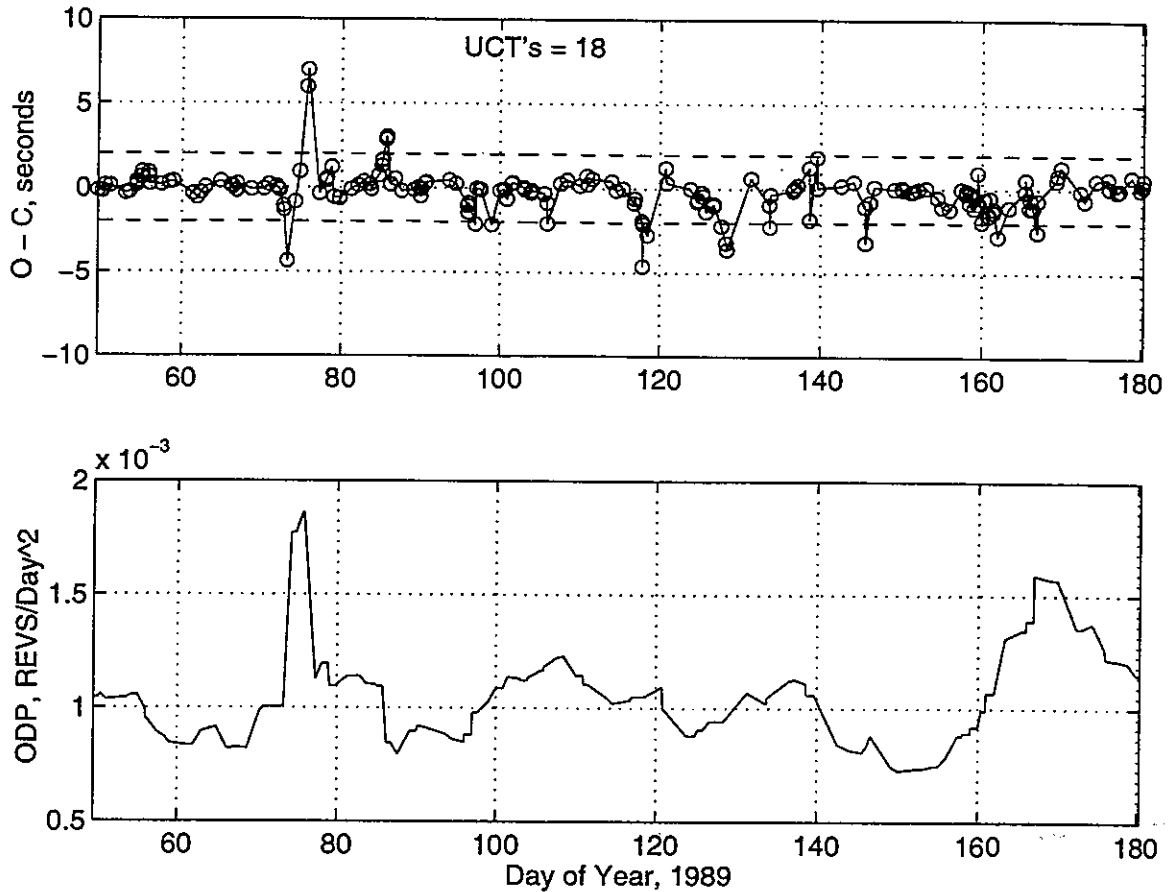


Figure 26: Residual crossing errors and ODP for Cosmos 1776 without filtering.

As before, the main disturbance occurred during March of 1989 along with several other periods where the satellite residual crossing errors fell outside the identification window limit of ± 2 seconds. Notice that the ODP values were over-corrected during the geomagnetic storm on DOY 72, meaning that the ODP values derived from the DC solution were too large and caused fence crossing prediction times to be too early, and resulted in positive fence-crossing residuals outside the 2-second identification window.

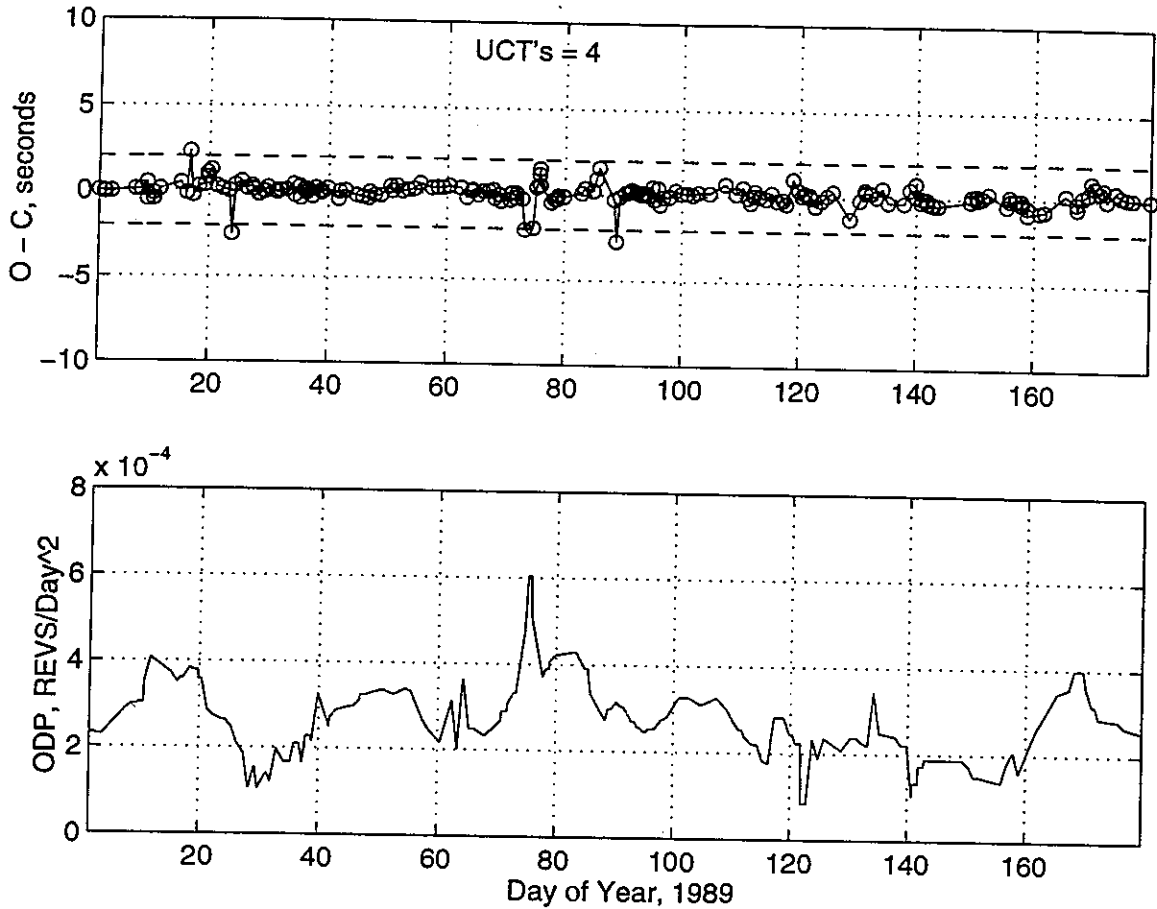


Figure 27: Residual crossing errors and ODP for Meteor 1 without filtering.

The top plot of Figure 27 shows the residual crossing errors for Meteor 1. This satellite has only a few UCT's suggesting that atmospheric drag was never large enough to seriously change the mean motion of Meteor 1 during the period of study. After examining the lower plot of ODP for Meteor 1, it can be seen that the average magnitude of ODP for the period was approximately 3×10^{-4} revs/day² which is less than half of the nominal value recorded for the other two satellites. Referring back to Table 5, which lists RCS values and other characteristics for the three satellites, the RCS value for Meteor 1 is 7.6 m^2 , which is considerably smaller than the other two satellites. A lower RCS value

generally means lower surface area, which would tend to raise the ballistic coefficient of a satellite notwithstanding differences in mass. A higher β would lower the effect density and drag would have on orbital motion, which appears to be the case given the few number of UCT's for Meteor 1.

Filtering Results

Having established the residual crossing errors for the three satellites without recursive filtering, a direct comparison can now be made of the impact of filtering ODP during normal fence operations. A parametric study was performed using a wide range of state noise levels for each of the two different formulations of Q_k as delineated in equation (24) and (25). Figure 28 shows the effect of filtering the ODP of Cosmos 1601 using the state noise expression described in (25), where 20 percent of the previous estimate, ODP_{k-1} , was used as an indication of the current state noise level of the atmosphere.

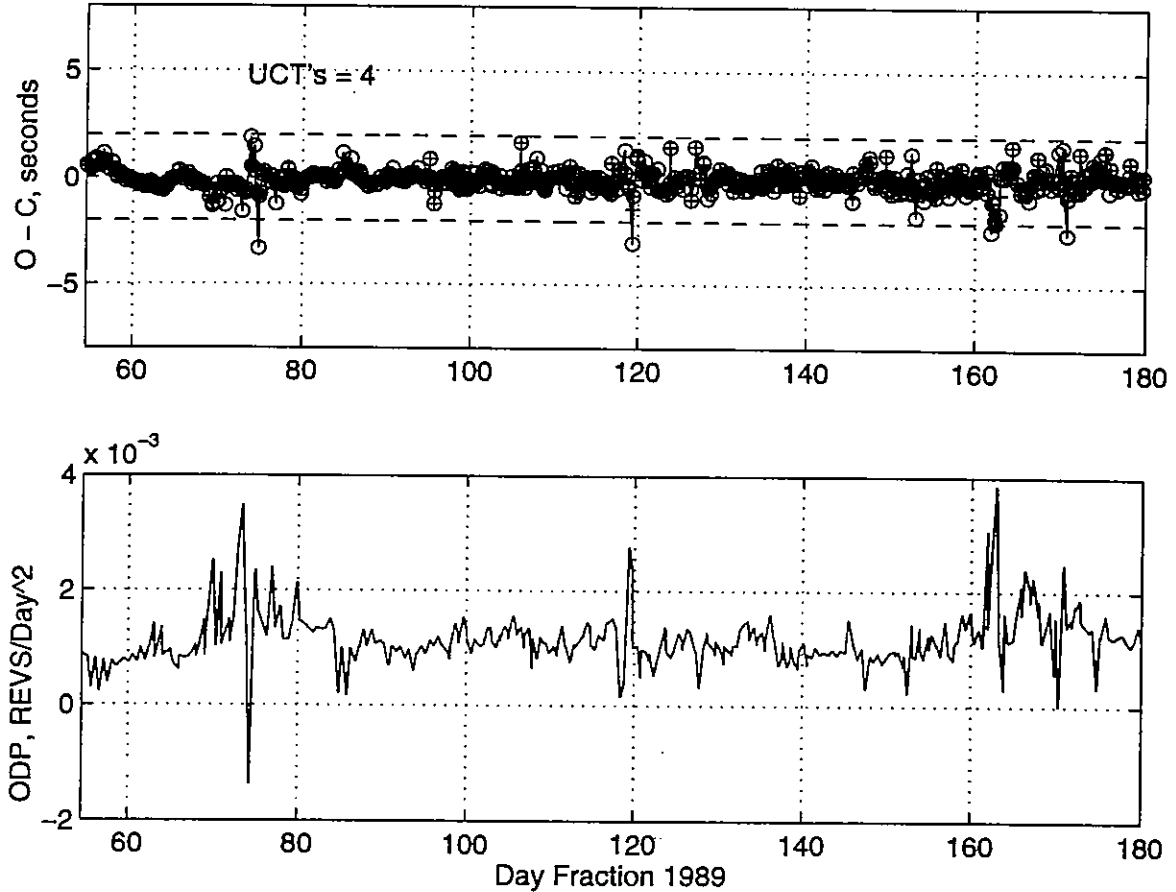


Figure 28: Effect of a one-state Kalman filter on Cosmos 1601 fence-crossing errors.

The top plot demonstrates that the filter dramatically reduces the number of UCT's with only a few points falling outside the +/- 2-second identification window. The bottom plot displays the values of ODP estimated by the Kalman filter for Cosmos 1601. Notice that after the geomagnetic storm on DOY 72, the filter estimate of ODP went negative, prior to recovering to a nominal value. Negative values of ODP are uncommon and could be due to a satellite undergoing maneuvers. In this case, the negative ODP is due to the filter over-correcting the state, meaning that too large a value for ODP was estimated during

the storm. When the geomagnetic disturbance subsided, ODP had to be reduced greatly to keep the fence-crossing errors to a minimum. Such wide changes to the state are necessary at both the onset and conclusion of solar storms. During these periods the filter state noise must increase for the filter to have a fast transient response to the storm, enabling sharp corrections to ODP, but at the cost of adding more noise to the ODP estimate.⁵² Because the Kalman filter is single state, fence-crossing errors are essentially a function of ODP only, and therefore all the uncertainty is placed in ODP, rather than being distributed across additional state variables such as n and ℓ . In actuality, some of the fence-crossing residuals are due to errors in n and ℓ , and therefore a single state filter is susceptible to over-correction during severe solar storms.

A number of trials were run using different levels of state noise for both the adaptive and non-adaptive state noise expressions for all three satellites. Table 6 and Table 7 summarizes the results.

Table 6: Filter results for an adaptive state noise.

Satellite		No Filter	α			
			0.05	0.10	0.20	0.40
Cosmos 1601	UCT's	19	16	10	4	9
	RMS	1.26	0.83	0.67	0.55	0.65
Cosmos 1776	UCT's	18	11	9	10	12
	RMS	1.27	0.98	0.89	0.87	1.17
Meteor 1	UCT's	4	3	3	6	6
	RMS	0.53	0.52	0.52	0.55	0.62

Table 6 shows the results of Kalman filtering on the number of UCT's and on the root mean square (RMS) of the residual crossing error, using the adaptive state noise equation (25), with different values of α . The largest reduction in both UCT's and RMS of the crossing error is shown by Cosmos 1601, followed by Cosmos 1776. Meteor 1 shows only a slight improvement over the no filter case.

Table 7: Filter results for a non-adaptive state noise.

Satellite		No Filter	γ			
			1.00E-05	1.00E-04	2.00E-04	4.00E-04
Cosmos 1601	UCT's	19	16	6	6	12
	RMS	1.26	1.16	0.59	0.59	0.76
Cosmos 1776	UCT's	18	12	9	10	13
	RMS	1.27	1.08	0.90	1.20	1.27
Meteor 1	UCT's	4	3	6	5	4
	RMS	0.53	0.52	0.94	1.10	0.53

Table 7 shows the results of Kalman filtering using the non-adaptive state noise equation (24) with different values of γ . In this case, the filter is able to achieve the same reduction in UCT's and RMS of crossing error as in the adaptive state noise case, with the exception of Cosmos 1601, where the adaptive state noise expression lowered the number of UCT's and RMS of crossing error further.

These results suggest that the Kalman filter performs just as well using either the adaptive or non-adaptive state noise expressions for satellites with medium to low residual crossing errors. However, for satellites with large crossing errors, filtering using an

adaptive state noise appears to have greater success at lowering UCT's and tightening the RMS of crossing errors. By having ODP in the state noise expression, Q_k can increase during periods of severe solar storms, enabling the filter to make the larger, sharper corrections needed to ODP during such noisy periods, whereas during quiet atmospheric intervals, ODP will be smaller, making Q_k contract, which will tend to make the state corrections smoother and less likely over-compensated due to noisy measurements. However, the non-adaptive Q_k does not have the capability to expand or contract based on atmospheric conditions, and therefore the filter is more likely to have difficulty making transitions from noisy to quiet atmospheric conditions for satellites that are sensitive to large changes in density and drag such as Cosmos 1601.

7. Conclusions and Recommendations

These findings support the potential for estimating the orbital decay rate of satellites using an orbital decay parameter (ODP) model developed from fitting predicted density to actual ODP values in a least squares (LS) sense. For satellites in high eccentric orbits *i.e.*, $e > 0.2$, or for satellites undergoing high decay rates, improvements can be made in the ODP model by basing orbital decay estimates on the LS fit of $\rho H^{\frac{1}{2}}$ to satellite ODP rather than just density. Predicted ODP could then be used to calculate fence-crossing times and potentially reduce the number of uncorrelated targets (UCT's) occurring at the radar fence. Such a system would be dependent on reasonable solar and geomagnetic predictions in order for atmospheric density to be properly estimated. Given these constraints though, estimating orbital decay rates using an ODP model would eliminate the phase lag that currently exists between the ODP calculated from DC and changes in atmospheric density. This would prove to be critical during severe solar storms when up-to-date ODP values are necessary to successfully predict crossing-times and maintain the satellite catalog.

Atmospheric Modeling

Of the four atmospheric models compared, the Jacchia '71 (J71) model performed the best as measured by the correlation between the density predicted by the atmospheric model and the actual ODP calculated from fence observations. Specifically, out of a dozen satellites examined, J71 showed the highest correlation for seven. The major factors behind the results were due to differences in how well each model estimated density fluctuations

due to variations in daily solar flux and geomagnetic activity. There was one particular geomagnetic storm that was greatly under-estimated by all four models, clearly indicating the need for better modeling of the upper atmosphere.

The ballistic coefficients of the satellites examined were determined using orbital decay theory in conjunction with density estimated from an atmospheric model. Results indicated good agreement with theoretical values. Having the ability to determine β can help in identifying an unknown satellite or in detecting changes in mass or frontal area due to collisions or maneuvers.

Kalman Filtering

The use of a single state Kalman filter offers a potential improvement in maintaining the catalog of artificial satellites during large solar storms by reducing the number of UCT's occurring and tightening residual RMS crossing errors. LEO satellites with large surface-to-mass ratios whose ground-tracks extend into the geomagnetic pole regions of the Earth will be more affected by perturbations to atmospheric density as a result of solar activity and more likely to benefit from applying a Kalman filter to process their observations than satellites that are not as highly affected by drag such as Meteor 1.

An adaptive state noise expression capable of expanding the state noise during periods of severe atmospheric disturbance while contracting the state noise during nominal conditions, proved to reduce the number of UCT's more effectively than a non-adaptive state noise for satellites susceptible to large crossing errors such as Cosmos 1601. The presence of ODP in the state noise formulation was the essential indicator of noise-level.

During periods of increasing solar or geomagnetic activity, ODP would grow as well as state noise, whereas immediately after a stormy period, ODP would decrease, bringing the state noise down as well.

To lower the possibility of a filter diverging or becoming reactive as a result of a bad estimate entering the adaptive state noise expression, a weighted running-mean of ODP should be used. This would help prevent an over estimated value of ODP from opening up, *i.e.*, increasing the state noise during otherwise quiet atmospheric conditions, which could lead to an over reactive filter, or in the case of a severely underestimated value of ODP, filter divergence. The non-adaptive state noise expression on the other hand, is not dependent on ODP and as a result, the filter is less vulnerable to divergence and reactivity problems.

Regardless of which state noise expression is employed, the Kalman filter is still susceptible to bad data entering the process, which leads to poor estimates of ODP. This can be circumvented by checking each measurement and down-weighting, or increasing the measurement noise, for those observations that fall outside an expected range. This leads to a slower response from the filter to real changes in satellite ODP, but prevents the filter from making abrupt changes to ODP based on poor data.

Implementing a Kalman filter system to help maintain the satellite catalog will most likely require individual filters for each satellite. Each filter would have to be tuned in order for the filter to respond correctly during real atmospheric events while ignoring noisy measurements. The process of tuning requires adjusting the state noise so that the filter can make corrections to the state that will minimize residual crossing errors without

causing the filter to diverge or become reactive. The degree to which a satellite is affected by drag would determine whether to use the adaptive or non-adaptive state noise expression. In some cases it may be possible to use the same state noise expression for satellites in similar orbits and with similar physical properties.

Future Work

The two research approaches investigated thus far suggest future work in the following areas:

Real-Time Systems Operation

Differential correction of elements needs to be performed in a real-time environment. This would allow testing the approaches of using atmospheric models and/or Kalman filters to improve estimates of ODP during periods of high solar activity, in preparation for incorporating these techniques into real-time operations.

Multi-state Kalman Filtering

The robustness of the Kalman filter technique needs to be improved. Using a multi-state Kalman filter, *i.e.*, a filter having a state vector of multiple components such as ℓ , n , and ODP, to process fence-crossings as opposed to a single state, may provide a more accurate estimate of ODP. A one-state filter has only one degree of freedom, requiring the ODP output of the filter to solely eliminate residual crossing errors. This can lead to over

correction since there are other variables that could be responsible for the inaccuracy in fence crossing time, such as errors in ℓ and n .

Hybrid Approach

A hybrid approach to reducing UCT's involving both the orbital decay parameter model and the Kalman filter process may prove beneficial. This technique would take advantage of the predictive capability of atmospheric models to estimate the initial state or *a priori* of a Kalman filter, rather than just guessing the initial value, which is common practice when initializing a Kalman filter.

Appendix A: Atmospheric Modeling

To model the upper atmosphere, a number of assumptions are made. The atmosphere is generally assumed to be comprised of the following constituents up to 90 km: molecular Nitrogen (N_2), molecular Oxygen (O_2), Argon (Ar), and Helium (He), homogeneously mixed with a fixed volume composition leading to a constant mean molecular weight \bar{M} .[†] Above this altitude, dissociation of molecular oxygen due to extreme ultraviolet (EUV) absorption lowers the mean molecular weight.⁵³ The atmosphere is assumed to be in hydrostatic equilibrium yielding the relationship:

$$dP = -g\rho dz \quad (27)$$

where dP is the differential of pressure, ρ is the density, g is the height-dependent acceleration of gravity, and dz is the differential of geodetic height. In addition, the air is taken as an ideal gas with an equation of state

$$P = \rho R \frac{T}{\bar{M}} \quad (28)$$

where R is the universal gas constant and T is the temperature. Upon substitution of (28) into (27), the barometric equation results⁵⁴

$$d \ln \rho = d \ln \left(\frac{\bar{M}}{T} \right) - \frac{\bar{M}g}{RT} dz \quad (29)$$

After integrating and applying boundary conditions at 90 km, the density at altitude z , up to the homopause near 100 km, is given by (30).

$$\rho(z) = \rho_0 \frac{T_0}{M_0} \frac{\bar{M}(z)}{T(z)} \exp \left(-\frac{1}{R} \int_{90}^z \frac{\bar{M}g}{T} dz \right) \quad (30)$$

Above this altitude, the departure from mixing and onset of molecular diffusion require the atmosphere to be modeled by the diffusion equation⁵⁵

$$\frac{dn_i}{n_i} = -\frac{M_i g}{RT} dz - (1 + \alpha_i) \frac{dT}{T} \quad (31)$$

where n_i represents the number density, or the number of molecules of the i th species per unit volume, M_i the molecular weight of the i th species, and α_i the thermal diffusion coefficient of the i th species. The solution to (31) is given by⁵⁶

$$n_i(z) = n_i(100) \left(\frac{T(100)}{T(z)} \right)^{(1+\alpha_i)} \exp \left(-\frac{M_i}{R} \int_{100}^z \frac{g}{T} dz \right) \quad (32)$$

Total density is then found using

$$\rho = \frac{1}{N_A} \sum n_i M_i \quad (33)$$

where N_A is Avogadro's number. These equations form the general underlying basis for determining atmospheric density, given a temperature profile $T(z)$ and altitude z .

There are a variety of temperature profiles in use in atmospheric models. Those typical of L.G. Jacchia, specifically J71,⁵⁷ begins at a boundary condition of $z_0 = 90$ km, where the temperature starts at a fixed value of $T_0 = 183^\circ$ K, and has a gradient of

$$G_0 = \left(\frac{dT}{dz} \right)_{z=z_0} = 0 \quad (34)$$

An inflection point occurs at a fixed height of $z_x = 125$ km, above which the profile becomes asymptotic to a temperature T_∞ , referred to as the exospheric temperature. The temperature at z_x is given by

* Minor constituents are ignored; Hydrogen is introduced between 150 – 500 km, depending on the model.

$$T_x = a + bT_\infty + ce^{kT_x} \quad (35)$$

where $a = 371.6678$, $b = 0.0518806$, $c = -294.3505$, and $k = -0.00216222$.

For temperatures in the region of 90 to 125 km, the temperature profile is given by the fourth-order polynomial

$$T = T_x + \sum_{n=1}^4 c_n (z - z_x)^n \quad (36)$$

subject to the following constraints

$$\text{when } z = z_0 \begin{cases} T = T_0 \\ G_0 = \left(\frac{dT}{dz} \right)_{z=z_0} = 0 \end{cases}$$

$$\text{when } z = z_x \begin{cases} G_x = \left(\frac{dT}{dz} \right)_{z=z_x} = 1.9 \frac{T_x - T_0}{z_x - z_0} \\ \left(\frac{d^2T}{dz^2} \right)_{z=z_x} = 0 \end{cases}$$

The coefficients c_n can then be solved for in terms of T_x , and are given by

$$c_1 = 1.9 \frac{(T_x - T_0)}{(z_x - z_0)}$$

$$c_2 = 0$$

$$c_3 = -1.7 \frac{(T_x - T_0)}{(z_x - z_0)^3} \quad (37)$$

$$c_4 = -0.8 \frac{(T_x - T_0)}{(z_x - z_0)^4}$$

For altitudes above 125 km, temperature profiles are given by

$$T = T_x + \varepsilon \tan^{-1} \left\{ \frac{G_x}{\varepsilon} (z - z_x) \left[1 + \vartheta (z - z_x)^\xi \right] \right\}, \quad (38)$$

where $\varepsilon = \frac{2}{\pi} (T_\infty - T_x)$, $\vartheta = 4.5 \times 10^{-6}$ and $\xi = 2.5$.

Appendix B: Model of Orbital Motion

The model of orbital motion used to maintain the satellite catalog applies a technique similar to the method of variation of parameters, but does not require numerical integration. The model, PPT2³⁴, employs an algorithm developed using Hamiltonian mechanics to propagate orbital elements in time by adding factors correcting for perturbations due to the non-sphericity of the Earth. PPT2 is based upon satellite orbital theory *without* drag as developed by Dirk Brouwer⁵⁸, coupled with improvements made by R. Lyddane⁵⁹ that remove singularities at $e = 0$ and $i = 0$. In addition, drag is modeled using time derivatives of mean anomaly. What follows is a brief description of the Brouwer/Lyddane corrections to the elements, preceded by the PPT2 drag model and a discussion of the satellite position prediction routine.

Brouwer/Lyddane Model

The Brouwer/Lyddane model⁶⁰ of orbital motion accounts for the non-sphericity of the Earth by using a spherical harmonic representation of the geopotential

$$U = \frac{\mu}{r} + \frac{\mu}{r} \sum_{n=2}^{\infty} \frac{R_{\oplus}^n}{r^n} \sum_{m=0}^n P_n^m(\sin \beta) [C_{n,m} \cos(m\lambda) + S_{n,m} \sin(m\lambda)] \quad (39)$$

where β is the satellite latitude, λ is the longitude, $C_{n,m}$ and $S_{n,m}$ are coefficients which depend on the mass distribution, P_n^m are the associated Legendre polynomials, μ is the gravitational constant, R_{\oplus} is the equatorial radius of the Earth, and r is the magnitude of the position vector of the satellite. Equation (39) is often approximated by ignoring the longitudinal terms resulting in only a zonal harmonic approximation to the geopotential:

$$U = \frac{\mu}{r} - \frac{\mu}{r} \sum_{n=2}^{\infty} \frac{R_{\oplus}^n}{r^n} J_n P_n(\sin \beta) \quad (40)$$

where $J_n = -C_{n,0}$. Zonal harmonics are dependent on the mass distribution that is symmetric about the north-south axis of the Earth, *i.e.*, they are not dependent on longitude. In addition, even-numbered harmonics are symmetric about the equatorial plane, whereas odd-numbered harmonics are anti-symmetric.⁶¹ Due to the presence of inverse powers of r in the geopotential, equation (40) may be truncated. The Brouwer model takes advantage of this and uses an expansion of (40) in the first four zonals

$$\begin{aligned} U = & \frac{\mu}{r} + J_2 \frac{\mu R_{\oplus}^2}{2r^3} (1 - 3\sin^2 \beta) + J_3 \frac{\mu R_{\oplus}^3}{2r^4} (3\sin \beta - 5\sin^3 \beta) \\ & - \frac{1}{8} J_4 \frac{\mu R_{\oplus}^4}{r^5} (3 - 30\sin^2 \beta + 35\sin^4 \beta) \\ & - \frac{1}{8} J_5 \frac{\mu R_{\oplus}^5}{r^6} (15\sin \beta - 70\sin^3 \beta + 63\sin^5 \beta) \end{aligned} \quad (41)$$

where

$$\begin{aligned} J_2 &= 0.4841605 \times 10^{-3} \sqrt{5} & J_3 &= -0.95958 \times 10^{-6} \sqrt{7} \\ J_4 &= -0.55199 \times 10^{-6} \sqrt{9} & J_5 &= -0.65875 \times 10^{-7} \sqrt{11} \end{aligned}$$

The variation in the elements is separated into secular and periodic corrections. The secular corrections are functions of the even zonals, *i.e.*, $J_2, J_4, \text{etc.}$, eccentricity, semi-major axis, and inclination. Periodic corrections are broken down further into long and short period corrections. Short period corrections are functions of J_2 and the elements, while long period corrections are functions of all the zonal terms and elements. The secular and periodic corrections are listed, followed by the Brouwer/Lyddane algorithm for propagating orbital elements.

Secular Corrections

$$\text{Define } \eta = \sqrt{1 - e''^2} \quad \theta = \cos i'',$$

and introduce the following dimensionless variables

$$\gamma_2 = \frac{1}{2a''^2} J_2 R_\oplus^2 \quad \gamma_3 = -\frac{1}{a''^3} J_3 R_\oplus^3 \quad \gamma_4 = -\frac{3}{8a''^4} J_4 R_\oplus^4 \quad \gamma_5 = -\frac{1}{a''^5} J_5 R_\oplus^5$$

$$\gamma'_2 = \frac{\gamma_2}{\eta^4} \quad \gamma'_3 = \frac{\gamma_3}{\eta^6} \quad \gamma'_4 = \frac{\gamma_4}{\eta^8} \quad \gamma'_5 = \frac{\gamma_5}{\eta^{10}}$$

The secular corrections are represented by

$$\begin{aligned} \delta_s \ell &= \frac{3}{2} \gamma'_2 \eta (-1 + 3\theta^2) \\ &+ \frac{3}{32} \gamma'_2 \eta [-15 + 16\eta + 25\eta^2 + (30 - 96\eta - 90\eta^2)\theta^2 + (105 + 144\eta + 25\eta^2)\theta^4] \\ &+ \frac{15}{16} \gamma'_4 \eta e''^2 (3 - 30\theta^2 + 35\theta^4) \end{aligned}$$

$$\begin{aligned} \delta_s \omega &= \frac{3}{2} \gamma'_2 (-1 + 5\theta^2) \\ &+ \frac{3}{32} \gamma'_2 [-35 + 24\eta + 25\eta^2 + (90 - 192\eta - 126\eta^2)\theta^2 + (385 + 360\eta + 45\eta^2)\theta^4] \\ &+ \frac{5}{16} \gamma'_4 [21 - 9\eta^2 + (-270 + 126\eta^2)\theta^2 + (385 - 189\eta^2)\theta^4] \end{aligned}$$

$$\begin{aligned} \delta_s \Omega &= -3\gamma'_2 \theta + \frac{3}{8} \gamma'_2 [(-5 + 12\eta + 9\eta^2)\theta + (-35 - 36\eta - 5\eta^2)\theta^3] \\ &+ \frac{5}{4} \gamma'_4 (5 - 3\eta^2)(3 - 7\theta^2)\theta \end{aligned}$$

Long Period Corrections

$$\begin{aligned}\delta_1 e &= e'' \eta^2 \left(\frac{1}{8} \gamma'_2 \left[1 - 11\theta^2 - \frac{40\theta^4}{1-5\theta^2} \right] - \frac{5\gamma'_4}{12\gamma'_2} \left[1 - 3\theta^2 - \frac{8\theta^4}{1-5\theta^2} \right] \right) \cos 2\omega'' \\ &+ \frac{\eta^2 \sin i''}{4\gamma'_2} \left(\gamma'_3 + \frac{5\gamma'_5}{16} (4 + 3e''^2) \left[1 - 9\theta^2 - \frac{24\theta^4}{1-5\theta^2} \right] \right) \sin \omega'' \\ &- \frac{35\gamma'_5}{384\gamma'_2} e''^2 \eta^2 \sin i'' \left[1 - 5\theta^2 - \frac{16\theta^4}{1-5\theta^2} \right] \sin 3\omega''\end{aligned}$$

$$\delta_1 i = -\frac{e'' \delta_1 e}{\eta^2 \tan i''}$$

$$\begin{aligned}\delta_1 \ell &= \eta^3 \left(\frac{1}{8} \gamma'_2 \left[1 - 11\theta^2 - \frac{40\theta^4}{1-5\theta^2} \right] - \frac{5\gamma'_4}{12\gamma'_2} \left[1 - 3\theta^2 - \frac{8\theta^4}{1-5\theta^2} \right] \right) \sin 2\omega'' \\ &- \frac{\eta^3 \sin i''}{4\gamma'_2 e''} \left(\gamma'_3 + \frac{5\gamma'_5}{16} (4 + 9e''^2) \left[1 - 9\theta^2 - \frac{24\theta^4}{1-5\theta^2} \right] \right) \cos \omega'' \\ &+ \frac{35\gamma'_5}{384\gamma'_2} e'' \eta^3 \sin i'' \left[1 - 5\theta^2 - \frac{16\theta^4}{1-5\theta^2} \right] \cos 3\omega''\end{aligned}$$

$$\delta_1 \omega = \left\{ \begin{aligned} & -\frac{1}{16} \gamma'_2 \left[(2 + e^{\prime\prime 2}) - 11(2 + 3e^{\prime\prime 2}) \theta^2 - \frac{40(2 + 5e^{\prime\prime 2}) \theta^4}{1 - 5\theta^2} - \frac{400e^{\prime\prime 2} \theta^6}{(1 - 5\theta^2)^2} \right] \\ & + \frac{5\gamma'_4}{24\gamma'_2} \left[(2 + e^{\prime\prime 2}) - 3(2 + 3e^{\prime\prime 2}) \theta^2 - \frac{8(2 + 5e^{\prime\prime 2}) \theta^4}{1 - 5\theta^2} - \frac{80e^{\prime\prime 2} \theta^6}{(1 - 5\theta^2)^2} \right] \end{aligned} \right\} \sin 2\omega$$

$$\begin{aligned} & + \frac{1}{4\gamma'_2} \left\{ \gamma'_3 \left(\frac{\sin i^{\prime\prime}}{e^{\prime\prime}} - \frac{e^{\prime\prime} \theta^2}{\sin i^{\prime\prime}} \right) \right. \\ & + \frac{5\gamma'_5}{16} \left[\left(\frac{\eta^2 \sin i^{\prime\prime}}{e^{\prime\prime}} - \frac{e^{\prime\prime} \theta^2}{\sin i^{\prime\prime}} \right) (4 + 3e^{\prime\prime 2}) + e^{\prime\prime} \sin i^{\prime\prime} (26 + 9e^{\prime\prime 2}) \right] \left[1 - 9\theta^2 - \frac{24\theta^4}{1 - 5\theta^2} \right] \\ & \left. - \frac{15\gamma'_5}{8} e^{\prime\prime} \theta^2 \sin i^{\prime\prime} (4 + 3e^{\prime\prime 2}) \left[3 + \frac{16\theta^2}{1 - 5\theta^2} + \frac{40\theta^4}{(1 - 5\theta^2)^2} \right] \right\} \cos \omega \end{aligned}$$

$$+ \frac{35\gamma'_5}{576\gamma'_2} \left\{ \begin{aligned} & -\frac{1}{2} \left(e^{\prime\prime} \sin i^{\prime\prime} (3 + 2e^{\prime\prime 2}) - \frac{e^{\prime\prime 3} \theta^2}{\sin i^{\prime\prime}} \right) \left[1 - 5\theta^2 - \frac{16\theta^4}{1 - 5\theta^2} \right] \\ & + e^{\prime\prime 3} \theta^2 \sin i^{\prime\prime} \left[5 + \frac{32\theta^2}{1 - 5\theta^2} + \frac{80\theta^4}{(1 - 5\theta^2)^2} \right] \end{aligned} \right\} \cos 3\omega^{\prime\prime}$$

$$\begin{aligned} \delta_1 \Omega = e^{\prime\prime 2} \theta & \left(-\frac{\gamma'_2}{8} \left[11 + \frac{80\theta^2}{1 - 5\theta^2} + \frac{200\theta^4}{(1 - 5\theta^2)^2} \right] + \frac{5\gamma'_4}{12\gamma'_2} \left[3 + \frac{16\theta^2}{1 - 5\theta^2} + \frac{40\theta^4}{(1 - 5\theta^2)^2} \right] \right) \sin 2\omega^{\prime\prime} \\ & + \frac{e^{\prime\prime} \theta}{4\gamma'_2} \left\{ \frac{\gamma'_3}{\sin i^{\prime\prime}} + \frac{5\gamma'_5}{16 \sin i^{\prime\prime}} (4 + 3e^{\prime\prime 2}) \left[1 - 9\theta^2 - \frac{24\theta^4}{1 - 5\theta^2} \right] \right. \\ & \left. + \frac{15\gamma'_5}{8} \sin i^{\prime\prime} (4 + 3e^{\prime\prime 2}) \left[3 + \frac{16\theta^2}{1 - 5\theta^2} + \frac{40\theta^4}{(1 - 5\theta^2)^2} \right] \right\} \cos \omega^{\prime\prime} \\ & - \frac{35\gamma'_5}{576\gamma'_2} e^{\prime\prime 3} \theta \left\{ \frac{1}{2 \sin i^{\prime\prime}} \left[1 - 5\theta^2 - \frac{16\theta^4}{1 - 5\theta^2} \right] \right. \\ & \left. + \sin i^{\prime\prime} \left[5 + \frac{32\theta^2}{1 - 5\theta^2} + \frac{80\theta^4}{(1 - 5\theta^2)^2} \right] \right\} \cos 3\omega^{\prime\prime} \end{aligned}$$

Short Period Corrections

$$\delta_2 a = a'' \gamma_2 \left[(-1 + 3\theta^2) \left(\frac{a''^3}{r'^3} - \frac{1}{\eta^3} \right) + 3(1 - \theta^2) \frac{a''^3}{r'^3} \cos(2\omega' + 2f') \right]$$

$$\delta_2 e = \frac{\eta^3 \gamma_2}{2e''} \left[(-1 + 3\theta^2) \left(\frac{a''^3}{r'^3} - \frac{1}{\eta^3} \right) + 3(1 - \theta^2) \left(\frac{a''^3}{r'^3} - \frac{1}{\eta^4} \right) \cos(2\omega' + 2f') \right]$$

$$- \frac{\eta^2 \gamma_2'}{2e''} (1 - \theta^2) [3e'' \cos(2\omega' + 2f') + e'' \cos(2\omega' + 3f')]$$

$$\delta_2 i = \frac{\gamma_2'}{2} \theta \sin i'' [3 \cos(2\omega' + 2f') + 3e'' \cos(2\omega' + 2f') + e'' \cos(2\omega' + 3f')]$$

$$\delta_2 \ell = -\frac{\eta^3 \gamma_2'}{4e''} \left\{ \begin{array}{l} 2(-1 + 3\theta^2)(W22 + 1) \sin f' \\ + 3(1 - \theta^2) \left[(1 - W22) \sin(2\omega' + f') + \left(W22 + \frac{1}{3} \right) \sin(2\omega' + 3f') \right] \end{array} \right\}$$

$$\text{where } W22 = \frac{a''^2}{r'^2} \eta^2 + \frac{a''}{r'}$$

$$\delta_2 \omega = -\frac{\delta_2 \ell}{\eta} + \frac{\gamma_2'}{4} [6(-1 + 5\theta^2)(f' - \ell' + e'' \sin f') + (3 - 5\theta^2)W21]$$

$$\text{where } W21 = 3 \sin(2\omega' + 2f') + 3e'' \sin(2\omega' + 2f') + e'' \sin(2\omega' + 3f')$$

$$\delta_2 \Omega = -\frac{\gamma_2'}{2} \theta [6(f' - \ell' + e'' \sin f') - W21]$$

Propagation Algorithm

- Begin with the initial values of the mean elements a'' , e'' , i'' , ℓ_0'' , ω_0'' , and Ω_0'' .

Note: Double primes denote mean elements, which also may be obtained through suitable averaging of the osculating or instantaneous Kepler elements.

- Calculate mean motion: $n_0 = \sqrt{\frac{\mu}{a''^3}}$

- Propagate mean anomaly, argument of perigee, and ascending node:

$$\ell'' = \ell_0'' + n_0 t (1 + \delta_s \ell) \quad (42)$$

$$\omega'' = \omega_0'' + n_0 t \delta_s \omega \quad (43)$$

$$\Omega'' = \Omega_0'' + n_0 t \delta_s \Omega \quad (44)$$

where $\delta_s x$ represents the secular contribution to the element x .

- Compute $\delta_1 e$, $e'' \delta_1 \ell$, $\delta_1 i$, and $(\sin i'') \delta_1 \Omega$

where $\delta_1 x$ is the long period correction to element x .

- Calculate $\delta_1 z = \delta_1 \ell + \delta_1 \omega + \delta_1 \Omega$
- Solve the system of equations

$$E'' - e'' \sin E'' = \ell'' \quad (45)$$

$$\tan \frac{1}{2} f'' = \sqrt{\frac{1+e''}{1-e''}} \tan \frac{1}{2} E'' \quad (46)$$

$$r'' = \frac{a''(1-e''^2)}{(1+e'' \cos f'')} \quad (47)$$

for true anomaly and position.

- Calculate $\delta_2 z = \delta_2 \ell + \delta_2 \omega + \delta_2 \Omega$

where δ_2x represents the short period corrections to element x.

- Calculate $z = \ell + \omega + \Omega = \ell'' + \omega'' + \Omega'' + \delta_1z + \delta_2z$
- Compute $e''\delta\ell = e''\delta_1\ell + e''\delta_2\ell$ and $\delta i = \delta_1i + \delta_2i$

- Calculate

$$\left(\sin\frac{1}{2}i''\right)\delta\Omega = \frac{(\sin i'')(\delta_1\Omega + \delta_2\Omega)}{2\cos\frac{1}{2}i''} \quad (48)$$

- $a = a'' + \delta_2a$

- Solve the system below for e, ℓ , i, and Ω .

$$e\cos\ell = (e'' + \delta e)\cos\ell'' - e''\delta\ell\sin\ell''$$

$$e\sin\ell = (e'' + \delta e)\sin\ell'' + e''\delta\ell\cos\ell''$$

$$\left(\sin\frac{1}{2}i\right)\cos\Omega = \left[\sin\frac{1}{2}i'' + \left(\cos\frac{1}{2}i''\right)\frac{1}{2}\delta i\right]\cos\Omega'' - \left(\sin\frac{1}{2}i''\right)\delta\Omega\sin\Omega'' \quad (49)$$

$$\left(\sin\frac{1}{2}i\right)\sin\Omega = \left[\sin\frac{1}{2}i'' + \left(\cos\frac{1}{2}i''\right)\frac{1}{2}\delta i\right]\sin\Omega'' + \left(\sin\frac{1}{2}i''\right)\delta\Omega\cos\Omega''$$

- Determine the satellite position vector \vec{r} using equations (45) - (47) with the newly found osculating elements.

Atmospheric Drag

The satellite orbit propagator, PPT2³⁴, does not contain an atmospheric model to handle drag effects on satellite orbital motion. The effects of drag, as well as other non-central forces such as solar radiation pressure, satellite thrusting, etc., that are not contained in PPT2, are represented by the time rate of change in mean motion as shown in equation (50),

$$\ell = \ell_0 + mt + \frac{1}{2} \dot{n} t^2 + \frac{1}{6} \ddot{n} t^3 + \dots \quad (50)$$

$$\text{where } m = n_0 t(1 + \delta_s \ell),$$

ℓ is mean anomaly, ℓ_0 is mean anomaly at epoch, *i.e.*, $t = 0$, n_0 is the mean motion at epoch, \dot{n} is the time rate of change of mean motion, \ddot{n} is the time rate of change of \dot{n} , and t is time. Normally, the \ddot{n} term is ignored, except for satellites with high decay rates. In addition, mean motion is updated using

$$n = n_0 + \dot{n} t \quad (51)$$

where n_0 is the mean motion at epoch.

For a LEO satellite, \dot{n} , or the orbital decay parameter (ODP), is primarily the result of atmospheric drag acting in a direction opposite to the satellite velocity vector. Changes in the mean motion of a satellite will effect the remaining orbital elements describing the orbit. Primarily, the effects are seen in the semi-major axis and eccentricity of the orbit as described by equation (52) and (53) below.⁶²

$$\dot{a} = -\frac{2}{3} \frac{a}{n} \dot{n} \quad (52)$$

$$\dot{e} = -\frac{2e}{3n} (1 - e^2) \dot{n} \quad (53)$$

Drag lowers the semi-major axis and eccentricity of a satellite orbit, thus tending to circularize the orbit. PPT2 uses (52) and (53) when propagating the mean elements to a specified time, as well as when making fence-crossing predictions.

Fence-Crossing Time Prediction

The capability is included in PPT2 to predict satellite fence crossing time for the purposes of preparing a chronological schedule of upcoming observations. When a satellite observation occurs, the actual crossing time is compared to the predicted, and if the observed minus the calculated (O-C), or residual error, is within two seconds, the satellite is considered to be identified. A diagram depicting the geometry of a typical fence station observation is presented next, followed by the method used in PPT2 to perform fence-crossing predictions.

Station Observation Geometry

Figure 29 illustrates the geometry of a typical radar fence observation,

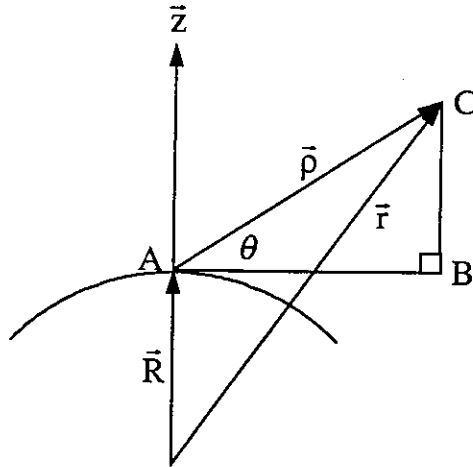


Figure 29: Fence-crossing geometry

where point A represents the ground station, \vec{R} is the station vector, \vec{r} is the satellite position vector, \hat{z} is the local vertical, $\vec{\rho}$ is the slant range, \overline{AB} is the ground range, \overline{BC} is the vertical range, and θ is the angle of elevation. Here the plane of the paper coincides with the fence plane.

PPT2 Prediction Algorithm

The capability to predict the geometry described in Figure 29 as well as fence crossing time is provided in PPT2. The condition that must be met signifying a satellite is crossing, *i.e.*, in the radar fence plane is illustrated in Figure 30,

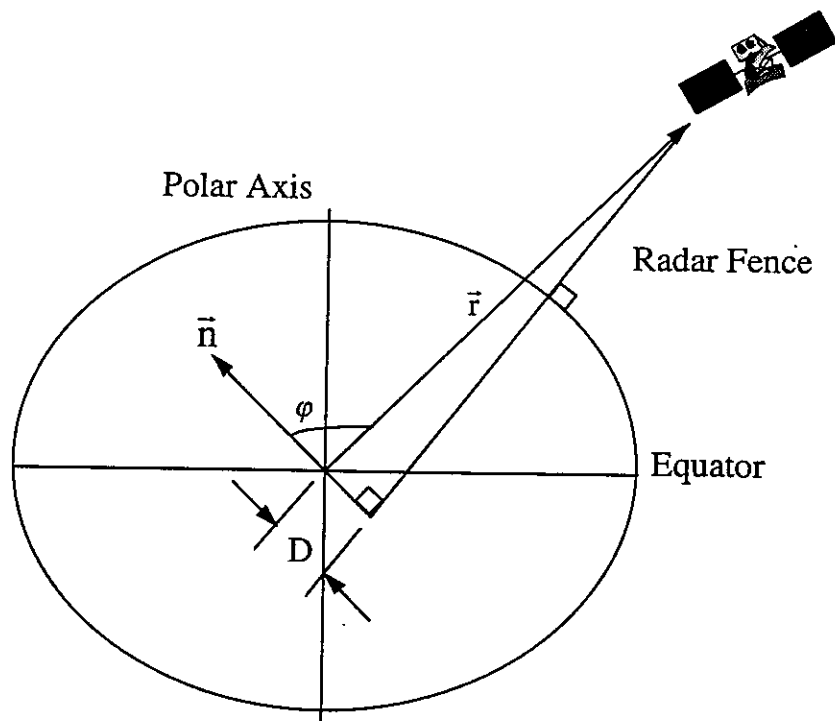


Figure 30: Satellite crossing radar fence-plane

where a satellite with position vector \vec{r} is crossing the radar fence depicted by the line perpendicular to the local horizontal and with unit normal vector \hat{n} , and D is the fence-plane displacement from the center of the Earth. The crossing constraint can be expressed mathematically as

$$\hat{n} \cdot \vec{r} + D \leq \delta \quad (54)$$

meaning that a satellite is considered to be crossing the radar fence when the fence normal component of the satellite position vector is equal to the fence displacement from the center of the Earth within an error tolerance δ .

The method used to make fence-crossing predictions begins as follows.

- Starting with the time of the elements or epoch, $t = 0$, update eccentricity using

$$e'' = e_0'' + \dot{e} t \quad (55)$$

- Compute the change in mean anomaly

$$\Delta \ell = E - e'' \sin E - \ell_0'' \quad (56)$$

$$\text{where } E = \frac{\sqrt{1-e''^2} \sin f}{1+e'' \cos f}$$

- Solve the cubic equation $\ell'' = \ell_0'' + n_0 t + \frac{\dot{n}}{2} t^2 + \frac{\ddot{n}}{6} t^3$ for time using iteration, starting with $\Delta t = \Delta \ell / m$

$$J = \Delta \ell - m \Delta t - \frac{\dot{n}}{2} \Delta t^2 + \frac{\ddot{n}}{6} \Delta t^3 \quad (57)$$

$$\Delta t = \Delta t + \frac{J}{m}$$

Iterate while $|J| \geq 10^{-4}$ up to 20 times.
then $t = t + \Delta t$

- Update a'' , ω'' , and Ω'' using

$$a'' = a'' + \dot{a} \Delta t$$

$$\omega'' = \omega_0'' + \frac{d\omega''}{d\ell} \Delta \ell'' \quad (58)$$

$$\Omega'' = \Omega_0'' + \frac{d\Omega''}{d\ell} \Delta \ell''$$

- Apply periodic corrections to a , e , i , ω , Ω , and ℓ .
- Solve Kepler's equation (45), and update position using (47).

- Calculate
$$\frac{d\omega}{dt} = \frac{df}{dt} = \frac{m(1+e \cos f)^2}{(\sqrt{1-e^2})^3} \quad (59)$$

- Compute the correction to true anomaly:

$$\Delta f = \frac{df(\hat{n} \cdot \vec{r} + D)}{dt \hat{n} \cdot \vec{v}} \quad (60)$$

- If Δf is less than a tolerance value, the prediction is finished. Otherwise f is adjusted by Δf , and the procedure starts over again beginning with (55).⁶³

References

-
- ¹ Tschan, C.R., "'Weather' Forecasters Work on Higher Plane", *Aviation Week and Space Technology*, September 18, 1995, p 49.
- ² Cleeton, C.E., "The U.S. Navy Space Surveillance System", Proceedings of the IAS National Symposium on Tracking and Command of Aerospace Vehicles, San Francisco, CA, February 19-21, 1962, pp 140-144.
- ³ Bate, R.R., Mueller, D.D., White, J.E., *Fundamentals of Astrodynamics*, Dover Publications, New York, 1971, pp 122-125.
- ⁴ Keating, G.M., Prior, E.J., Chang, K., Nicholson III, J.Y., and von Zahn, U., "Comparison of Drag and Mass Spectrometer Measurements During Small Geomagnetic Disturbances", *Space Research XVII*, p 355, 1977.
- ⁵ King-Hele, D.G., *Satellite Orbits in an Atmosphere: Theory and Applications*, Blackie and Son Ltd, London, 1987, pp 44-46.
- ⁶ *Ibid.*, pp 47-53.
- ⁷ *Ibid.*, pp 54-71.
- ⁸ Wertz, J.R. (ed.), *Spacecraft Attitude Determination and Control*, D. Reidel Publishing Co., Boston, 1985, p 64.
- ⁹ Jacchia, L.G., "The Earth's Upper Atmosphere - II", *Sky and Telescope*, pp 230-231, April, 1975.
- ¹⁰ Brown, R.G. and Hwang, P.Y.C., *Introduction to Random Signals and Applied Kalman Filtering*, 2nd Ed., John Wiley & Sons, Inc., New York, 1992
- ¹¹ *Ibid.*, pp 230-232.
- ¹² *Ibid.*, pp 234-236
- ¹³ Lyons, D.T., "Aerobraking Magellan: Plan versus Reality", *AAS/AIAA Spaceflight Mechanics Meeting*, Cocoa Beach, FL, February 14-16, 1994.
- ¹⁴ King-Hele, D.G., *Satellite Orbits in an Atmosphere: Theory and Applications*, Blackie and Son Ltd, London, 1987, p 77.

-
- ¹⁵ Wertz, J.R. (ed.), *Spacecraft Attitude Determination and Control*, D. Reidel Publishing Co., Boston, 1985, pp 98-99.
- ¹⁶ COESA, "U.S. Standard Atmosphere, 1976", National Oceanic and Atmospheric Administration, U.S. Gov. Printing Office, 1976, pp 7-8.
- ¹⁷ Bate, R.R., Mueller, D.D., White, J.E., *Fundamentals of Astrodynamics*, Dover Publications, 1971, p 94.
- ¹⁸ Jacchia, L.G., "The Earth's Upper Atmosphere - 1", *Sky and Telescope*, March 1975, pp 155-159.
- ¹⁹ Jacchia, L.G., "Revised Static Models of the Thermosphere and Exosphere with Empirical Temperature Profiles", *Smithsonian Astrophysical Observatory Special Report No. 332*, 1971, p 21.
- ²⁰ Prolss, G.W., Roemer, M., Slowey, J.W., "Dissipation of Solar Wind Energy in the Earth's Upper Atmosphere: The Geomagnetic Activity Effect", *Advances in Space Research*, Vol. 8, No. 5-6, 1988, pp (5)215-(5)217.
- ²¹ Hickey, M.P., "The Marshall Engineering Thermospheric Model", *NASA CR-179359*, 1988.
- ²² Jacchia, L.G., "Revised Static Models of the Thermosphere and Exosphere with Empirical Temperature Profiles", *Smithsonian Astrophysical Observatory Special Report No. 332*, 1971.
- ²³ Jacchia, L.G., "Thermospheric Temperature, Density, and Composition, a New Model", *Smithsonian Astrophysical Observatory Special Report No. 375*, 1977
- ²⁴ Hedin, A.E., "MSIS-86 Thermospheric Model", *J. Geophys. Res.*, 92, 1987, pp 4649 - 4662.
- ²⁵ Jacchia, L.G., "New Static Models of the Thermosphere and Exosphere with empirical Temperature Profiles", *Smithsonian Astrophysical Observatory*, Special Report No. 313, 1970.
- ²⁶ Keating, G.M. and Prior, E.J., "The Winter Helium Bulge", *Space Research VIII*, North Holland Publishing Co., Amsterdam, 1968, pp 982-992.
- ²⁷ Bates, D.R., "Some Problems Concerning the Terrestrial Atmosphere Above About the 100-km Level", *Proceedings of the Royal Society of London*, A253, 1959, pp 451-462.

-
- ²⁸ NRC Committee on Space Debris, *Orbital Debris - A Technical Assessment*, National Academy Press, Washington, D.C., 1995, p 38.
- ²⁹ King-Hele, D.G., Walker, D.M.C., *The R.A.E. Table of Earth Satellites 1957-1989*, Fourth ed., Royal Aerospace Establishment, Farnborough Hants, England, 1990.
- ³⁰ Thomas, P.G., (ed), "Space Traffic Surveillance", *Space/Aeronautics*, November, 1967
- ³¹ Cleeton, C.E., "The U.S. Navy Space Surveillance System", Proceedings of the IAS National Symposium on Tracking and Command of Aerospace Vehicles, pp 140-144, February 19-21, 1962, San Francisco, CA.
- ³² *Ibid.*
- ³³ Hayden, C.C. and Knowles, S.H., "Naval Space Surveillance Center Uses of Time, Frequency, and Phase", Proceedings of the 23rd Annual Precise Time and Time Interval (PTTI) Applications and Planning Meeting, NASA Goddard Space Flight Center, Greenbelt, MD, 1992, pp 127-132.
- ³⁴ NAVSPACOM, "PPT2: The NAVASPASUR Model of Satellite Motion", 1992, p 20.
- ³⁵ Bate, R.R., Mueller, D.D., White, J.E., *Fundamentals of Astrodynamics*, Dover Publications, 1971, p 125.
- ³⁶ NAVSPACOM, "PPT2: The NAVASPASUR Model of Satellite Motion", 1992, pp 22-24.
- ³⁷ NRC Committee on Space Debris, *Orbital Debris - A Technical Assessment*, National Academy Press, Washington, D.C., 1995, p 36.
- ³⁸ Cook, G.E., "Drag Coefficients of Spherical Satellites", *Annales De Geophysique*, 1966, pp 53-64.
- ³⁹ Bate, R.R., Mueller, D.D., White, J.E., *Fundamentals of Astrodynamics*, Dover Publications, 1971, pp 387-388.
- ⁴⁰ Cliver, E.W., *et. al.*, "An Estimate of the Maximum Speed of the Solar Wind, 1938-1989", *Journal of Geophysical Research*, 95, 1990, p 17,104.
- ⁴¹ King-Hele, D.G., Walker, D.M.C., *et. al.*, "The R.A.E. Table of Earth Satellites 1957-1989", Fourth Ed., Royal Aerospace Establishment, Farnborough Hants, England, 1990.
- ⁴² King-Hele, D.G., *Satellite Orbits in an Atmosphere: Theory and Applications*, Blackie and Son Ltd, London, 1987, pp 5-6.

-
- ⁴³ Jacchia, L.G., "Revised Static Models of the Thermosphere and Exosphere with Empirical Temperature Profiles", Smithsonian Astrophysical Observatory, Special Report 332, 1971, pp 41-44.
- ⁴⁴ Prolss, G.W., Roemer, M., Slowey, J.W., "Dissipation of Solar Wind Energy in the Earth's Upper Atmosphere: The Geomagnetic Activity Effect", *Advances in Space Research*, Vol. 8, No. 5-6, 1988, pp (5)215-(5)217.
- ⁴⁵ Hardin, J.C., *Introduction to Time Series Analysis*, NASA Reference Publication 1145, 2nd Printing, 1990, p 116.
- ⁴⁶ Hicks, J.R., "An Adaptive Thermospheric Model to Improve the Prediction of Satellite Orbits", MS thesis, The George Washington University, March 1997.
- ⁴⁷ King-Hele, D.G., *Satellite Orbits in an Atmosphere: Theory and Applications*, Blackie and Son Ltd, London, 1987, pp 27-28.
- ⁴⁸ Vahlberg, J.C, "Atmospheric Effects Task, Final Kalman Filtering Results", Space Surveillance Workshop, MIT Lincoln Laboratory, April 9-11, 1991.
- ⁴⁹ Bozic, S.M., *Digital and Kalman Filtering: an Introduction to Discrete-Time Filtering and Optimum Linear Estimation*, 2nd ed., Halsted Press, New York, 1994, pp 125-126.
- ⁵⁰ Candy, J.V., *Signal Processing The Model-Based Approach*, McGraw-Hill, New York, 1986, pp 106-110.
- ⁵¹ Grewal, M.S., and Andrews, A.P., *Kalman Filtering Theory and Practice*, Prentice-Hall, Englewood Cliffs, 1993, p 278.
- ⁵² Candy, J.V., *Signal Processing The Model-Based Approach*, McGraw-Hill, New York, 1986, p 107.
- ⁵³ Jacchia, L.G., "The Earth's Upper Atmosphere - I", *Sky and Telescope*, pp 156-157, March, 1975.
- ⁵⁴ COESA, "U.S. Standard Atmosphere, 1976", *National Oceanic and Atmospheric Administration*, U.S. Gov. Printing Office, 1976, p 6.
- ⁵⁵ *Ibid.*, p 6.
- ⁵⁶ Jacchia, L.G., "New Static Models of the Thermosphere and Exosphere with empirical Temperature Profiles", *Smithsonian Astrophysical Observatory*, Special Report No. 313, pp 3-7, 1970.

⁵⁷ Jacchia, L.G., "Revised Static Models of the Thermosphere and Exosphere with Empirical Temperature Profiles", *Smithsonian Astrophysical Observatory*, Special Report No. 332, pp 11-12, 1971.

⁵⁸ Brouwer, D., "Solution of the Problem of Artificial Satellite Theory Without Drag", *Astronomical Journal*, 64, November 1959.

⁵⁹ Lyddane, R.H., "Small Eccentricities in the Brouwer Theory of the Artificial Satellite", *Astronomical Journal*, 68, October 1963.

⁶⁰ NAVSPACOM, "PPT2: The NAVSPASUR Model of Satellite Motion", 1992 pp 3-8.

⁶¹ Bate, R.R., Mueller, D.D., White, J.E., *Fundamentals of Astrodynamics*, Dover Publications, 1971, pp 422-423.

⁶² NAVSPACOM, "PPT2: The NAVSPASUR Model of Satellite Motion", 1992, pp 9-10.

⁶³ *Ibid.* pp 19-22.